Nondestructive Evaluation of the Condition of Subsurface Drainage in Pavements Using Ground Penetrating Radar (GPR)

Horizontal axis — Horizontal position (ft)
Vertical axis — Receiving time (ns)

Joseph V. Sinfield, Hao Bai

AUTHORS

Joseph V. Sinfield, ScD
Associate Professor of Civil Engineering
School of Civil Engineering
Purdue University
(765) 496-2742
jvs@purdue.edu
Corresponding Author

Hao Bai
Graduate Research Assistant
School of Civil Engineering
Purdue University

JOINT TRANSPORTATION RESEARCH PROGRAM

The Joint Transportation Research Program serves as a vehicle for INDOT collaboration with higher education institutions and industry in Indiana to facilitate innovation that results in continuous improvement in the planning, design, construction, operation, management and economic efficiency of the Indiana transportation infrastructure. https://engineering.purdue.edu/JTRP/index_html

Published reports of the Joint Transportation Research Program are available at: http://docs.lib.purdue.edu/jtrp/

1. Report No.	2. Government Accession No.	3. Recipient's Catalog No.
FHWA/IN/JTRP-2013/25		

4. Title and Subtitle	5. Report Date
Nondestructive Evaluation of the Condition of Subsurface Drainage in Pavements Using Ground Penetrating Radar (GPR)	November 2013
	6. Performing Organization Code

7. Author(s)	8. Performing Organization Report No.
Joseph V. Sinfield, Hao Bai	FHWA/IN/JTRP-2013/25

9. Performing Organization Name and Address	10. Work Unit No.
Joint Transportation Research Program Purdue University 550 Stadium Mall Drive West Lafayette, IN 47907-2051	
	11. Contract or Grant No. SPR-3419

12. Sponsoring Agency Name and Address	13. Type of Report and Period Covered
Indiana Department of Transportation State Office Building 100 North Senate Avenue Indianapolis, IN 46204	Final Report
	14. Sponsoring Agency Code

15. Supplementary Notes

Prepared in cooperation with the Indiana Department of Transportation and Federal Highway Administration.

16. Abstract

Subsurface drainage features are routinely incorporated in the design of pavement systems as they are believed to increase pavement service life provided that they are installed correctly and maintained. Maintenance, however, is challenging in that location and subsequent inspection of these systems can be time consuming and laborious. With this in mind, some departments of transportation have turned to ground penetrating radar (GPR) as one means to rapidly locate subsurface drainage features in pavements and thus alleviate some of the cost and complexity of maintaining these systems, but with mixed results.

In this context, this study pursued a two-pronged approach to improve GPR-based location of sub-pavement drainage systems, involving: (1) software-based signal processing and (2) modifications of hardware test configurations. From a signal processing perspective, two complementary signal processing approaches were developed in this work. Method 1 involved algorithms that are designed to reduce GPR signal background clutter and noise by taking advantage of the somewhat uniform nature of the strata underlying constructed pavements and to systematically remove anomalous signals. Method 2 focused on enhancing 2-D image quality to facilitate recognition of hyperbolic signal returns indicative of drain detection. From a hardware perspective, field experiments were also carried out in this work to validate the signal processing algorithms and assess the potential for alternative antenna configurations to enhance detection success. Five different antenna configurations were tested in total. When employed in field settings, the signal processing algorithms demonstrated an ability to routinely detect X-drains (shallow depth, PVC) with 2–3 false alarms per successful detection. Similarly, all known K-drains (moderate depth, metal/clay) in the studied field test regions were successfully identified, although each successful K-drain detection was accompanied by a significant number of potential false alarms. Beyond these signal conditioning related findings, additional recommendations for field deployed GPR survey line selection, antennae configuration, and frequency selection are also provided.

17. Key Words	18. Distribution Statement
ground penetrating radar, GPR, sub-pavement drainage, pipe detection, signal processing	No restrictions. This document is available to the public through the National Technical Information Service, Springfield, VA 22161.

19. Security Classif. (of this report)	20. Security Classif. (of this page)	21. No. of Pages	22. Price
Unclassified	Unclassified	62	

Form DOT F 1700.7 (8-69)

EXECUTIVE SUMMARY

NONDESTRUCTIVE EVALUATION OF THE CONDITION OF SUBSURFACE DRAINAGE IN PAVEMENTS USING GROUND PENETRATING RADAR (GPR)

Introduction

Subsurface drainage features are routinely incorporated in the design of pavement systems as they are believed to increase pavement service life provided that they are installed correctly and maintained. Maintenance, however, is challenging in that location and subsequent inspection of outlet pipes, drainage conduits, and edge drains can be time-consuming and laborious.

Consequently, locating and evaluating the condition of existing subsurface drainage systems has now become a key factor to enable proper maintenance and increase the service life of pavement. There are several different methods that can be used to detect objects in subsurface settings, such as metal detectors, electronic marker systems, acoustic emission sensing, resistivity measurements, micro-gravitational techniques, and seismic reflection/refraction methods. However, ground penetrating radar (GPR)—a nondestructive geophysical technique that makes use of radio waves to examine low loss dielectric materials—appears to offer the greatest potential to facilitate drainage feature detection in subsurface settings.

In this context, the objective of this study was to determine whether GPR technology can be used to rapidly locate subsurface drainage features in pavements and thus alleviate some of the cost and complexity of maintaining these systems.

Findings

The work carried out in this program involved a two-pronged approach to improve GPR-based sub-pavement drainage system evaluation while maximizing the value of the Indiana Department of Transportation's (INDOT's) pre-existing investment in GPR hardware and remaining within project budget limitations. Two major avenues were explored to achieve improvements in GPR detection success: (1) software-based signal processing and (2) modifications of hardware test configurations.

From a signal processing perspective, two complementary sets of approaches were developed in this work, referred to herein as Methods 1 and 2. Method 1 involves two signal processing algorithms that are designed to reduce GPR signal background clutter and noise by taking advantage of the somewhat uniform nature of the strata underlying constructed pavements and to systematically remove anomalous signals. The output of this method is a 1-D plot of potential target locations as a function of distance on the survey line along the roadway. This method proved to be very effective at identifying both X- (shallow depth, PVC) and K-drains (moderate depth, metal/clay) even when a hyperbolic signal return could not be observed in the 2-D data. Generally, all X-drains are routinely identified (with only occasional exceptions), with three to four false alarms per successful detection. Similarly, all known K-drains in the studied field test regions were successfully identified, although each successful K-drain detection was accompanied by a significant number of potential false alarms. While these false alarms all require field investigation, the effort associated with these investigations is likely substantially less than the effort required to manage the consequences of undetected, and thus unmaintained,

K-drains. The reliability of Method 1 was shown to improve when scans obtained with two antennae are compared and when routine drain spacing is employed as a filter. These additional screens help to reduce false alarms to roughly two to three per successful detection.

Method 2 focuses on enhancing 2-D image quality to facilitate recognition of hyperbolic signal returns indicative of drain detection. When this method reveals a hyperbola, there is a clear "detect" outcome and thus the approach can clarify interpretation of potential targets identified via Method 1. It is important to note, however, that lack of a hyperbolic return in the 2-D image is not conclusive in declaring a "false alarm" as the statistical algorithms of Method 1 routinely detected pipes when no hyperbolic return was visible. Thus, in practice, it is likely important to investigate all potential target zones identified by Method 1. Overall, Method 2 would likely be most valuable if incorporated in an automated data processing system to help rapidly identify clear "detects" and thus limit the focus of in-field investigative study to only truly uncertain target zones.

From a hardware perspective, field experiments were also carried out in this work to assess the potential for alternative antenna configurations to enhance the detection success. Five different antenna configurations were tested. These tests reveal several conclusions that can be generalized as follows:

1. Survey line selection has a significant influence on the quality of obtained GPR images. In all cases, images obtained on the gravel side slope of roads provided clearer, higher SNR (signal to noise ratio) images of buried drains relative to images obtained in the middle of the shoulder of the roadway or at the pavement shoulder—gravel slope interface, and more frequently displayed, the characteristic hyperbolic returns expected from a buried conduit. It is worth noting that while operating on the gravel slope has some challenges in terms of maintaining the stability of the antennae, a survey line well off the roadway adds to the safety of the overall scanning operation. With this in mind, there is likely value in developing a robust outrigger setup that can facilitate antenna coupling with the ground on the gravel slopes beside roadways.

2. Test configurations involving two antennae facilitate more reliable detection strategies than single antennae configurations. The potential to compare results from two antennae along a shared survey line helps to distinguish background clutter and anomalies from actual pipe detections and facilitates signal averaging that can be employed to reduce the net background interference in post-processing. The benefits of this logic likely increase to a limit as additional antennae are added to the test setup.

3. In tests conducted with a transmitter and dual receivers operating at different frequencies, higher input frequencies yielded higher SNRdB results than lower input frequencies. However, at any given input frequency results obtained with the lower frequency receiver of the studied pair tended to provide higher SNRdB returns, indicating some loss in energy of the returned signal combined with a beneficial reduction in sensitivity to noise.

4. Cross-polarized configurations generally provided good results but did not yield a benefit that justified the added complexity of operating the cross-polarized system. It is important to note that only configurations involving a cross-polarized receiver oriented perpendicular to the transmitter and direction of travel and vice versa were pursued in this work. Other orientations of the entire cross-polarized setup may warrant future investigation.

Implementation

Based on the tests and data analyses performed herein, the following recommendations are provided to guide future deployments of GPR for subsurface drainage detection under pavements:

1. Implement the background reduction and anomaly detection algorithms developed in this work (Method 1) in a user-friendly software application that can be employed to process GPR data.
2. Implement the shape enhancement algorithms developed in this work (Method 2) to facilitate evaluation of potential target zones via an automated shape recognition routine.
3. Enhance on-board computing power employed in the field vehicle used to pull the GPR antennae so that data can be processed in real time, thereby enabling target zone marking during the GPR scanning operation (vs. post–data processing).
4. Develop a robust GPR unit outrigger capable of negotiating the gravel slopes alongside roadways to maximize energy coupling into the subsurface and enhance detection sensitivity.
5. Deploy (at least) two antennae in any survey operation to improve background management and facilitate results comparison that can increase the probability of successful detection and false alarm rejection.
6. Utilize configurations involving one transmitter and dual-frequency high-low receiver pairs to optimize energy input into the subsurface and minimize received noise.

CONTENTS

LIST OF TABLES

LIST OF FIGURES

1. INTRODUCTION AND PROBLEM STATEMENT

Subsurface drainage features are routinely incorporated in the design of pavement systems as they are believed to increase pavement service life provided that they are installed correctly and maintained. Maintenance, however, is challenging in that location and subsequent inspection of outlet pipes, drainage conduits, and edge drains can be time consuming and laborious.

Consequently, locating and evaluating the condition of existing subsurface drainage systems has now become a key factor to enable proper maintenance and increase the service life of pavement. While there are several different methods that can be used to detect objects in subsurface settings, such as metal detectors, electronic marker systems, acoustic emission sensing, resistivity measurements, micro-gravitational techniques and seismic reflection/refraction methods (*1*), ground penetrating radar – a nondestructive geophysical technique that makes use of radio waves to examine low loss dielectric materials – appears to offer the greatest potential to facilitate drainage feature detection in subsurface settings and may also provide information on drainage feature condition.

Several researchers have demonstrated the potential to locate plastic and clay conduit in agricultural soils (e.g., (*2,3*)), and assess water presence in/around buried conduits (e.g., (*4*)) using ground penetrating radar (GPR). Other researchers have successfully utilized GPR in the analysis of materials such as wood, concrete, and asphalt (e.g., (*5–8*)). However, routine success in use of the method is highly dependent upon subsurface conditions, the presence or lack of water, the nature of the subsurface target being sought, and its depth. Further, effective use of GPR still requires expert data interpretation.

2. OBJECTIVES AND SCOPE

Given the above background, the objective of the research herein was to determine if ground penetrating radar technology can be used to rapidly locate and determine the condition of subsurface drainage features in pavements and thus alleviate some of the cost and complexity of maintaining these systems. To this end, this research study encompassed the following activities:

1. Performance of a literature review to develop a thorough understanding of the current state of knowledge on GPR applicability to sub-pavement drainage feature assessment.
2. Definition of the set of physical parameters that characterize sub-pavement drainage systems in field settings likely to be encountered throughout Indiana.
3. Identification and acquisition of compatible, commercially available equipment to modify/enhance the existing INDOT GPR unit so that techniques and equipment configurations with the potential to enhance drainage system detection success could be objectively assessed in the laboratory and/or field.

4. Application of GPR simulation tools to inexpensively and rapidly evaluate alternate GPR test configurations.
5. Design, fabrication, and application of a laboratory based experiment to enable proof testing of the enhanced/modified GPR system under controlled testing conditions.
6. Development and/or application of unique signal processing techniques to enhance drainage system detection sensitivity.
7. Performance of in-laboratory and in-field tests on simulated and/or actual road segments of known cross-section to assess GPR system performance under representative working conditions.
8. Analysis and synthesis of all findings to develop relevant conclusions.
9. Translation of the findings into an implementation plan for future routine application, where appropriate.

3. RESEARCH BACKGROUND

3.1 Introduction

Subsurface drainage systems are an important driver of the service life of pavements, as free water in pavement is a leading cause of road damage. To effectively evaluate subsurface drainage systems with ground penetrating radar, both experimentally and in the field, it is helpful to have a robust understanding of typical road cross-section design. A general review of pavement and subsurface drainage system design is therefore introduced here as well as an overview of the performance of drainage systems. In addition, a brief introduction to GPR and some of its key areas of application is also provided, highlighting connections to the current study.

3.2 Overview of Pavement Systems

3.2.1 Pavement and Drainage System Design

A pavement is usually constructed of asphalt or Portland cement concrete, or a layered composite of these materials. An asphalt pavement is referred to as a flexible pavement, in which a bituminous binder is combined with coarse and fine aggregates. A flexible pavement is typically constructed using Hot Mix Asphalt (HMA) or Warm Mix Asphalt (WMA). A Portland cement concrete pavement (PCCP) is referred to as a rigid pavement. In addition to these two major pavement categories, aggregate pavement is also common, which is constructed with compacted aggregate. The pavement structure is considered to be that part of the road that is placed on the finished subgrade and encompasses all paved surfaces including shoulders (*9*). Figure 3.1 shows typical cross-sections of flexible, rigid, and composite pavements, noting of course that the design of any specific roadway may vary.

Subsurface drains have been utilized in pavement systems since the 1950s. Transverse subsurface drains were among the first types of subsurface drains to be installed. This type of drain was typically a drain tile or
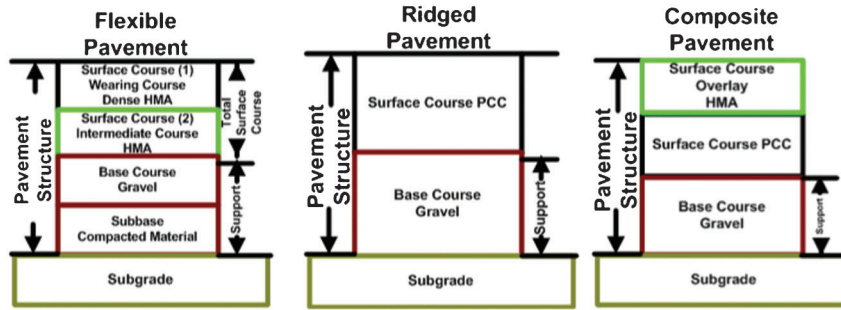
Figure 3.1 Typical cross sections of flexible pavement (HMA or WMA), rigid pavement (PCCP) and composite pavement (*10*).

perforated pipe constructed perpendicular to the pavement and spaced longitudinally throughout the project. Beginning in the 1960s, longitudinal pipes were constructed along the edges of the pavement with outlets to side ditches. Little or no maintenance was performed on the subsurface drain systems until a mid-1990s study showed that poor performance of the subsurface drain system was causing failures of pavement structures (*9*).

Today, subsurface drainage systems in pavement take the form of edge drainage pipes and outlet pipes, which are considered the most important drains in the system, here shown in Figure 3.2. In the transverse direction, several drainage alternatives can be considered based on design requirements. Hagen and Cochran (*11*) compared four typical drainage systems and concluded that use of permeable asphalt-stabilized base for the transverse drainable layers usually provided the most effective means to remove water from pavement and provided the driest pavement foundation and the least early pavement distress. Figure 3.3 gives a basic view of the different subsurface drainage elements in an example PCC Pavement cross-section (*11*).

3.2.2 Performance of Drainage in Pavement

The reliable design and maintenance of subsurface drains can effectively remove free water and extend the service life of pavement. On the other hand, lack of drainage, and/or a poor sub-base with high fines content can obstruct proper water removal and lead to subsequent pavement damage (*13*). It is therefore important to routinely assess drain condition and effectiveness.

Figure 3.2 Typical drainage systems of modern pavements (with longitudinal edge-drain and outlet pipe) (*12*).

Ahmed et al. (*14*) conducted a study on the performance of existing sub-pavement drainage systems in Indiana. Observations in the study revealed that outlet pipes were frequently exposed for some length or crushed. Outlet markers were not present in the majority of cases, making it difficult to locate the outlets. Vegetation growth around the pipes sometimes blocked the flow completely. Field results were collected for different types of pavements, and the drainage efficiency was reported for these pavements. Figure 3.4 shows a typical hidden outlet pipe. Table 3.1 provides AASHTO criteria to describe the performance of drainage systems.

Subsurface drainage systems are installed for all important highway pavement structural sections. Although considering and constructing a sub-pavement drainage system is important to enable pavement function, maintenance is the key factor related to the service life of pavement. Several pavement failures have occurred recently in Indiana which have been attributed to poor drainage conditions (e.g., challenges with clogged sub-pavement outlet drains on I64 in the Seymour District; road patch failure associated with poor drainage on I69 in Fort Wayne; ice formation and related pavement damage caused by poor drainage on I164 in the Vincennes District). INDOT has concluded that unmaintained drainage can sometimes lead to worse damage than undrained pavement. Therefore, maintenance of the drainage system is as important as providing the system (*16*). In order to fulfill this goal, locating and evaluating the subsurface drainage conduit is the first and the most important problem to be solved.

3.3 Introduction to Ground Penetrating Radar

3.3.1 Introduction

Radar is an acronym for Radio Detection and Ranging and is based on a simple principle: detecting objects and determining their distances (range) from the echoes they reflect (*17*). Radar operates based on the principle of transmitting electromagnetic waves (Tx) and receiving (Rx) reflected signals from any object in their path (*18*). Radars transmit either pulsed (most situations) or continuous signals. For pulsed radars the target range is simply determined by the time it takes the pulse of radiated energy to travel to the target and return (*19*).
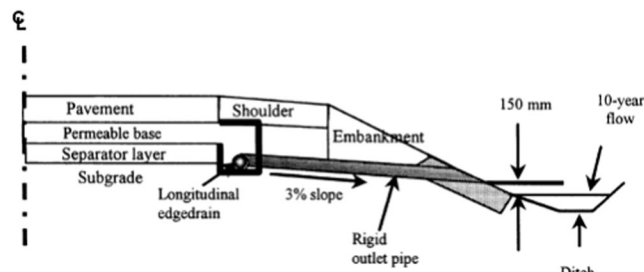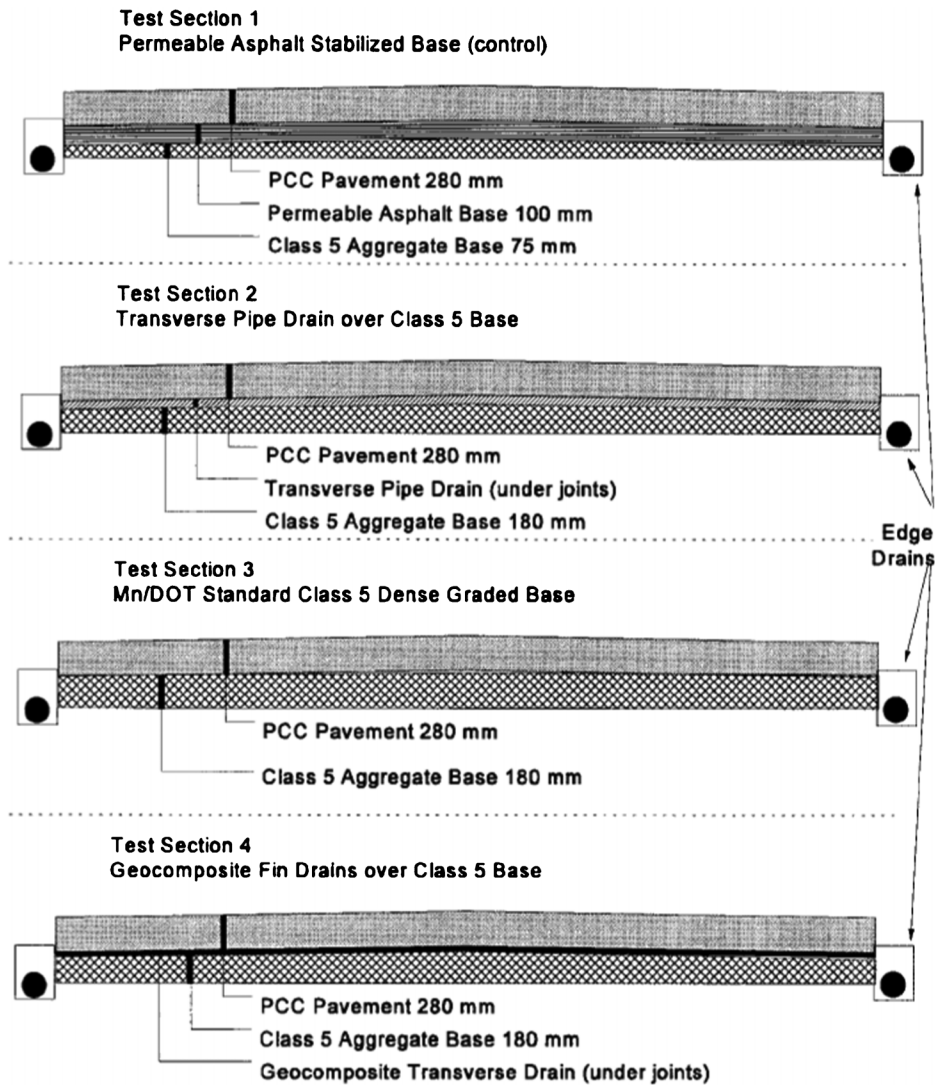
Figure 3.3 Pavement drainage systems (*11*).

Ground Penetrating Radar (GPR) is a high resolution geophysical technique that utilizes electromagnetic radar waves to locate and map subsurface targets, including buried drainage systems. GPR operates by transmitting short pulses of electromagnetic energy into the pavement. These pulses are reflected back to the radar antenna. The amplitude and arrival time are related to the depth of targets and surrounding material properties (*9*). GPR can also be called "ground-probing radar," "sub-surface radar," or "surface-penetrating radar (SPR)" depending on the application.

Figure 3.4 Typical hidden outlet pipe (*14*).

TABLE 3.1
AASHTO Drainage Criteria (*11,15*)

Quality of Drainage	Water Removed Within
Excellent	2 Hours
Good	1 Day
Fair	1 Week
Poor	1 Month
Very poor	Water will not drain

3.3.2 History and Applications of GPR

GPR was first developed in the early 1970's for military applications such as locating underground tunnels. Since then, it has been used in a broad array of applications including locating landmines and unexploded munitions, performing contaminant mapping and ground water analysis, studying glaciers and other ice formations, and carrying out infrastructure and material profiling. Locating underground utilities (in this case drainage systems) is thus only one of many applications for which the technique has been applied.

An overview of peer-reviewed literature related to several primary GPR application areas is presented below, highlighting some of the key insights borrowed from these fields for the work pursued in this study.

Agriculture and hydro-geophysics. Ground penetrating radar has been used extensively to assess the hydraulic properties of the subsurface that control underground water movement and the spread of chemicals that enter the groundwater system. In this arena, multiple researchers have successfully measured hydro-geological properties critical to agriculture and environmental fate and transport at the field scale using GPR (e.g., (20–24)). GPR has also been applied in other aspects of agriculture, such as monitoring the movement of agrochemicals (25); mapping the soil spatial variability of agricultural fields (26); quantifying the impact of hydrology on crop production (27); and detecting produce in cultivated soils (28). In addition, GPR has been employed in agricultural contexts highly related to this research to detect and locate agricultural drainage pipes (2,28,30). While knowledge of the characteristic signal return patterns from drainage pipes are quite similar to those seen in sub-pavement drainage applications, agricultural conduits are typically located quite close to the ground surface, are often large in dimension, and are buried beneath simple soil strata (vs. multiple pavement layers of varying material properties), making related findings of limited value for the application pursued herein.

Archaeology. As a nondestructive geophysical survey method, ground penetrating radar has multiple advantages in archaeological studies, and has been used extensively to detect underground structures and buried objects without causing damage. Both 2-D and 3-D GPR surveys are widely employed in archaeology (31,32), with related work encompassing both urban areas (33) and more rural field settings (34,35). GPR modeling and simulation are also common in archaeology (36). In archaeology, archaeologists often employ pattern recognition algorithms to GPR data to search for signals indicative of manufactured rather than naturally occurring subsurface features. This same principle is employed in the background/ clutter reduction algorithm employed in this study.

Mine detection. GPR is widely used for the detection of metallic, plastic, and wooden mines. Several automatic mine detection algorithms have been developed within this application area, including algorithms based on fuzzy logic (37) and systems designed to make use of limited data (38). Bruschini et al. (39) introduced a combined GPR and metal detector sensor system to increase mine detection accuracy and reduce false alarms when searching for metallic mines. Montoya and Smith (40) introduced a GPR system based on Resistively Loaded Vee Dipoles, which greatly reduced antenna related clutter and enhanced detection sensitivity for anti-personnel mines. Earp et al. (41) performed a study of metallic mine detection effectiveness using an ultra-wideband GPR system. Sun and Li (42) introduced a time-frequency analysis technique to detect buried plastic landmines. Beyond these efforts, some of the greatest successes in landmine detection accuracy are a byproduct of digital signal processing (DSP) techniques such as the non-uniform fast Fourier transform (NUFFT) based migration method (43); the Kalman filter based DSP approach (e.g., (44)); and the hidden Markov models (HMMs) method (45). Several of these techniques, or their variants, are employed in this work.

Road evaluation. Because of the fast processing and nondestructive nature of ground penetrating radar, it is also widely used in the transportation area, especially for road evaluations. One of the most common applications is pavement thickness evaluation both during construction and once roads are in service, and several compact, low cost GPR systems and theoretical analysis models have been developed for this purpose (46,47). GPR has also been used to evaluate the nature of the subgrade soil and stratigraphy underlying roadways (48); to assess pavement quality, through evaluation of pavement layer properties, detection of under-pavement air voids, and estimation of crack prevalence in roads (48,49). GPR is also applied to detect and evaluate pavement layer stripping, especially for asphalt concrete pavements (5,50). Among the many contributions to the technology in this area of application are developments that have enabled successful air coupling of the GPR signal with the roadway which have enabled non-static tests that make application of the technology to evaluation of extensive highway networks practical from a time and cost perspective.

4. EQUIPMENT OVERVIEW

4.1 Introduction

In this effort, equipment was acquired to assemble an enhanced GPR unit capable of utilizing multiple transmitter and receiver antennae operating at varying frequencies to develop an image of the subsurface. The key aspects of this new hardware are described in detail below.

4.2 Overview of GPR Equipment

To enable the multi-antennae capability desired for this effort, a new GPR control unit, the SIR-30, was purchased from GSSI Inc. This unit was selected due to its features and compatibility with existing INDOT equipment, and offers the ability to collect data from 4 different channels at the same time. This allows simultaneous collection of data from different frequency antennae, facilitates use of a Multi-input Multi-output (MIMO) antenna array, and also enables the comparison of data at different antennae polarizations. The key components of this system include the following:

1. Main Control Unit (SIR-30): enables 4 antennae to work at the same time.
2. LCD Digital Monitor together with Keyboard and Mouse (or a laptop with an Ethernet cable connection): facilitates user interface with control unit.
3. Antennae with Distance Measuring Instrument (DMI): together with SIR-30 control unit, the antennae and DMI create a complete location-indexable Tx-Rx system.

Main control unit (SIR-30). The SIR-30 control unit serves as the center of the GPR system used in this research, enabling simultaneous operation of

4-channels, as well as high data transmission speed and improved data resolution. The maximum pulse repetition frequency (PRF) that can be transmitted by the SIR-30 is $\sim$ 733 KHz, which means the system can collect $\sim$ 3/4 million samples per second. However, the actual data collection rate pursued in lab experiments and field surveys varied based on the PRF of each antenna and the desired density of data collection points. Based on the combined capabilities of the control unit and antennae, the average vehicle speed for a field survey is likely limited to around 3-4 miles per hour to ensure capture of quality data with a resolution of roughly at 48 traces/ft. The control unit also has a 32-bit A/D unit which enhances detection sensitivity relative to pre-existing INDOT equipment.

Figure 4.1 provides an image of the SIR-30 unit. This unit can be controlled by a laptop connected by Ethernet cable, which enables convenient use in the field. Also this unit itself is a personal computer. So, with an interface LCD monitor and input devices (keyboard and mouse), it can be self-controlled, which increases data transmission and storage speed, which are again valuable benefits in the field.

The unit dimensions are $17.7 \times 13 \times 5.1$in ($45 \times 33 \times 13$cm) and it weighs only 18.5 lbs (8.4 kg).
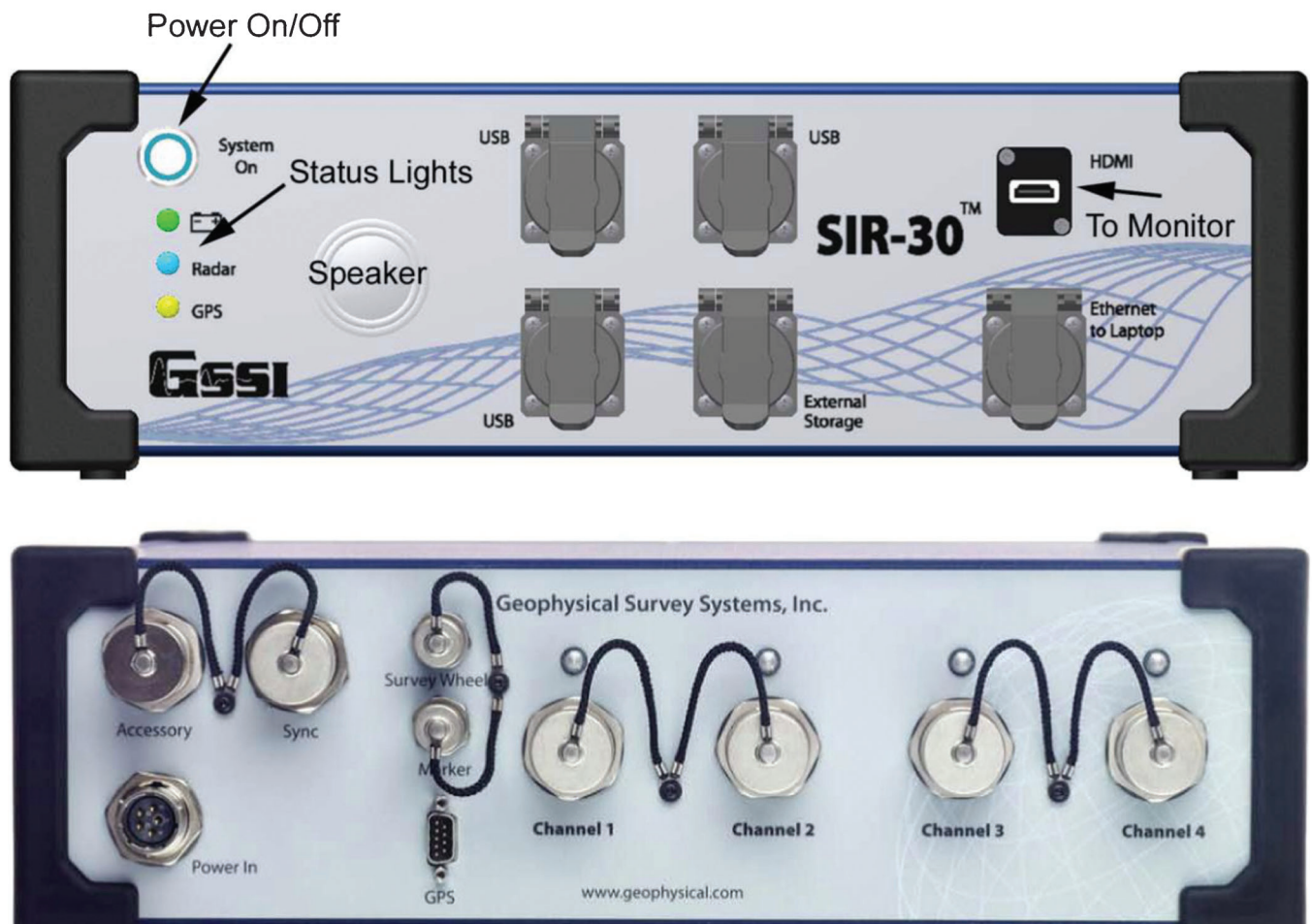

Figure 4.1 Front and back view of SIR-30 control unit (GSSI SIR-30 Manual).

GPR antennae. Based on the required resolution and depth of penetration for the pavement drainage application, antennae of three different frequencies will be employed in this research, 900 MHz, 400 MHz, and 270 MHz. Each of the antennae are pulsed radar devices; the original signal they generate is a simple Ricker pulse. An illustration of an integrated antenna box is shown in Figure 4.2. Each antenna box contains separate transmitter and receiver antennae, one control unit connector, and two Distance Measuring Instruments (DMI) with connectors for different DMI survey wheels.

This design makes it possible to build a MIMO GPR system, in which the transmitter and receiver can be controlled individually.

Outfitted with a suitable DMI survey wheel, the antennae can be run in distance mode or continuous time mode. The former mode provides the exact horizontal position of imaged targets. In continuous time mode, antennae transmit signals based on a time clock signal, which is useful in static tests without antennae movement. Most GPR surveys require the movement of the antennae to obtain data at different positions along the survey line. As a result, traditionally, a constant travel speed must be carefully maintained in order to receive stable shapes in the reflected signal, which is not straightforward in practice. However, together with the DMI, the antennae can transmit signals and track position in the distance control mode. Because the antenna position can then be determined very easily, the speed will not influence the shape of the received signals, simplifying field operation.

Model 3101 900 MHz GPR antenna. This antenna with a central frequency of 900 MHz is designed for applications requiring high resolution but shallow penetration depth (GSSI Inc. Manual). (Dimensions of the integrated antenna box are $13 \times 7.5 \times 3.5$ inches ($33 \times 20 \times 8$ cm)). Figure 4.3 shows the Model 3101 900 MHz antenna attached to a Model 611 survey wheel. The pulse duration of the source signal is 15ns. The effective penetration depth is between 0 and 6 ft depending on the dielectric permittivity of encountered materials.

Model 5040 400 MHz GPR antenna. This antenna with 400 MHz central frequency, shown in Figure 4.4, is a mid-frequency GPR antenna designed for greater

Figure 4.3 Model 3101 900 MHz antenna attached to a Model 611 survey wheel.

penetration depths, but with decreased resolution compared to the high frequency antenna. The dimensions of the entire antenna unit are $12 \times 12 \times 6.5$ inches ($30 \times 30 \times 17$ cm). The transmitted pulse duration of this antenna is 25ns, and the effective penetration depth is 0 to 16 ft depending on the dielectric permittivity of encountered materials.

Model 5104 270 MHz GPR antenna. This antenna is designed for deeper penetration with a 270 MHz centered frequency. The dimensions of this antenna case are $17.5 \times 17.5 \times 7.5$ inches ($44.5 \times 44.5 \times 19$ cm). The transmitted pulse duration is 3.6ns and the effective penetration depth is 0 to 25 ft depending on the dielectric permittivity of encountered materials. The application of this frequency is normally for large targets buried at greater depths.

Model 611 survey wheel (DMI). Compared to a typical survey cart used in the field with large wheels (about 12 inches in diameter), the wheel size of this equipment is quite small—about 3.83 ($3\frac{5}{6}$) inches in diameter which is a suitable size to be used in

Figure 4.2 Schematic of an integrated antenna box produced by GSSI, Inc.

Figure 4.4 Top view of Model 5040 400 MHz GPR antenna.

laboratory tests. It can be attached directly to the 900 MHz antenna box (Figure 4.3) and also can be used together with 400 MHz antenna. The maximum control rate of this wheel is about 609.6 ticks/foot (2000 ticks/meter), which means this wheel can control the antennae to transmit at most 2000 signals per meter.

4.3 Standard Testing Procedures

As described above, the GPR system used in this project contains several components. Before carrying out lab or field experiments, correct integration of the system must be completed. The general procedures to prepare the multi-channel GPR system for use are straightforward and can be summarized as follows:

1. Attach a DMI survey wheel to each of the antenna boxes to be used in the test and connect them with a suitable cable;
2. Connect all antennae needed in the experiment to the main SIR-30 control unit using supplied and appropriately connectorized cables;

Choose one from 3 and 4:

3. If using monitor to control the unit directly, connect a digital LCD monitor to the SIR-30 main body with an HDMI cable, as well as the necessary input devices, such as a keyboard and mouse;
4. If using a laptop to run the unit, first set up the laptop as a client computer which can communicate to the main body of SIR-30, then connect the laptop to SIR-30 with an Ethernet cable;
5. Plug in all source power connections on the monitor or laptop, then the SIR-30 control unit;
6. Open the SIR-30 control program to identify necessary parameters of all connected antennae;
7. The system is now ready to perform a survey.

5. OVERVIEW OF SIMULATIONS AND EXPERIMENTS

5.1 Introduction

The work carried out in this program involved a two-pronged approach to improve GPR-based sub-pavement drainage system evaluation while maximizing the value of INDOT's pre-existing investment in GPR hardware and remaining within project budget limitations. Specifically, two major avenues were explored to achieve improvements in GPR detection success: (1) software-based signal processing and (2) modifications of hardware test configurations (see Figure 5.1). Simulations and experiments were employed throughout this work as an efficient means to assess the potential benefits and limitations of these improvement efforts under various test conditions.

5.2 Simulation and Experiment Design Factors

Two main sets of variables which influence GPR observations were considered in different simulation and experimental contexts: Environment factors and Equipment factors.

Environment factors

Drainage conduit type and size. Subsurface drainage systems encountered in the built environment vary widely and may range in size from just a few to tens of square centimeters in cross section. Further, drainage conduits may be concrete, clay, or plastic pipe (e.g., transverse or longitudinal pipe drains) or geo-textile composites (e.g., geo-composite edge drains or permeable layers).

Drainage conduit installation geometry. Sub-pavement drainage systems may be oriented in a transverse or longitudinal direction relative to the roadway and must be installed at a slope steeper than 0.2% for subsurface drains and 0.3% for outlet pipes; different geophysical techniques may be required to rapidly locate drains in these two distinct orientations.

Soil type and sub-grade type. Although most primary road designs share common design principles, the sub-grade materials can vary location to location based on availability and their bulk dielectric properties can potentially be influenced by aggregate compaction and infiltration by other soils (the more conductive the soil, the greater the radar attenuation).

- Highly conductive soil: Water saturated (wet) soil or highly salty soil (e.g., where salt is used for ice melting)
- Clay dominated soil: usually includes significant moisture, making it highly conductive
- Silt dominated soil: usually found in topsoil, containing some amount of moisture, making it moderately conductive—less likely in primary road scenario
- Sand dominated soil: containing little moisture, and hence low conductivity
- Granular and compacted soil: usually found under paved areas, very low conductivity

Pavement material (HMA or WMA, concrete). Clearly primary road surfaces may take on an array of forms related to varying formulations of hot (warm) mixed asphalt or concrete.

Strata thickness and conduit depth. Again, primary road layer thickness and the resulting location of subsurface drainage conduits can vary based on road design.

Equipment factors

Arrangement and number of GPR transmitters and receivers. GPR surveys can be performed in a variety of ways (e.g., common offset, multi-offset) that each maximize the response from some sub-surface features and minimize the response from others.

Coupling geometries. GPR can generally be air-coupled or ground-coupled into the subsurface; the choice of coupling method involves a compromise between coupling efficiency and testing speed.

Operating frequency range (commonly from 10 MHz to more than 1,000 MHz). Although GPR is generally viewed as the geophysical method with the
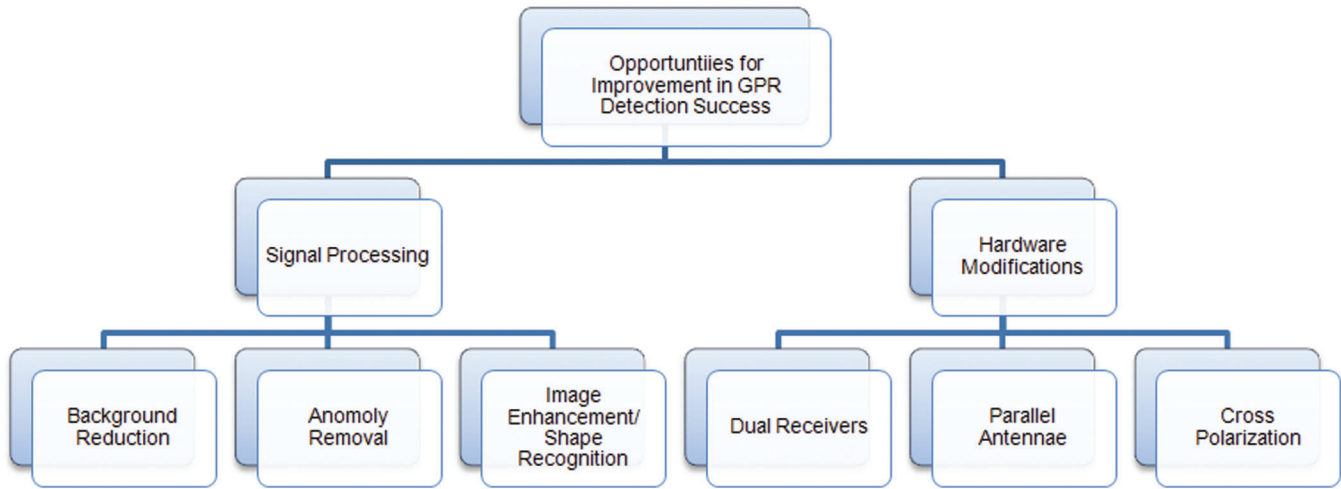
Figure 5.1 Avenues of potential improvement in GPR detection success.

highest resolution for imaging the subsurface (with centimeter scale resolution possible in some circumstances), there is an inevitable trade-off between resolution and penetration depth, driven by operating frequency. Depth of investigation increases with decreasing frequency but at the cost of decreased resolution. While GPR waves can reach depths of 30–40 m in materials such as ice or volcanic rock, they may penetrate only 1–2 m in materials such as clay or shale.

Absolute vs. relative measurements. While it would be ideal to obtain absolute measurements with any sensing system (that is measurements that are accurate and definitive at a single point in time), under some circumstances relative measurements (that is subsequent measurements compared to each other) may prove useful in difficult sensing conditions and could yield insight (for example, scanning the sub-surface before and after rainfall to find variations in subsurface moisture that may help locate drainage conduits).

5.3 Computer-based Electromagnetic Simulation

5.3.1 Overview

In addition to the performance of lab or field experiments, simulations were carried out using GPRMAX2D software (Copyright 2005 by Antonis Giannopoulos). GPRMAX2D is an electromagnetic wave simulation software package for Ground Penetrating Radar models designed by Dr. Antonis Giannopoulos of the University of Edinburgh, UK. This simulator is based on the Finite-Difference Time-Domain (FDTD) method. Simulations were employed throughout this work for multiple purposes including the design of the in-laboratory test basin, exploration of the influence of road cross-section designs on radar signatures, and evaluation of alternate GPR antennae configurations. In particular, simulations offer the advantage of modeling situations with infinite boundary conditions, which eliminates the influence of even subtle side reflections that might be encountered in a scaled down laboratory experiment that must inevitably be "contained."

5.3.2 Simulations with Infinite Boundary Conditions

Two simulations in particular were pursued to determine the influence of water and pavement cover on GPR observations of sub-pavement conduits and are highlighted here. The depth of pipes (PVC) was set at 0.6m, which is a reasonable depth based on typical road cross-section design. The dimensions of the simulated area were chosen to enable inclusion of 3 different diameter pipes, located with enough distance (0.75m in the models) between them to avoid relative interference. The antennae of GPR unit were simulated to move along the ground surface in the simulation models. The data collection rate was one trace per 0.03 meters. Two different offsets (along the horizontal direction) between the transmitter and receiver were considered in both models, 0 meters and 0.2 meters.

Schematics of these two models are shown in Figure 5.2. The size of the simulated area is 3m (L) × 0.8m (D). There are 3 PVC pipes involved; with diameters of 4″, 6″ and 8″, respectively. Side and bottom boundary conditions for the calculation area were absolved infinite boundaries. In addition, a free boundary is modeled at the surface. As illustrated in Figure 5.2 below, Model 1 involves only sand and no pavement cover. One concrete pavement layer is introduced in Model 2. While these models are obviously simplified relative to an actual road cross-section, they help to assess fundamental geometric and material impacts on different GPR test configurations. In particular, several groups of simulations have been analyzed for each model involving important factors such as radar frequencies, antennae offset, and water conditions in the sand (saturated or dry). Table 5.1 provides the details of the analyzed simulations.
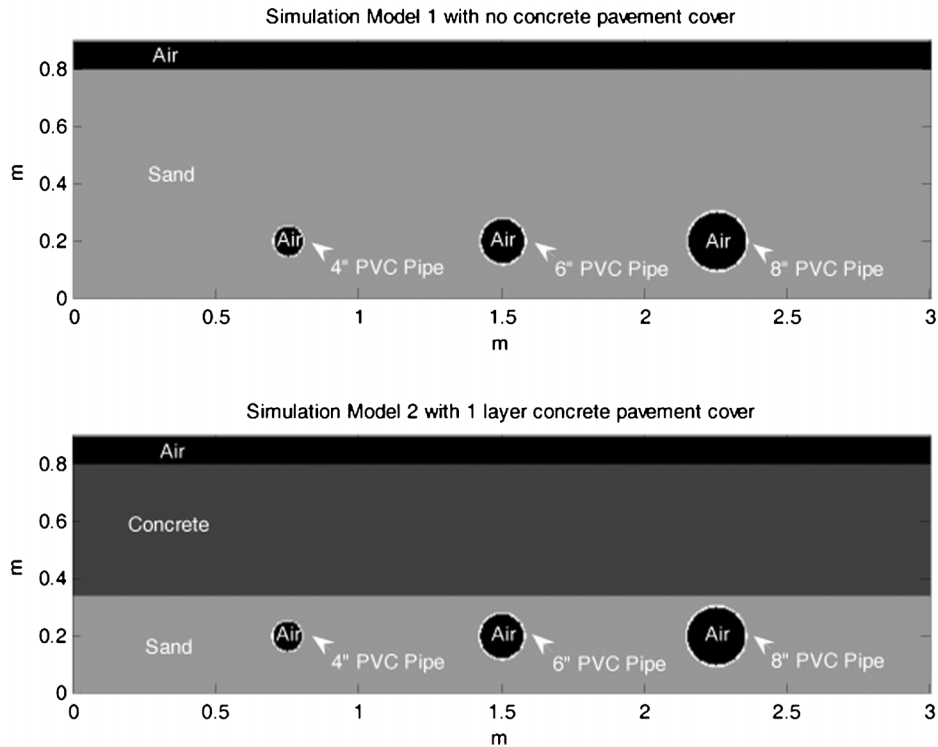
Simulation Model 1 with no concrete pavement cover

Simulation Model 2 with 1 layer concrete pavement cover

Figure 5.2 Schematics of simulation models: No pavement cover (top) and concrete pavement cover (bottom).

As shown in Table 5.1, 12 different simulations have been analyzed with different key parameters. Figures 5.3 (a-f) and 5.4 (a-f) provide all the analyzed results, for Models 1 and 2, respectively. In all the following figures, the horizontal axis represents the trace number along the scan direction. The vertical axis represents the time axis, which provides the arrival time of reflected signals in the unit of nanoseconds. All the hyperbola shapes in the simulation results indicate reflection signals of potential targets.

Comparing all the sets of simulation results, there are several conclusions that can be drawn, as follows:

- Simulations with 0.2 meters offsets between the trans- mitter and receiver can help improve the GPR results

significantly, especially with saturated soil conditions. As shown in Figure 5.3 (c), when using the 900 MHz antennae with Model 1 involving saturated sand and a 0m offset between Tx and Rx, the target is very hard to detect. However, in Figure 5.3 (f), which has the same soil conditions as 5-3 (c) but with 0.2 meters offset between Tx and Rx, the three targets are clearly found. The reflection delay from targets in saturated sand is much longer than for the dry sand, which is shown in Figure 5.3 (d). In dry sand the delayed reflection time is around 8ns (Figure 5.3 (d), but in saturated sand it varies from 16ns to 18ns (Figure 5.3 (f), due to the fact that EM waves travel much more slowly in water than in dry materials (sand in this case).

- Based on the simulation results, a concrete pavement layer will decrease the resolution of GPR images under

TABLE 5.1
Details of Analyzed Simulations and Related Parameters

Model	Antennae Offset (m)	Operated Frequency (MHz)	Water Conditions of Sand (Dry or Saturated)	Simulation No.	Result Figure No.
Model 1	0	900	Dry	1-0-900D	5-3 (a)
		400	Dry	1-0-400D	5-3 (b)
		900	Saturated	1-0-900S	5-3 (c)
	0.2	900	Dry	1-0.2-900D	5-3 (d)
		400	Dry	1-0.2-400D	5-3 (e)
		900	Saturated	1-0.2-900S	5-3 (f)
Model 2	0	900	Dry	2-0-900D	5-4 (a)
		400	Dry	2-0-400D	5-4 (b)
		900	Saturated	2-0-900S	5-4 (c)
	0.2	900	Dry	2-0.2-900D	5-4 (d)
		400	Dry	2-0.2-400D	5-4 (e)
		900	Saturated	2-0.2-900S	5-4 (f)
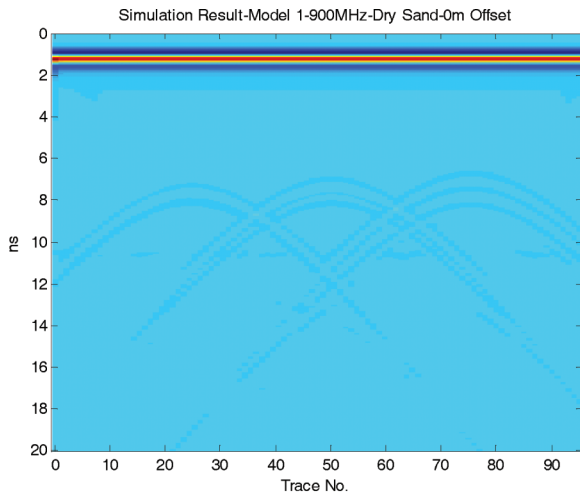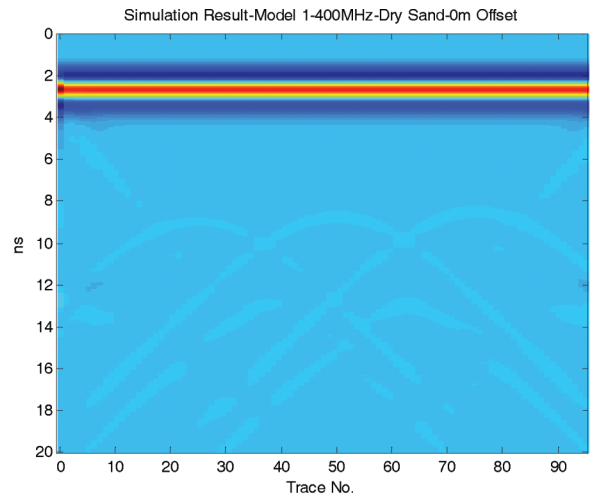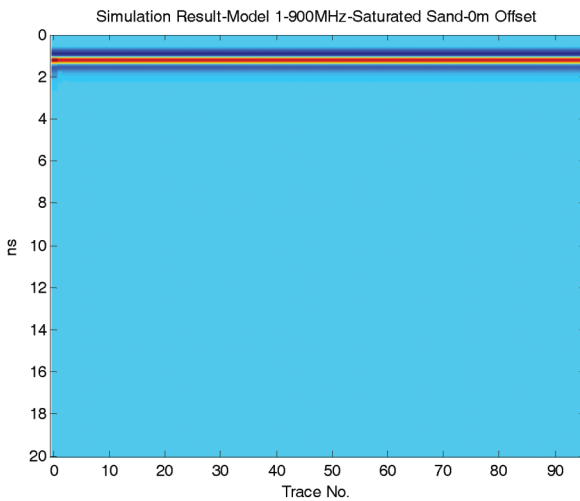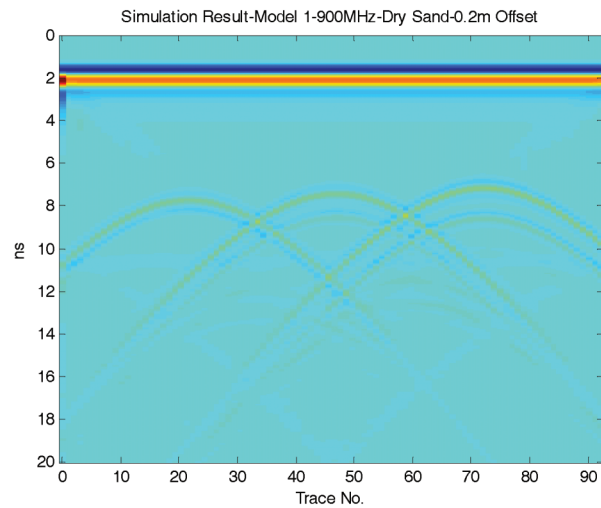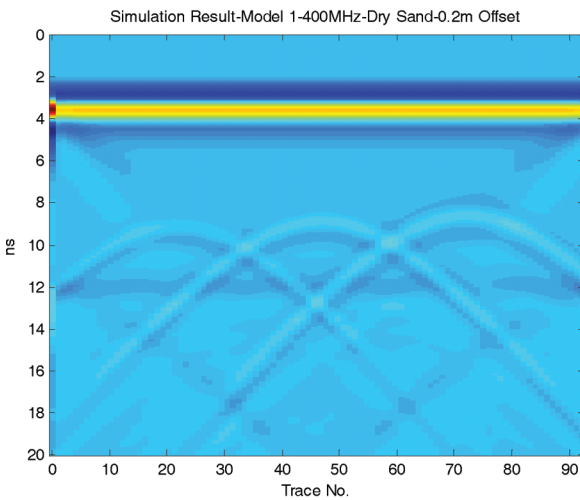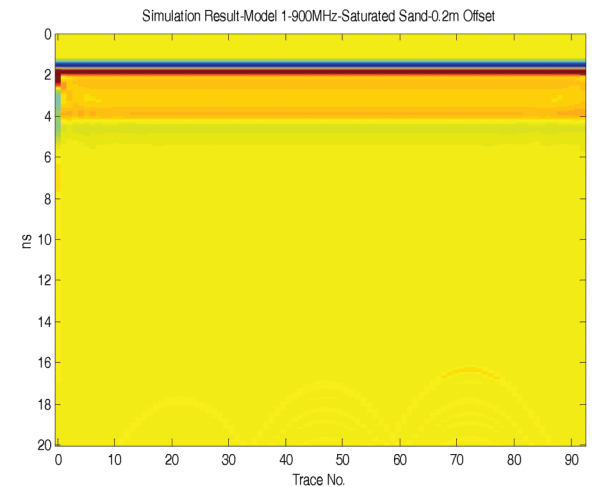
Figure 5.3 Simulation results of Model 1: Sand only.
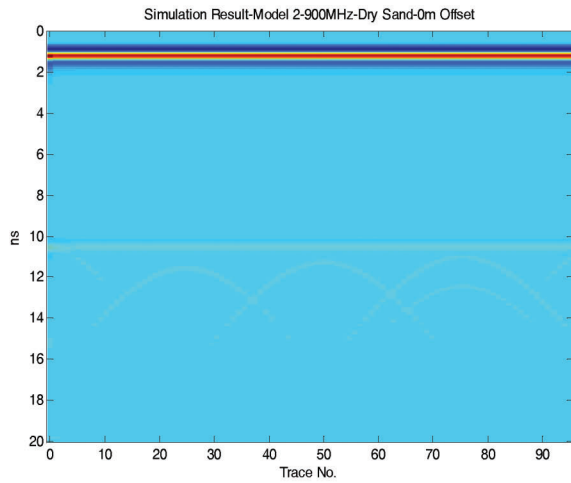
(a) 2-0-900D
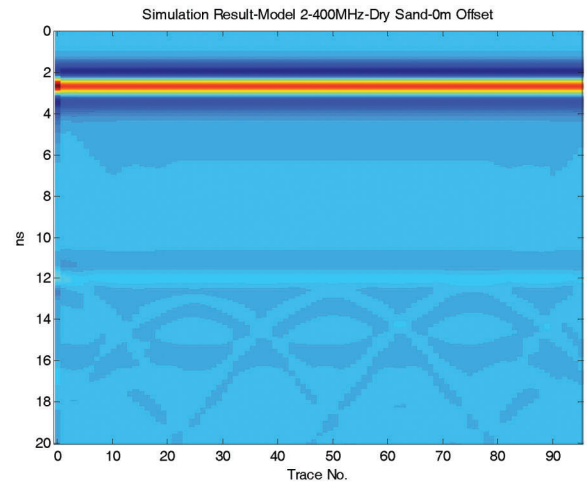
(b) 2-0-400D
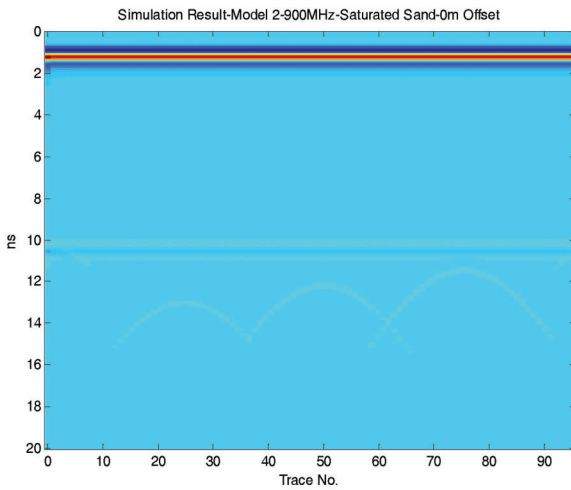
(c) 2-0-900S
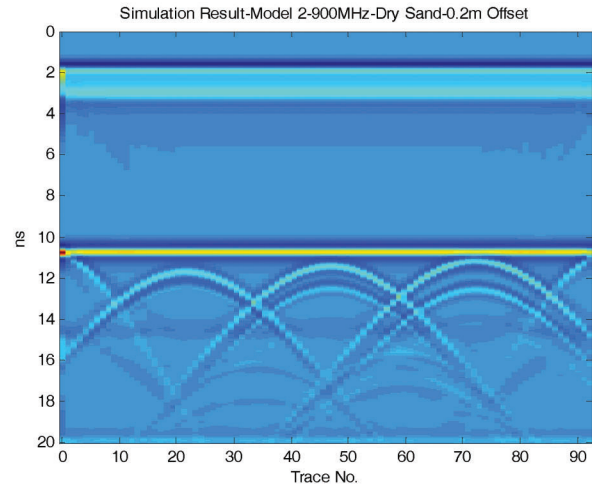
(d) 2-0.2-900D
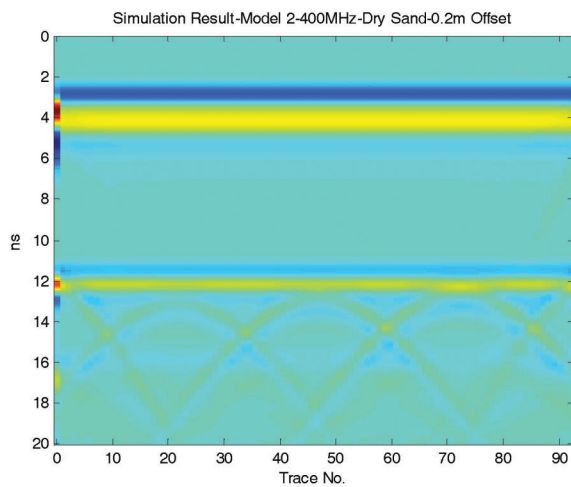
(e) 2-0.2-400D
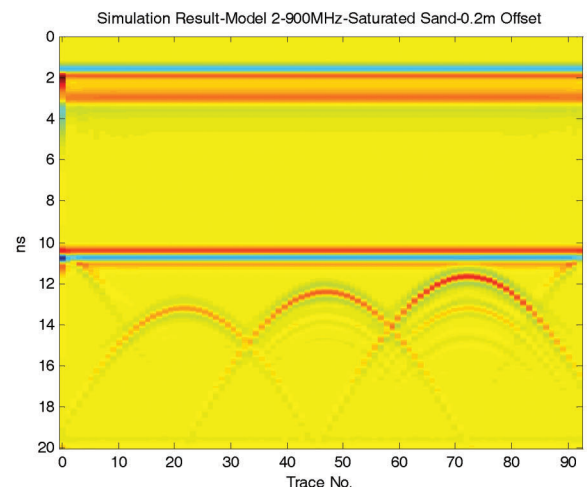
(f) 2-0.2-900S

Figure 5.4 Simulation results of Model 2: Sand with concrete cover layer.

dry sand conditions, as shown by comparing Figure 5.3 (a) and Figure 5.4 (a). With 0.2m offset of the Tx and Rx, the results improve as shown in Figures 5.4 (d) and (e).

An interesting preliminary finding revealed in the simulation is that the quality of the GPR results improves under both 400 MHz (Figure 5.4 (e)) and 900 MHz (Figure 5.4 (f)) analysis when pavement cover is present. The improved images are again generally associated with a 0.2 meter offset between Tx and Rx. These observations are discussed again later in the context of the field experiments.

Details of additional simulations are provided where relevant throughout the report.

5.4 Laboratory Experiments

Lab experiments are an efficient means to proof test equipment, simulate situations likely to be encountered in the field, and assess possible solutions to identified detection or operational challenges. With this in mind, a simple in-laboratory test basin – that is a vessel that contains the soils and other materials used to represent any given field scenario—was designed and fabricated for use in this program.

5.4.1 Test Basin Design

The design of the test basin took advantage of insights gained through work by other researchers who have performed in-laboratory GPR experiments (51–53). Their work was particularly valuable in highlighting means to manage water/liquids in a test apparatus, defining appropriate dimensions for an effective in-laboratory test setup, and managing air-launched GPR antennae when working at a laboratory scale.

Even with the benefit of past studies, effort was placed on ensuring that the test basin used here was appropriately sized and designed. The main concern here is the potential for the walls of the vessel to create side reflections of electromagnetic (EM) energy that could interfere with observations of targets in the test medium. In addition, several other factors associated with the design of the test basin can influence the data

collected by GPR, such as the material from which it is fabricated, and the nature of the soil, aggregate, and roadway materials that it contains.

To assess these variables simulations were carried out using the GPRMAX2D software described above. Simulations performed encompassed the following ranges of key variables:

1. Since the depth of drainage conduits below pavement is normally in the range of 0.5m to 1m, initial simulations were performed assuming a depth of 1m which provides a conservative bound for basin design.
2. Several potential fabrication materials were considered for the experimental basin, such as, (1) a simple metal box, (2) a simple wooden box and (3) a canvas box supported by round metal bars. (Note that steel was used as a test material to verify model function based on steel's "mirror-like" reflection of electromagnetic waves).
3. Finally, several key boundary conditions associated with selected basin materials were also explored. Possible boundary effects caused by the use of a test basin could include, (1) sidewall reflections (e.g., from the walls of a metal box), (2) bottom reflections (e.g., from a steel support plate below the basin), (3) support reflections (e.g., from metal bars used to support a canvas box) and (4) corner reflections (e.g., from the edges of the basin).

To explore possible designs, three different basin sizes were analyzed involving differing width to depth ratios and different wall materials as summarized in Table 5.2. Figures 5.5 (a)–(c) illustrate the geometries of the three simulated models. In these simulations, the GPR antennae are simulated to move along the surface of the experimental basin, and the data collection rate is 1 trace per 0.03 meters. Moreover, there is no offset between transmitter and receiver in these simulations because it is assumed that they are performed with a standard Tx/Rx antenna unit, in which the transmitting and receiving antennae cannot be physically separated.

In general, the results of the simulations generated based on the factors above can be expressed as a function of (1) the fabrication material and dimensions of the designed basin and (2) the operating frequencies of the GPR antennae (400 MHz and 900 MHz).

Simulation results for the different models are shown in Figure 5.6 (a)–(h) as follows.

TABLE 5.2
Simulation Parameters for Experiment Basin Size Determination

Model	Descriptions	Basin Sidewall Material	Antenna Frequency (MHz)	Result Figure No.
A	W = ~2D	Metal	900 MHz	Figure 5.6 (a)
			400 MHz	Figure 5.6 (b)
B	W > 2D	Metal	900 MHz	Figure 5.6 (c)
			400 MHz	Figure 5.6 (d)
C	W ≪ 2D	Metal	900 MHz	Figure 5.6 (e)
			400 MHz	Figure 5.6 (f)
		Canvas / Dry Wood	900 MHz	Figure 5.6 (g)
			400 MHz	Figure 5.6 (h)

NOTE: W = width of designed basin; D = depth from surface to the top of target pipe.
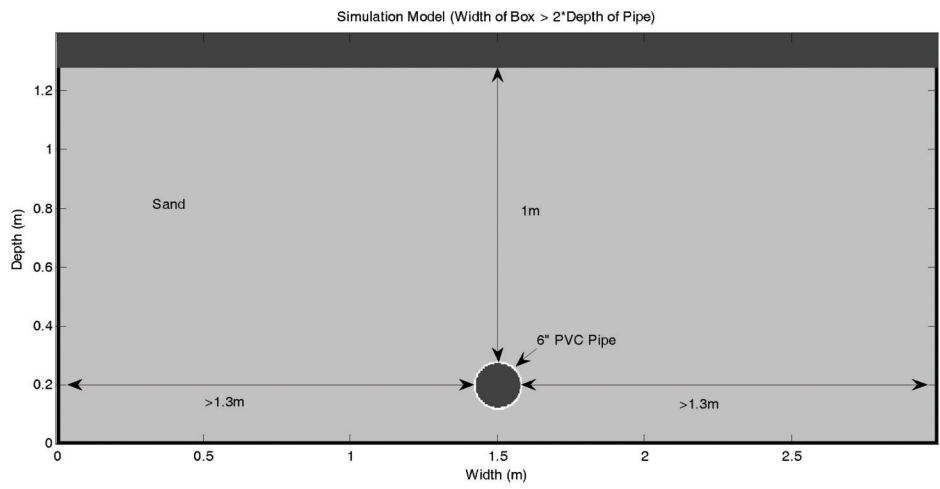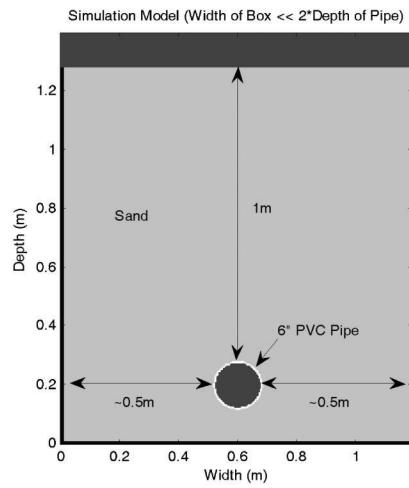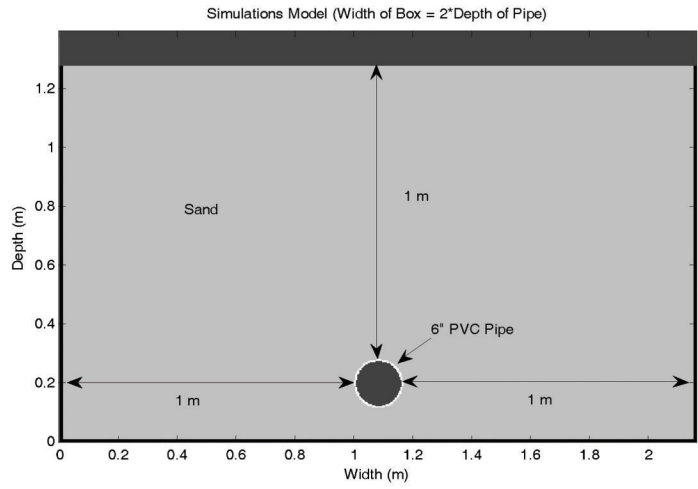
Figure 5.5   Geometries of simulated models for experimental basin size determination.
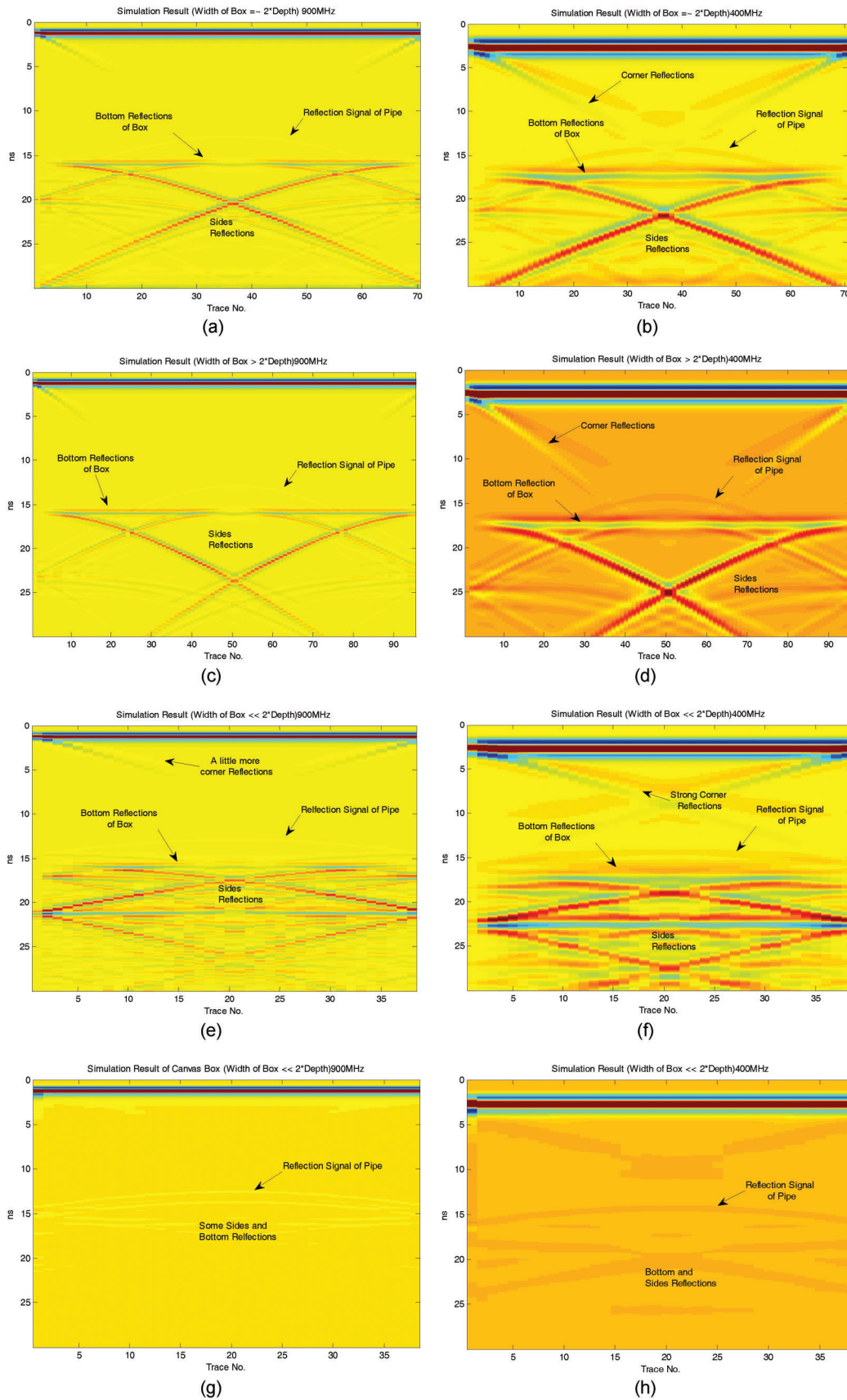
Figure 5.6   Results of basin size simulations (continued).

Several findings are notable:

- Recognizing that the EM radiation emitted from the GPR antenna will obey Snell's Law when interacting with an EM reflective surface, the reflections of flat walls and round support bars would be expected to follow very different paths, as discussed in detail in the following paragraphs.
- In nearly all of the simulations, side reflections of emitted EM radiation appear at the transceiver after the bottom reflection since reflections must obey Snell's Law, and will thus not influence the pipe reflection signal (see Figure 5.7). Even for the smallest basin (Model B), the side reflections still arrive after the bottom reflection, although there is evidence of some convolution when a 400 MHz antenna is employed. The same is true for the signal reflected directly from bottom of the basin.
- Comparison of the 400 MHz (Figure 5.6 (b) (d) (f) (h)) and 900 MHz (Figure 5.6 (a) (c) (e) (g)) antenna simulations indicate that corner reflections are much stronger when the 400 MHz antenna is employed. In Figures 5.6 (b) and (d), corner reflections can be observed that are strong enough to influence the return signal from pipe, which could lead to errors in a real test. This problem is particularly pronounced in Figure 5.6 (d), in which the corner reflections cross above the signal from the pipe—creating a signal that could be misinterpreted as another parabolic reflection from a pipe. These reflections likely stem from the upper structural edge of the test basin.
- The size of the test basin remains as the most important factor in producing a field representative in-lab test setting. For the smallest model (Model C), side reflections are much more complicated than the other two larger sized models, which significantly complicate target signal determination. This problem is compounded with the 400 MHz antennae, as shown in Figure 5.6 (e) (f). However, different basin materials can influence the side effect significantly. The wooden or canvas basic reduces these reflections enough to analyze buried pipes based on the smallest size design above (Model C), as shown in Figure 5.6 (g) and (h).

Based on the analysis above, a simple wooden box, slightly elevated above the floor, was used as the lab experimental test basin in this project. Details of this
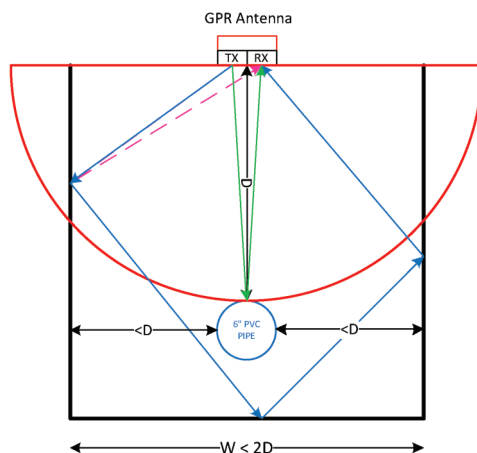
Figure 5.7 Illustration of side reflections vs. pipe and bottom reflections in test basin simulation.

lab test basin will be introduced as necessary in subsequent sections of this report.

5.4.2 Test Basin Preparation Procedures

Based on the key parameters indicated above, the test basin must be filled with controlled materials before an experiment is conducted. The general procedures for this activity are as follows.

1. Choose the cross-section of pavement that is to be simulated, such as the shoulder, pavement surface, or side slope;
2. Design this selected cross-section based on the road design manual, employing different materials for the various base layers as required; for example for the side slope of the pavement, drainage pipes would be buried only by soil, but not gravel layers and a top pavement surface;
3. Determine desired water conditions in the soil based on the desired real field conditions; such as saturated after rainy weather, dry conditions in the high temperature period of summer, or intermediate partially saturated conditions;
4. Design pipe positions, depth and line directions; outlet drainage pipes would appear at different positions and depth based on which part of road is simulated; meanwhile, the choice of the pipe line direction in this limited sized basin can be varied to simulate different survey line angles (parallel, perpendicular and angle α);
5. Place all controlled materials into the test basin in the appropriate order: base sand, pipes with defined direction located at determined depth, gravel subbase, gravel base and top pavement surface (if necessary);
6. The cross-section is now ready for testing.

5.4.3 Test Basin Data Set

The test basin was employed in this work for a variety of proof testing activities and to develop data sets representative of desired field conditions that were not necessarily available or readily accessible in the field. While the majority of analyses discussed herein will focus on actual field data, laboratory acquired data is referenced where additive to the discussion.

5.5 Acquisition of Field Data

Multiple field surveys were performed in this research to acquire data sets from actual roadways in Indiana. For field tests, road cross-sections where the locations of subsurface pipes are well known and also marked were examined to facilitate data interpretation. Three types of drainage conduits can be encountered in the field, (1) transverse pipes, (2) longitudinal edge pipes, and (3) outlet pipes. Figure 5.8 provides a schematic of drainage system geometry and typical survey paths.

The outlet pipes on the shoulder and side slope of the pavement are considered the primary target in this work. Several of these data sets will be employed in this report to illustrate key analyses and findings:

Figure 5.8 Schematic plan-view illustration of drainage system configurations.

1. Route US-231: Here the survey line was about ¾ miles long. There were 4 PVC pipes (1 8″-diameter pipe and 3 4″-diameter pipes) involved in this test. Two antennae were used here, one 400 MHz antenna and another 900 MHz antenna.
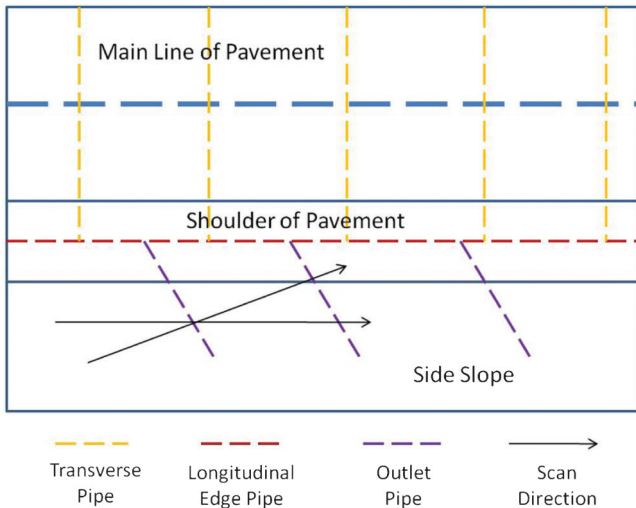2. Route I-65: The survey line of this test totals approximately 4.5 miles. Two types of drainage pipes were detected in this test, X-drains (newly installed, shallow PVC pipe) and K-drains (old deeply buried metal pipe). Here 4 antennae were employed, two 400 MHz antennae and two 900 MHz antennae.
3. New Route US-231: The survey line for this test was about ¼ mile long. There are two PVC pipes involved. The main purpose of this test was to examine different antennae configurations in the field. Both the original SIR-20 and SIR-30 GPR systems were used during this work. In total three different operating frequencies were tested here, 270 MHz, 400 MHz and 900 MHz. Four antenna configurations were examined in this work as well.

6. DIGITAL SIGNAL PROCESSING METHOD 1: BACKGROUND REDUCTION

As introduced above, there were two general investigative approaches pursued in this research to improve GPR system performance: digital signal processing and hardware experimentation. The following two chapters focus on the first approach, digital signal processing.

6.1 Introduction

This section focuses on employing unique signal processing methods to interpret lab and field data and enhance the quality of conclusions that can be drawn from any GPR data set. The main approach applied to the data involves an improved background and clutter reduction (subtraction) method relative to that employed directly by the GSSI GPR unit. This method is focused on interpretation of 1-D GPR results derived from the original 2-D GPR image along the survey line as a function of distance. While notably less complex than 2-D image analysis, it is believed that this treatment could provide a clear view of underground conduits below studied pavement. In addition, a second percentage-change-summation algorithm is also introduced to better manage anomalous signals. Just as with the first algorithm, the output of the second algorithm is also plotted in 1-D. The final result of a GPR scan is thus the combination of both outputs obtained by these two algorithms.

The methodology has been implemented through the development of a custom data analysis program. The program produces two major types of output based on the different algorithms: (1) GPR signal SNR values and (2) vertical sums of the percentage change in the GPR signal at measurement points along the horizontal survey line. By considering the probability distribution of obtained results, a detection threshold that effectively establishes the sensitivity of the system was defined. Numbers of detected target conduits and false alarms in a given GPR survey line have also been compared in sets of lab and field data to obtain views of optimal program parameters. Finally, multi-frequency results obtained along the same survey line were compared and combined in order to provide a final pipe position output with higher accuracy along any given survey line. Details of this methodology and related analyses are described in the following sections.

6.2 Related Literature Review

One advantage of GPR is the potential to detect non-metallic targets. However, the strength of the reflection signals from non-metallic targets is significantly weaker than that obtained from metallic targets of equivalent dimension and position. Further, the useful information about the target may be buried in the background of the signal, or so called clutter and noise in Radar theory. As a result, one of the key problems for this project is differentiation of the scattered signal of potential targets from the background interference, because the primary targets here are primarily non-metallic (PVC or clay) drainage pipes.

The background clutter and noise normally consists of three components: the breakthrough signals directly from transmitters to receivers; the reflections from the air-ground interface as well as the interfaces of different layers in the pavement and subsurface; the scattered signals from other non-related targets, such as rocks, air voids or unknown discontinuities in the subsurface (*54*). So the primary challenge in pipe detection as discussed herein is how to separate desired signals from background.

Several researchers have already put forward a number of methods to reduce background clutter and noise in GPR data sets, such as: simple mean scan subtraction (*55*); complex average subtraction (*56*); moving average

background removal (57); HHkkkHKalman Filter-Based approach to Target-Background Separation (58); background removal using Singular Value Decomposition (SVD) (54), Eigenvalues (59); the likelihood ratio test (55,60); the whitening filter (61); the median filter (62); the fuzzy weighted background removal and target energy function approach (63,64); and the wavelet-based method (65,66).

The algorithm used in this effort is an improved moving average background reduction method, which is developed as described below.

6.3 Data Pre-Processing

The GPR data normally obtained from a GPR unit is a B-Scan radar image can be considered in the form of a matrix. An example is shown in Figure 6.1 which was obtained from a field survey located on highway US-231, near Purdue University. Each column of the matrix is a digitized single trace of a scan, which is a so called A-Scan in Radar theory, as shown in Figure 6.2.

As shown in Figure 6.1, the scattered pipe reflection signal, the hyperbola shape located approximately halfway across the upper $1/3^{rd}$ of the image, is likely to be detected in a very specific range of depth below the pavement assuming drainage pipe placement has been guided by accepted design principles put forward in the road design manual (9). Consequently, only a limited vertical interval of a GPR data set must be analyzed to detect conduit targets. Normally, the pipes are buried 0.5m to 1m under the surface of pavement. Thus the uppermost region of the data and data below a depth of approximately 1 m can typically be ignored (note that these thresholds can be modified as desired in the current algorithm). For example, in Figure 6.1, the pipe is detected around 10ns along the vertical axis, which corresponds to a depth of 0.5m. Furthermore, each A-Scan of a data set is digitized into 512 samples. In other words, there are 512 rows in the final data matrix, which could be plotted in a 2-D image as shown below. Thus for each A-Scan, only samples 50–200 (row 50–200) are selected from the data set and used in the final analysis, which is shown as the range between two red lines in Figure 6.1.

6.4 Algorithm 1: Improved Moving Average Background Reduction

6.4.1 Overview of the Algorithm

The method presented here is a moving average background subtraction approach as mentioned above. In this approach, at any given point of signal analysis along the survey line, a point termed the "checkpoint," an averaged A-scan background signature, is subtracted from the A-scan at that point to reveal the signal of interest. The "average" background signature is developed by examining data (a series of A-scans) in a region of finite length, w, along the survey line that is located a fixed column distance, d, behind the checkpoint. This region is called the background window. As the checkpoint is moved forward along the survey line, the background window remains a fixed column distance, d, behind the checkpoint, trailing the checkpoint in a manner that ensures its local relevance to the ground conditions in the region of the checkpoint. As a result, there are two key parameters related to this method, the size of the window employed to develop a background signature (i.e., the background window size), w, and the column distance between the checkpoint and the end of background window, d. A conceptual representation of this algorithm, as well as a related mathematical formulation, is shown in Figure 6.3.

For any given run of the signal processing algorithm, a set of values for w and d will be tested. During the test, the background window will start from the beginning of the data matrix, and the average of the signals within this window will be subtracted from a target signal d columns from the end of the background window. Then another window will start from the second column, the target will also move to next spot,
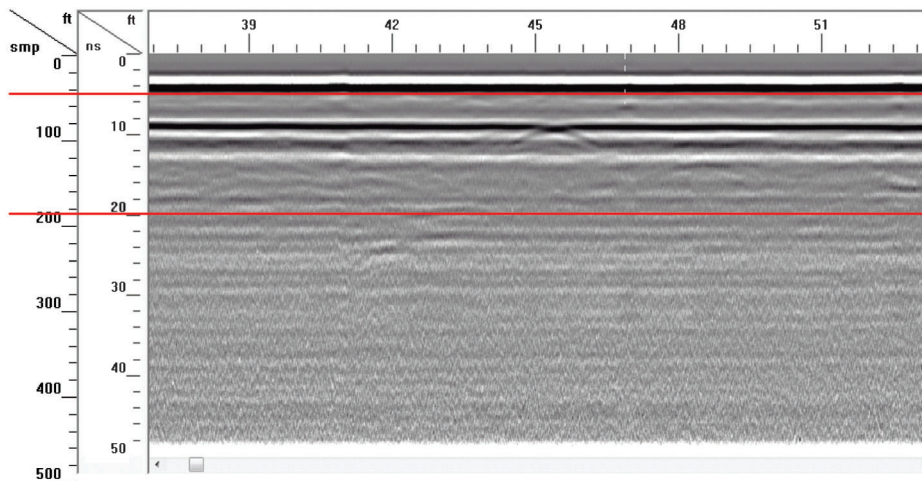

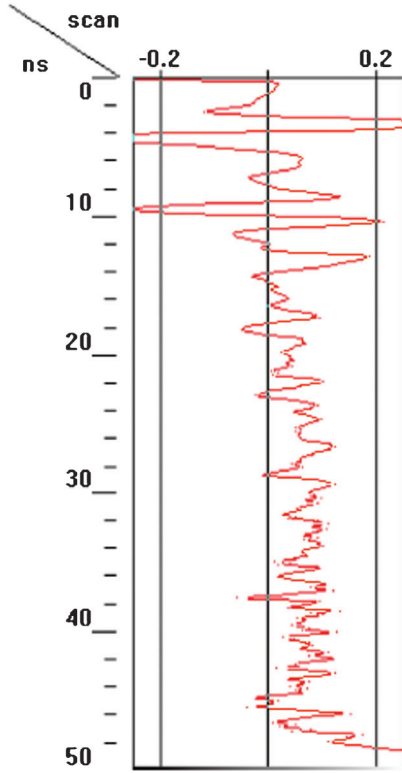**Figure 6.1** A 900 MHz GPR image indicating presence of an 8″ pipe.

Figure 6.2 An A-Scan signal from GPR data.

and the same calculation will apply again. The background window and target signal will keep on moving until the entire data set has been analyzed. Then, a different set of w and d will be tested by the same procedure above in another calculated loop. Finally, an optimal combination of *w* and *d* can be recommended for use in practice.

6.4.2 Detailed Calculation Steps of Proposed Algorithm 1

The main purpose of this algorithm is to find an optimal combination of w and d, which could be applied in practice. Although the whole algorithm contains several loops to perform this calculation, only one entire loop needs to be considered step by step to understand the whole algorithm.

Step 1: Obtain the average of background signals, b_m, within the considered background window.

$$\vec{b}_m = \begin{bmatrix} \frac{1}{w}\sum_{i=1}^{w} b_{1i} \\ \frac{1}{w}\sum_{i=1}^{w} b_{2i} \\ \vdots \\ \frac{1}{w}\sum_{i=1}^{w} b_{ni} \end{bmatrix} \quad (1)$$

The result of the operation above provides a generalized background signature representative of an area that does not contain a pipe. Given that the distance between buried pipes in practice typically greatly exceeds the width, w, of the background window ($\sim$4–5″), there is generally no danger of incorporating a pipe signature in the background that is ultimately subtracted from a target trace.

Step 2: Obtain the pipe area signal. The signal at the checkpoint mentioned above is located d columns away from the last trace (column) of selected background window and will move together with background window column by column over the entire data set. To illustrate the concept of the proposed algorithm, here a checkpoint signal located in the pipe detection area is selected.

Step 3: Subtract the background average from both the background signal and the checkpoint signal.

$$B' = \underbrace{\left[\vec{b}_1 - \vec{b}_m \cdots\cdots \vec{b}_w - \vec{b}_m \right]}_{\text{background signals - averaged background signal}} \quad (2)$$

$$\vec{s}' = \underbrace{\left(\vec{s}_1 - \vec{b}_m \right)}_{\text{check point signal - averaged background signal}} \quad (3)$$

After calculation of the background average, subtract this value from each background signal in the current calculated background window and also from the pipe area signal.

Step 4: Take the absolute value of the result in Step 3. In order to make future calculations easier, absolute values of results in Step 3 are considered, and the mean value and standard deviation of the absolute new background are also calculated for each row.

The absolute value of pipe area signal with background removed is given by:

$$\vec{s}''_m = \left| \vec{s}' \right| \quad (4)$$

The averaged absolute value of new background signals with background removed is thus given by:

$$\vec{b}''_m = \frac{1}{w}\sum_{i=1}^{w} \left[\left| \vec{b}_1 - \vec{b}_m \right| \cdots\cdots \left| \vec{b}_w - \vec{b}_m \right| \right] \quad (5)$$

Step 5: Calculate signal to noise ratio (SNR) at every checkpoint. The Signal to Noise Ratio (SNR) value is a measure of electrical signals that compares the checkpoint signal level to the background noise. A position with a higher SNR value is considered as a possible detected target in the algorithm.

Based on the definition of SNR, the mean SNR value at a certain location, each checkpoint column, can be determined as follows:

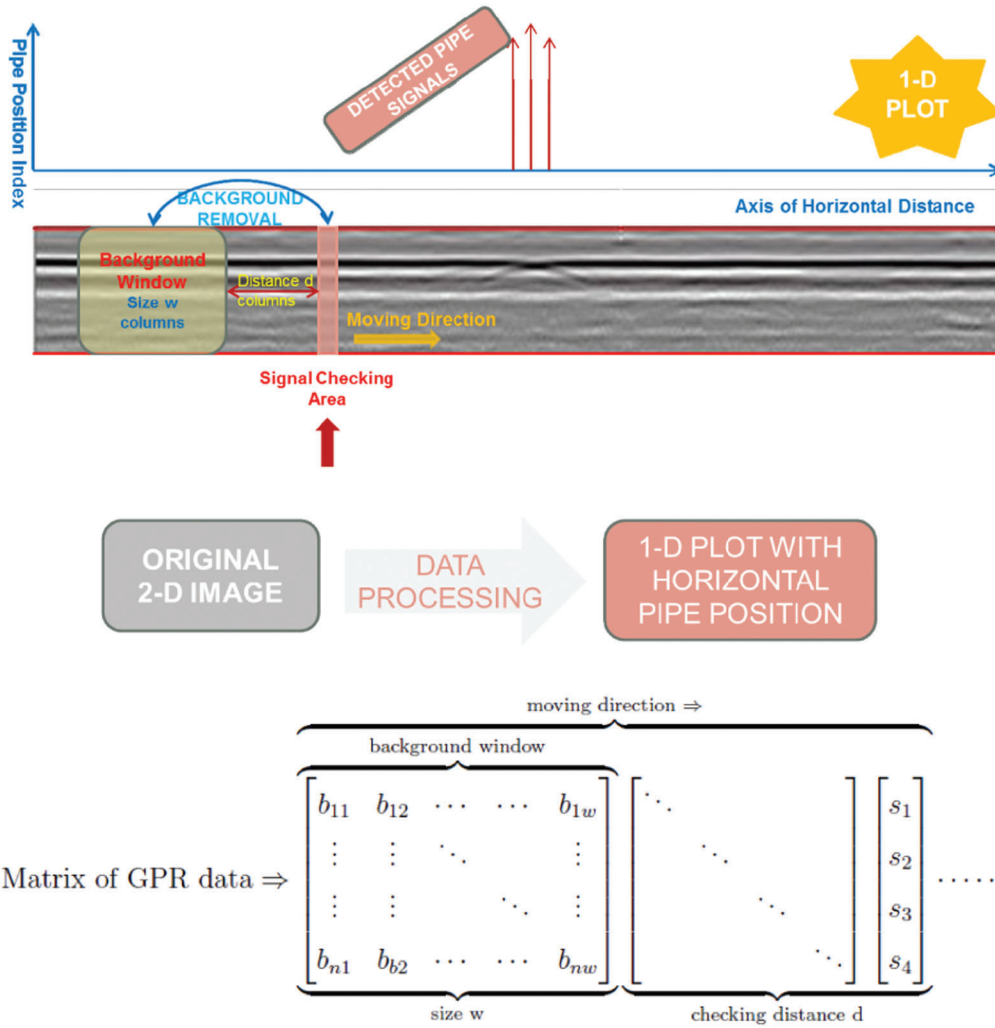$$SNR = \frac{mean\ (s''^2_m(i))}{mean\ (b''^2_m(i))} \quad (6)$$

Figure 6.3   Conceptual representation of algorithm 1.

$$SNR_{dB} = 10\log_{10}\left[\frac{mean\ \left(s_m''^2(i)\right)}{mean\ \left(b_m''^2(i)\right)}\right]dB \qquad (7)$$

In related MATLAB programs, SNR_{dB} is used for all SNR calculations. At this point, an original 2-D radar image is converted to a 1-D plot, SNR_{dB} versus horizontal positions of survey line.

Step 6: Threshold selection based on probability distribution of data obtained in Step 5. Based on the SNR_{dB} values obtained as a function of horizontal position, a histogram can be generated. Curve fitting of different probability distribution functions has been performed in order to determine the most appropriate distribution function to represent the histogram data. In the current algorithm, a normal distribution function has been selected to fit the histogram of SNR_{dB} values.

Several probability thresholds can then be selected to establish the confidence level of detecting a target. According to the distribution function fitted in the histogram, the related thresholds of SNR_{dB} values can then be back calculated and applied to the previous results.

As this algorithm represents only one part of a multi-stage process, a unique threshold cannot be determined here. Instead, a group of thresholds are tested. Further comparisons with results of other algorithms must be applied to finalize an optimal threshold value for calculation use as discussed below.

6.5 Algorithm 2: Anomalous Signal Removal

6.5.1 Overview of the Algorithm

GPR images are often plagued by anomalous discontinuous scan lines, especially in the data gathered with a 900 MHz antenna. As shown in Figure 6.4, several vertical lines go through the entire data set. Such anomalous lines could provide false high peaks in the SNR_{dB} plots mentioned above, which might generate an inaccurate detection result for the entire survey line. In order to avoid the influence of these anomalous lines in the data processing procedures, a new algorithm based on percentage change in signal elements was developed.
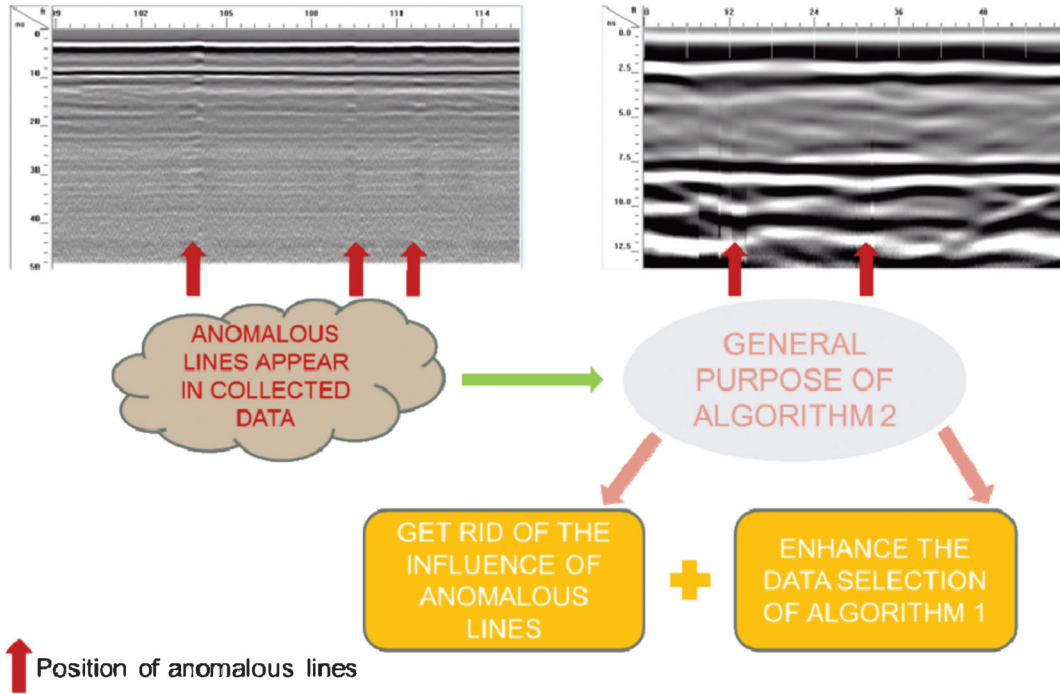
Figure 6.4 Anomalous lines in the GPR data set.

Because the anomalous lines always cross through the entire vertical range of GPR images, changes in the GPR signal along any horizontal data row crossing the lines should show a significant change in value at all vertical positions. Based on this assumption, the percentage change in the signal amplitude of every element relative to the previous element in every row of GPR data is calculated. This calculation is repeated row by row until the entire dataset is processed. However, even if there is a value jump across the anomalous lines; it is still not necessarily large enough to be noticed. Thus, the sum and standard deviation of the percentage changes for each row in a data column are calculated. A data column with a high sum and a low standard deviation is then identified as an anomalous trace. Finally, the original 2-GPR image is converted into a 1-D plot of this percentage change versus horizontal position, which allows the output from this algorithm to be combined with the output of algorithm 1. A conceptual illustration of algorithm 2 is shown in Figure 6.5.

6.5.2 Detailed Calculation Steps of Algorithm 2

The main purpose of this algorithm is to eliminate the influence of anomalous lines in GPR images. To implement this algorithm, procedures introduced below need to be followed.

Step 1: Calculate the percentage change of one element relative to its previous element in each row. As introduced previously, the original GPR image can be considered as a 2-D matrix data set. In order to implement algorithm 2, the percentage change of every element relative to its horizontal (row direction)

previous element must be calculated. As shown below, the original GPR data is converted into a new matrix data set based on equation (8). Each element of this new matrix is the calculated percentage change value.

Original GPR Data Matrix $\Rightarrow$

$$
\begin{bmatrix}
d_{11} & d_{12} & \cdots & d_{1,j-1} & d_{1,j} & \cdots & d_{1,n-1} & d_{1,n} \\
\vdots & \vdots & \vdots & \vdots & \vdots & \vdots & \vdots & \vdots \\
d_{i,1} & d_{i,2} & \cdots & d_{i,j-1} & d_{i,j} & \cdots & d_{i,n-1} & d_{i,n} \\
\vdots & \vdots & \vdots & \vdots & \vdots & \vdots & \vdots & \vdots \\
d_{m,1} & d_{m,2} & \cdots & d_{m,j-1} & d_{m,j} & \cdots & d_{m,n-1} & d_{m,n}
\end{bmatrix}
$$

$$
\begin{aligned}
p_{i,1} &= 0; \\
p_{i,j} &= \frac{d_{i,j} - d_{i,j-1}}{d_{i,j-1}} \times 100\%;
\end{aligned}
\qquad (8)
$$

Converted Matrix of Percentage Values $\Rightarrow$

$$
\begin{bmatrix}
0 & p_{12} & \cdots & p_{1,j-1} & p_{1,j} & \cdots & p_{1,n-1} & p_{1,n} \\
\vdots & \vdots & \vdots & \vdots & \vdots & \vdots & \vdots & \vdots \\
0 & p_{i,2} & \cdots & p_{i,j-1} & p_{i,j} & \cdots & p_{i,n-1} & p_{i,n} \\
\vdots & \vdots & \vdots & \vdots & \vdots & \vdots & \vdots & \vdots \\
0 & p_{m,2} & \cdots & p_{m,j-1} & p_{m,j} & \cdots & p_{m,n-1} & p_{m,n}
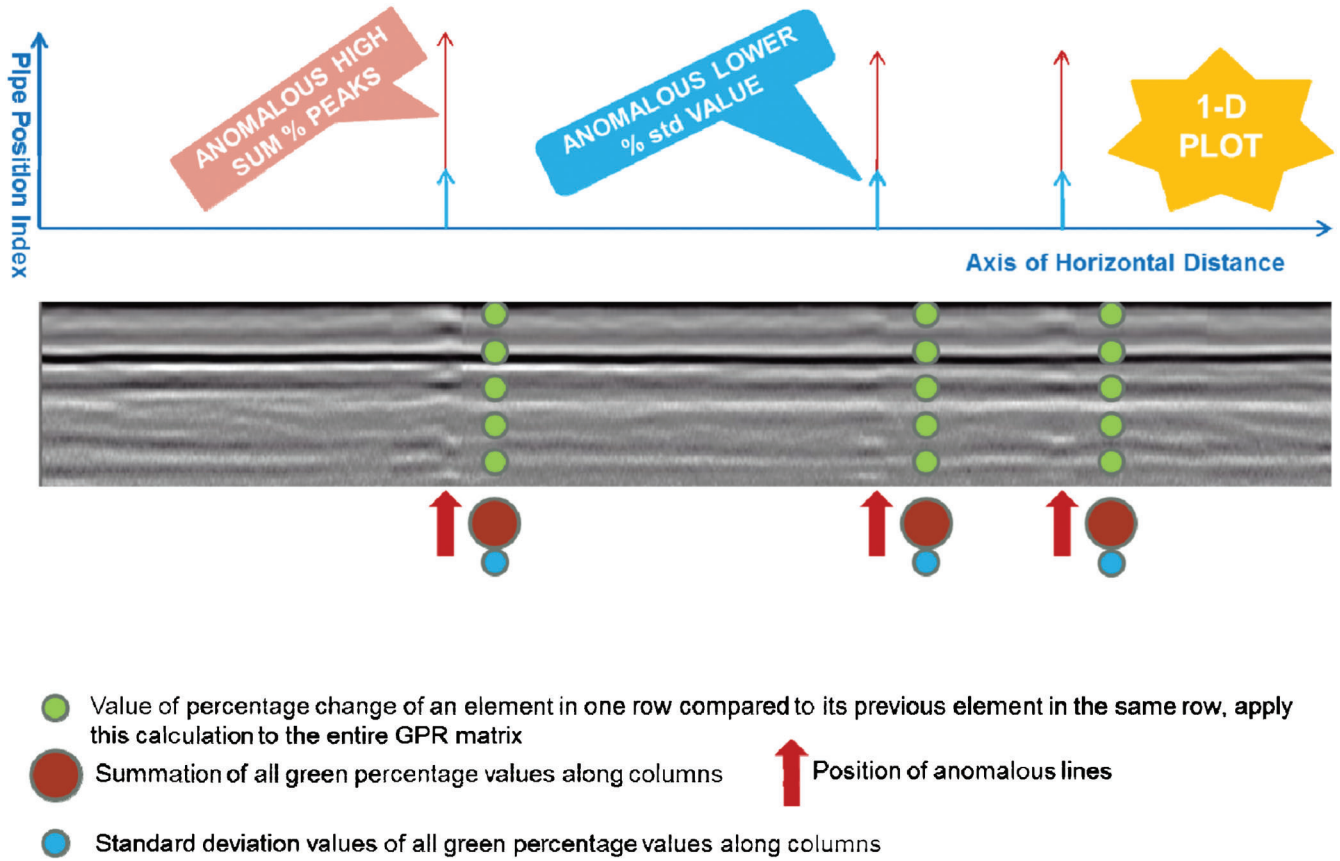\end{bmatrix}
$$

Figure 6.5 Conceptual representation of algorithm 2.

Step 2: Calculate the summation of every column of the new percentage change matrix. Although it is assumed that there will be a value jump in the original GPR 2-D image when crossing the anomalous lines, the percentage value obtained in the last step is still not necessarily easy to identify. Thus, a summation of each column of the new converted percentage data matrix is calculated. At this point, the original 2-D GPR data is also converted into a 1-D plot comparable to that developed with the first algorithm.

$$sp_j = \sum_{i=1}^{m} p_{i,j} \qquad (9)$$

Step 3: Calculate the standard deviation of each column of data obtained in Step 1. Based on 2-D GPR images, it is clear that a jump in signal values in a vertical row of the data matrix could result not only from anomalous lines, but also from target detection. The anomalous lines, however, normally cross through the entire vertical data set. As a result, the value jumps caused by anomalous lines always occur in all the rows at that position. Instead, the value jumps caused by possible target detection only happen in a certain vertical range. So the standard deviation of each column of the percentage change data matrix can be

determined as another useful criterion to eliminate the unwanted anomalous lines. Based on this assumption, both anomalous lines and target detection could cause a notable spike in the percentage change summation. However, the standard deviation of the columns where anomalous lines are present should be small compared with the locations of a target.

To this end, standard deviation values of each column of the matrix in Step 1 are also plotted in the form of a 1-D figure.

$$stdp_j = \text{std}\left[p_{i,j}\right]_{i=1}^{m} \qquad (10)$$

Step 4: Apply thresholds to plots obtained in Step 2 and 3 based on their probability distribution functions. This step is similar to Step 6 introduced in the first algorithm. The histograms of both results obtained in the previous two steps are generated. Then the resulting histograms are fit with a probability distribution function. Instead of selecting a normal distribution as with the first algorithm, a gamma distribution function is selected by this procedure as it appears to more consistently represent obtained field data.

Again, several probability thresholds are chosen based on the confidence sought in determining the targets along the survey line. According to the

distribution function fitted in the histogram, the related thresholds of percentage values can be back calculated and applied to the previous results.

Just as for algorithm 1, a unique threshold cannot be selected at this point. An optimal threshold will be determined in additional comparison steps.

Step 5: Combine two percentage outputs into one plot corresponding to selected thresholds. After a group of thresholds is applied in the last step, a comparison of the percentage summation plot with the percentage standard deviation plot at each selected threshold is performed. Peaks, which represent an index of potential pipe presence at a given location, present in both plots are left in the final result of the current algorithm. Peaks that only appear in one plot are ignored.

6.6 Combined Selection Mechanisms

Two algorithms were introduced herein. A combined output of these two algorithms is generated in the following sections. The two algorithms are first employed, independently, on a single frequency data set. The results of the two algorithms can then be combined. After this step, an additional filter can be applied to the results based on the logical spacing of installed drainage pipes in the field. Finally, tests performed at different GPR operational frequencies can be aligned and compared as one more mechanism to increase the reliability of target identification.

6.6.1 Combination of Two Proposed Algorithms

The two main data processing algorithms outlined above employ a group of signal evaluation thresholds to identify potential pipe locations and eliminate signal anomalies. The results of the two algorithms must then be combined. Peaks presented in the output of both algorithms are chosen to be shown in the combined result. Peaks only shown in one algorithm's result are ignored.

6.6.2 Output Selection for Field Data of Installed Pipe Distance

When processing actual field data, there is another criterion that can be used to further increase the selectivity of the pipe detection algorithm—installed pipe distance. This criterion can be used to determine whether a peak in the output result is a possible pipe or a false alarm. Because this project is based on a designed and constructed pavement, the distance between two outlet pipes should be relatively well defined. Even if the actual installed distance has some errors during construction, it still should fall in a reasonable range rather than be randomly distributed. Due to this property of drainage pipes in the pavement, a final screening of the output result from the two previous algorithms can be performed to improve overall detection accuracy.

In the field data collected on US-231, the distance between two installed outlet pipes is around 400 ft. Considering that some installation error was possible during construction, an evaluation interval of 400 ± 30 ft is applied during this selection procedure.

Considering an output result at a certain threshold level obtained in the previous section, the final detection procedure is carried out as follows: (1) this pipe distance check examines the first peak point along the horizontal survey line and assumes that it is an identification point in this procedure; (2) then the algorithm establishes a second checkpoint located 400 ft away from the first point; (3) then a search is performed point by point within a range of ± 30 ft centered at the checkpoint; (4) if there is at least one peak point present in this search range, the identification point together with all the points in the searching range is considered to be a possible pipe detection signal; (5) otherwise, if there is no peak point in this searching range, the identification point is considered as a false alarm point and will be ignored in the final output; (6) the same procedure is repeated for all the points in the data set until the entire data line has been scanned; (7) at last, a final output with possible pipe locations is provided. This overall procedure is repeated assuming a new starting point at each peak within the initial increment of the inter-pipe distance in the data set to develop a full set of possible pipe locations.

Applying this searching procedure to the results of all the threshold levels, a group of final results for a single frequency GPR image is produced. At this point, the data from each GPR frequency can be aligned for comparison, which will be introduced in the next section.

6.6.3 Comparison of Multi-Frequency Results

GPR data collected with different frequency antennae could provide complementary information. One advantage of the SIR-30GPR system is the ability to perform a test with four active channels at the same time, which makes simultaneous detection of data from different frequency antennae possible. To compare the results obtained with different frequency antennae, the most important step is to align both results at the same horizontal starting point to make sure the detected pipe signals appear at the correct horizontal locations. Then the plots of the final results obtained at different frequencies can be depicted in the same figure. The peaks shown in both frequency results could be considered as more likely locations of target pipes.

6.7 Field and Lab Data Verification

To demonstrate the methodology introduced above, both field and laboratory results are analyzed in the following sections. Table 6.1 provides a summary of the field tests.

A field test was performed on a section of US-231 near the intersection of US-231 and INDIANA-25

TABLE 6.1
Summary of GPR Field Test Information

Field Test Location	US-231/River Rd Near Purdue Bowen Lab	I-65N (Mile 142– 148), Lebanon IN	New US-231 near Purdue Airport
Test Dates	08/16/2010	05/14-05/16/2012	06/17-06/18/2013
Involved Drainage Type	PVC X-Drain	PVC X-Drain and Metal K-drain	PVC X-Drain
Test Length	~1500 ft	~6 miles	~1000 ft
No. of Antennas Used	2	4	6
Related Frequencies in the Test	400 MHz and 900 MHz	400 MHz (2) and 900 MHz (2)	270 MHz (2), 400 MHz (2) and 900 MHz (2)

involving 4 PVC outlet pipes. The average depth of the target pipes was about 2 feet, and the pipes had a diameter of 8 inches (Pipe No. 1) or 4 inches (Pipe No. 2-4). The GPR system used in this test was equipped with two antennae having frequencies of 400 MHz and 900 MHz. The total survey is around 1300 ft long, and the data was collected on the shoulder of constructed pavement.

A simulated pavement cross-section was also established in the laboratory. The laboratory test basin was employed to hold soil materials as well as other necessary components, such as installed PVC pipes. Concrete blocks were used to simulate the pavement surface. During the laboratory test, data was collected with both 400 MHz and 900 MHz antennae.

A discussion of the effectiveness of the background reduction and anomalous signal removal algorithms in each of these scenarios is provided below.

6.7.1 Field Data Analysis

In this section field test data is analyzed following the procedures introduced above and employing the two different proposed algorithms. Because the data processing procedures are the same for both 900 MHz and 400 MHz data prior to the final combination of different frequency outputs, only 900 MHz processed results are described in detail in the sections below. At the end of the discussion, final combination of two frequency results is performed in order to make the final detection decision for this field survey test. As shown in the following two groups of figures (Figures 6.6 and 6.7), only pipe No.1 can be readily seen via visual inspection in the original 900 MHz GPR image. The other 3 smaller pipes cannot be visualized in the 900 MHz data or the 400 MHz data.
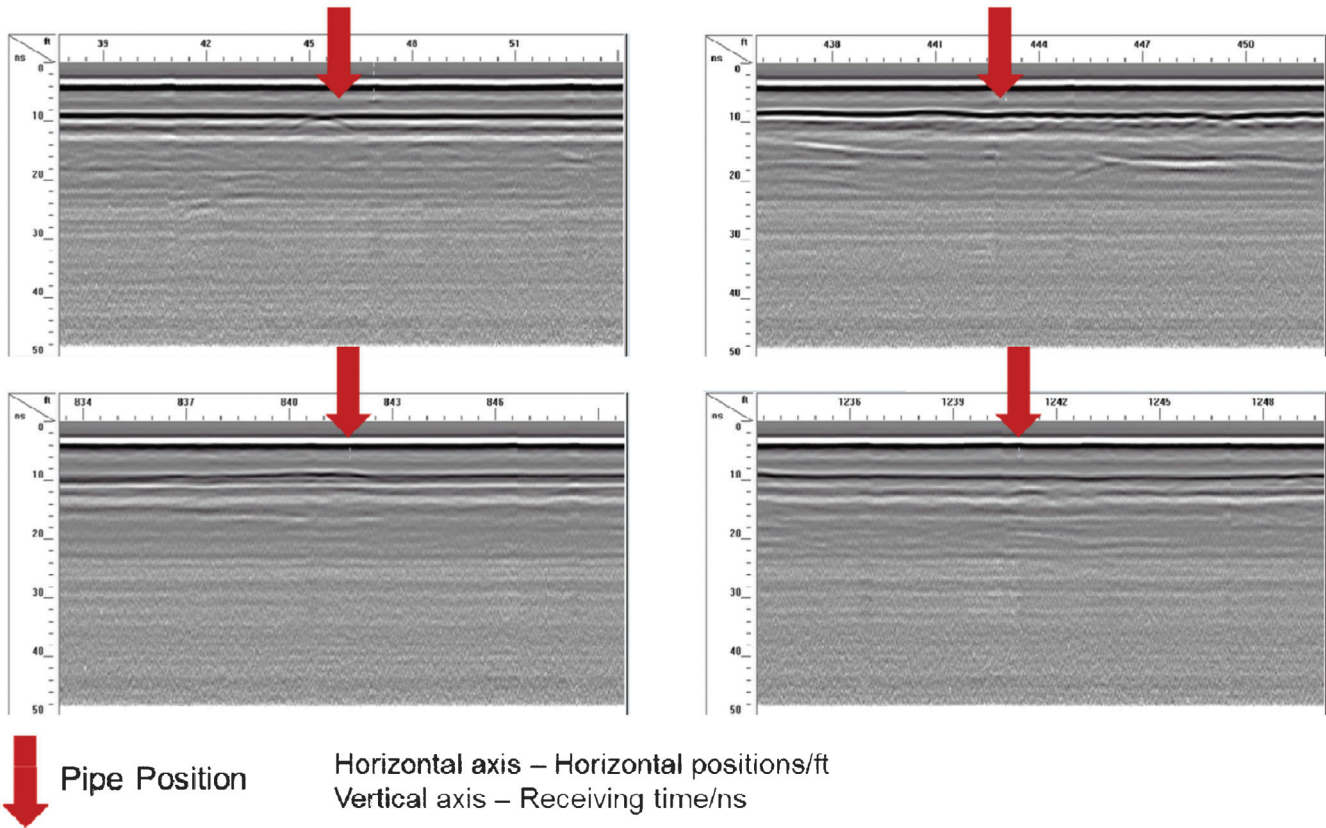

Pipe Position

Horizontal axis – Horizontal positions/ft
Vertical axis – Receiving time/ns

Figure 6.6 Original GPR data set of 900 MHz frequency.

Pipe Position

Horizontal axis – Horizontal positions/ft
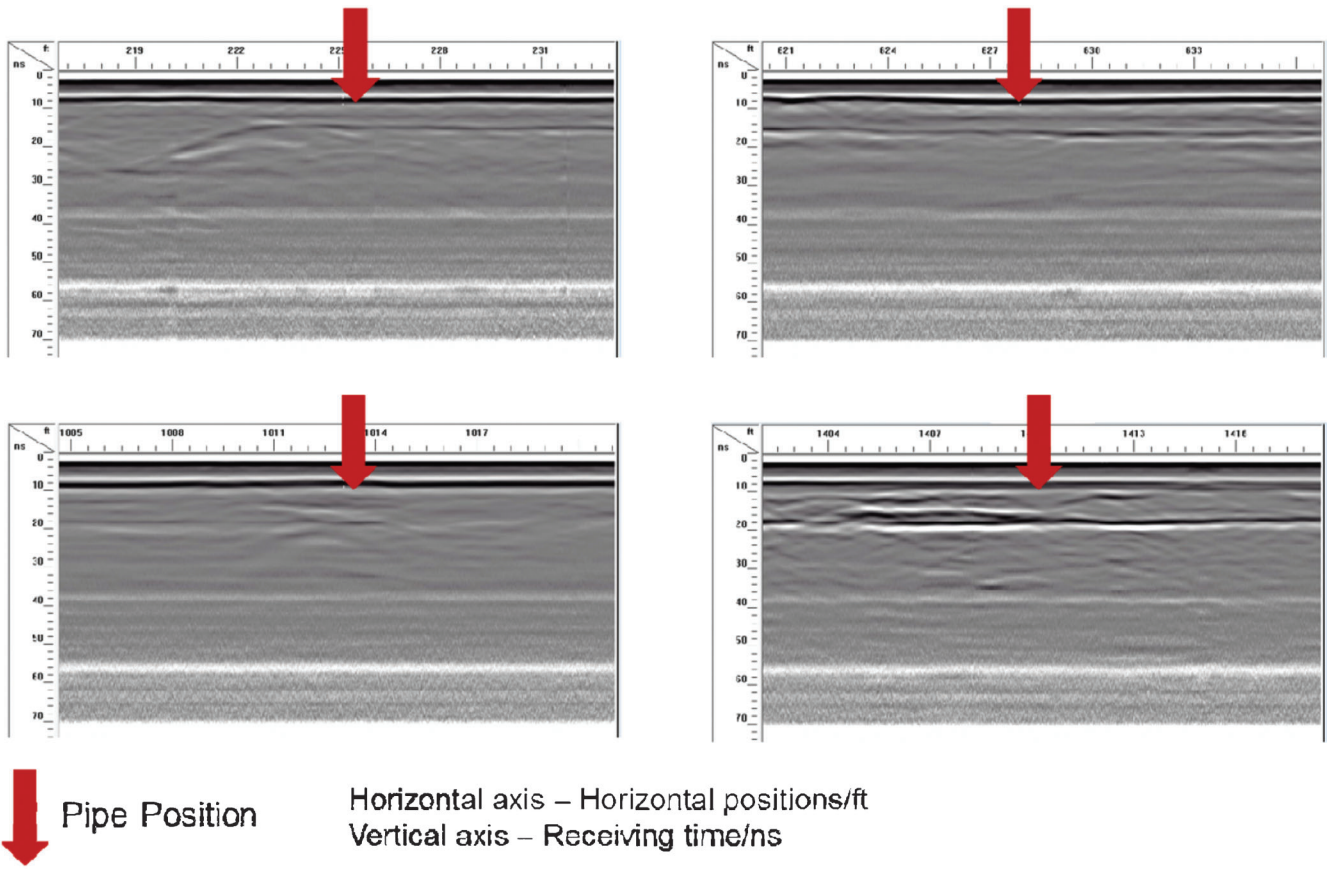Vertical axis – Receiving time/ns

Figure 6.7   Original GPR data set of 400 MHz frequency.

1. 900 MHz Results of algorithm 1: moving average background reduction. As noted earlier, two key outputs are developed through algorithm 1:

a. **SNR_{dB} Values Plot:** The result provided with this algorithm is a 1-D SNR_{dB} plot versus horizontal survey positions, which is shown on the right side of Figure 6.8.
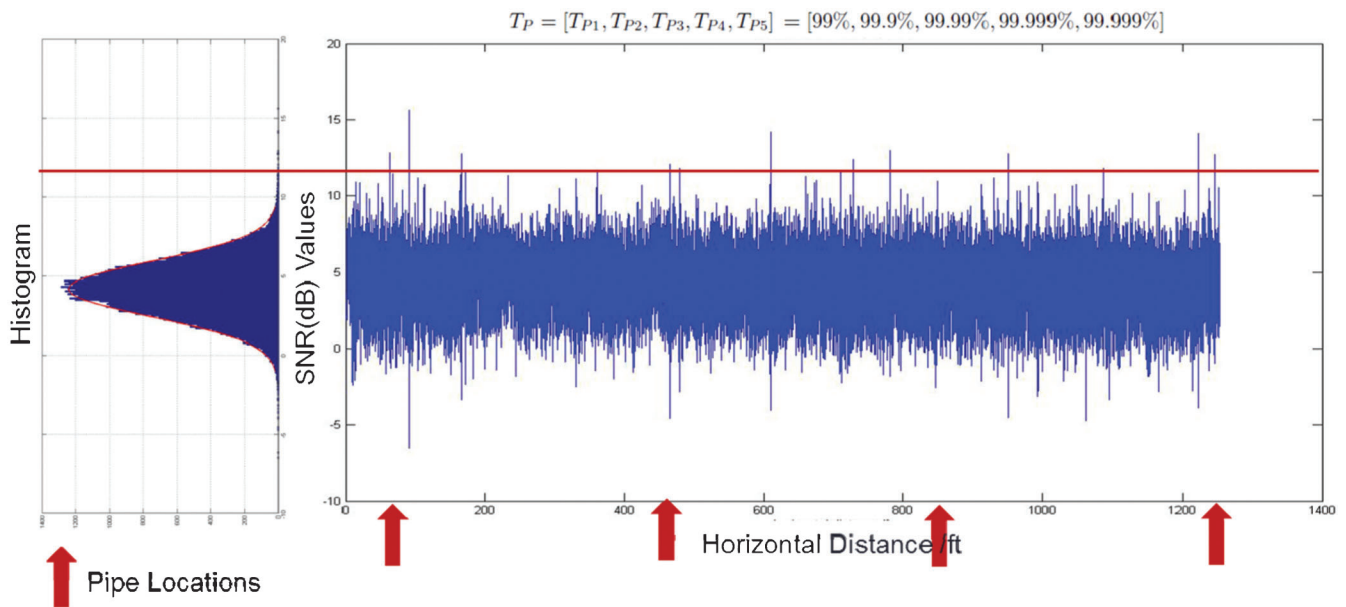

$$T_P = [T_{P1}, T_{P2}, T_{P3}, T_{P4}, T_{P5}] = [99\%, 99.9\%, 99.99\%, 99.999\%, 99.999\%]$$

Figure 6.8   900 MHz result of algorithm 1.

b. **Histogram with Distribution Fit of SNR$_{dB}$ Results:** Based on the obtained SNR$_{dB}$ results, a histogram is generated for future threshold selection, as shown on the left side of Figure 6.8. The histogram is also fit with a probability distribution function which in this case is best defined by a normal distribution function.

2. 900 MHz Results of algorithm 2: anomalous signal removal. Two major outputs are also generated from algorithm 2:

a. **Percentage summation plot:** Here the percentage change in the signal amplitude of every element in an A-scan relative to the previous A-scan in the series is calculated, summed, and plotted vs. horizontal location as shown in Figure 6.9.
b. **Percentage standard deviation plot:** The standard deviation of percentage changes in each A-scan are then plotted vs. horizontal location as shown in Figure 6.10.

Histograms of both the percentage summation and standard deviation plots are subsequently generated, together with suitable distribution functions. Instead of selecting a normal distribution as with algorithm 1, a gamma distribution is more appropriate here.

3. Threshold selection for both algorithms. As described earlier, selection of thresholds for both algorithms is based on their probability distribution functions. A group of probability thresholds is used across the entire analysis procedure. Real number thresholds for a single case could be back calculated by their corresponding probability distributions. Due to the fact that the number and dimension of pipes in the entire survey line is extremely small compared to the total survey length; a group of high probability thresholds is selected in this analysis procedure. Trial analysis would typically be performed for all the

thresholds to identify an optimal threshold value. The trial group of probability thresholds is listed below.

$$T_P = [T_{P1}, T_{P2}, T_{P3}, T_{P4}, T_{P5}] =$$

$$[99\%, 99.9\%, 99.99\%, 99.999\%, 99.999\%]$$

4. Combination of two algorithms with thresholds applied. In this step, each threshold in the list above is first applied to all the results obtained in Figures 6.8, 6.9 and 6.10 separately. Then the two percentage results are combined into one data set with peaks presented in both plots only. Finally, the pipe distance searching procedure is applied. The final results of the 900 MHz survey correlated to certain threshold level are then generated at this stage. Figures 6.11 through 6.13 show the results of 900 MHz data with probability thresholds T_{P1} to T_{P5}. The figure illustrates that the threshold levels of T_{P1} and T_{P2} are not very selective and thus lead to multiple false alarms along the detection line. On the other hand, the threshold levels of T_{P4} and T_{P5} provide results with over selections, which fail to detect most major targets. Thus, the threshold level of $T_{P3} = 99:99\%$ is considered as the optimal threshold level that should be applied in this analysis procedures.

5. Combination of results obtained by two frequencies. In order to obtain a more accurate detection result, results obtained at two different GPR frequencies are then compared. With the optimal threshold level of $T_{P3} = 99.99\%$, a final detection result is presented in the Figure 6.14. As shown in this figure, the 4 red peaks are the actual pipe locations along the road; blue peaks are the possible pipe detection locations obtained from the 900 MHz data; and green peaks are the possible pipe detection locations obtained from the 400 MHz data.
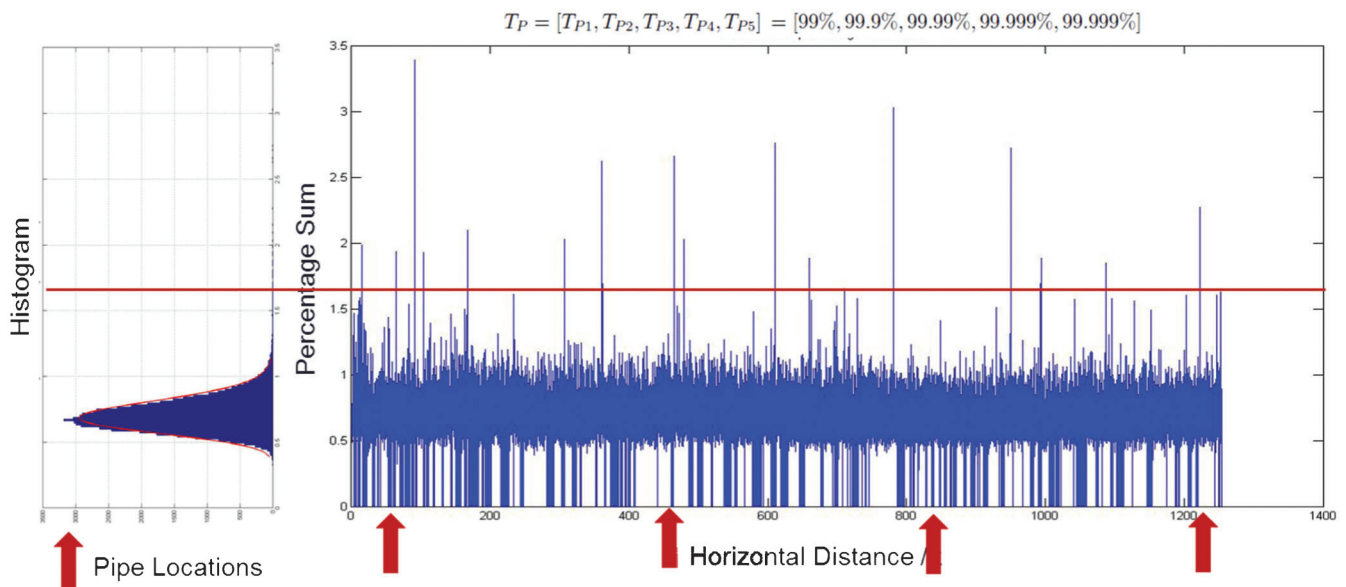

Figure 6.9 900 MHz result of algorithm 2—percentage summation.

$$T_P = [T_{P1}, T_{P2}, T_{P3}, T_{P4}, T_{P5}] = [99\%, 99.9\%, 99.99\%, 99.999\%, 99.999\%]$$
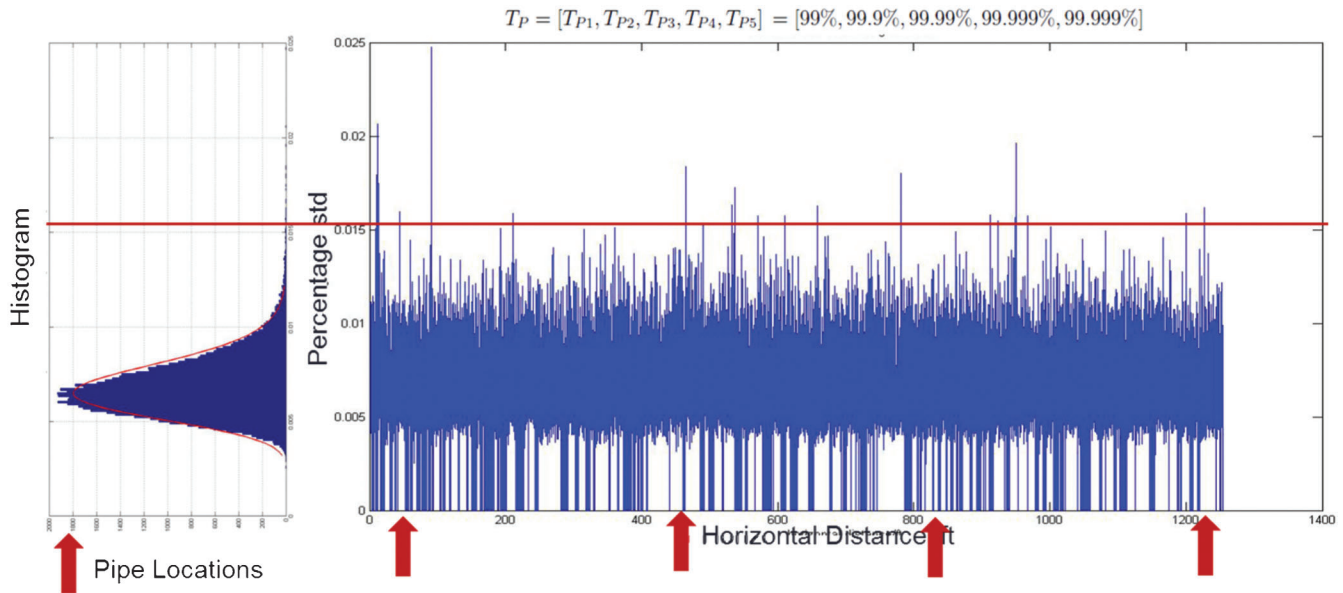

Figure 6.10 900 MHz result of algorithm 2—percentage standard deviation.

Ultimately, pipes 1, 2, and 4 were successfully detected by the proposed analysis procedures, and 5 false alarms are registered. Pipe 3, located at a horizontal distance of just over 1000 ft. in the scan, was not detected by either antenna. Nonetheless, the aforementioned signal processing algorithms significantly improve detection success over the original base case visual scan which had readily displayed only Pipe #1.

6.7.2 Target Detection Effectiveness

Detection effectiveness for the introduced algorithm relative to visual inspection of the original GPR images (i.e., "observation") for the US 231 data can be described in terms of detection successes, missed targets, inferred targets, and false alarms. Figure 6.15 illustrates that system effectiveness varies based on antenna operating frequency, and whether or not the developed algorithms are employed. Use of the developed algorithm on the combined frequency data improved

detection substantially over both visual observation and individual antenna analyses. Although false alarms still occur when using the algorithm, it is important to note that even when visually interpreting the original GPR images, there are significantly more false alarms. Figure 6.16 summarizes these findings, demonstrating that use of the developed algorithms increases detection success from 25% with visual observation using 900 MHz antenna, to 75% when the data analysis algorithms are employed on the combined 400 MHz and 900 MHz data. In addition, the error rate, that is the ration of false alarms relative to inferred targets, reduces from a high of 100% for the 400 MHz system to 70% for the combined data analyzed with the algorithms.

6.7.3 Lab Data Analysis

As noted earlier, the above signal processing algorithms were also applied to data obtained from a laboratory experiment performed in the wooden test
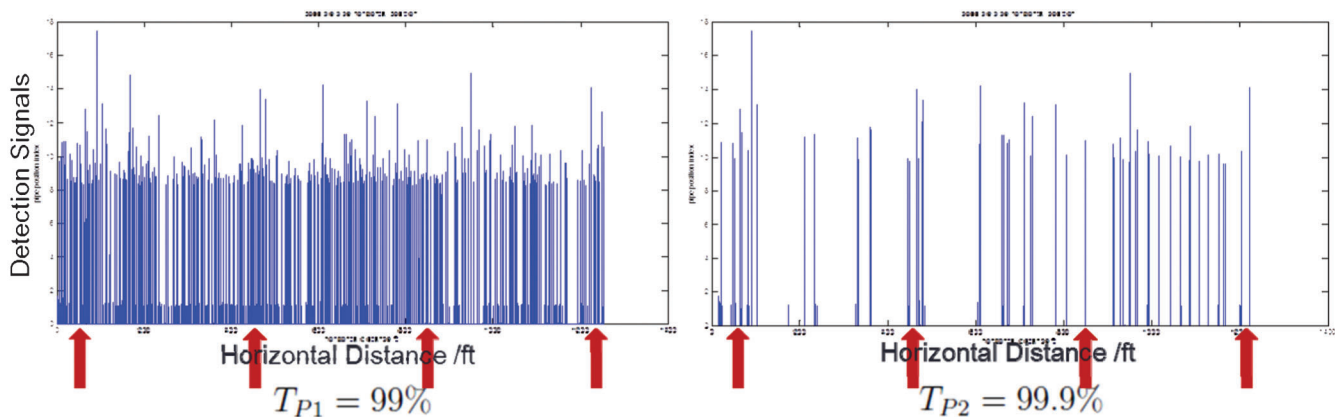

Figure 6.11 900 MHz Final result at threshold level of $T_{P1} = 99\%$ and $T_{P2} = 99.9\%$.
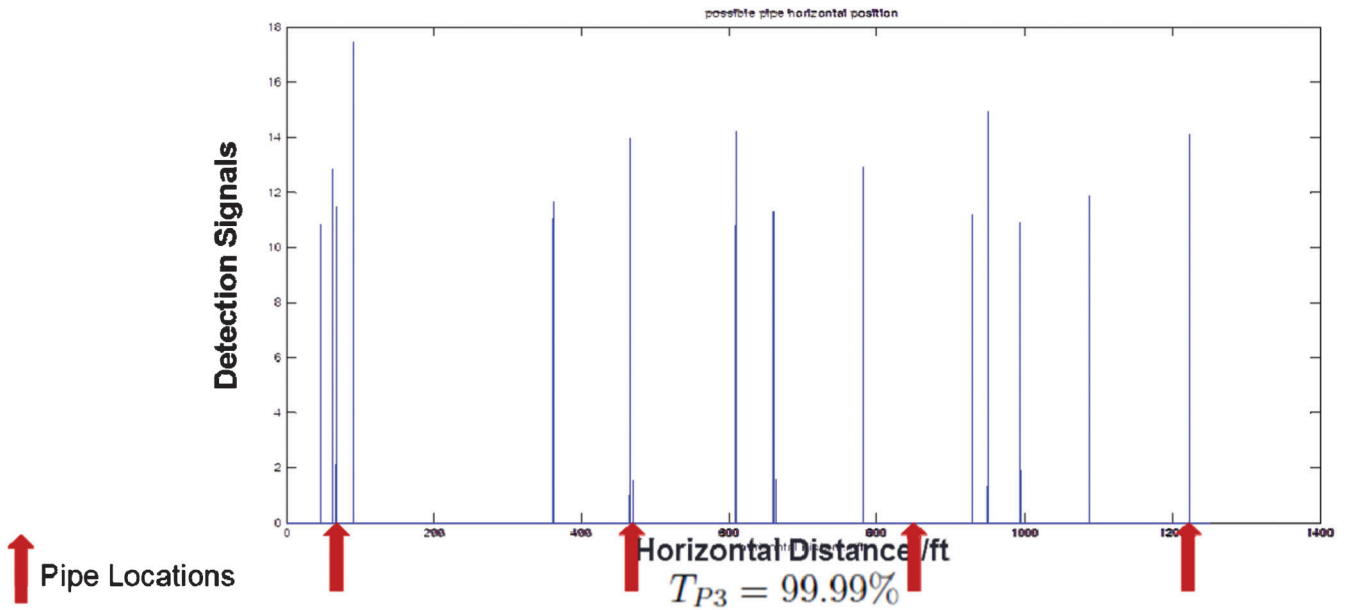
Figure 6.12   900 MHz Final result at threshold level of $T_{P3} = 99.99\%$.

basin. As illustrated in Figure 6.17, the test basin (measuring 57" (L) by 20" (D) by 20" (W)) was filled with local soil in the Purdue Geotechnical lab and outfitted with a 2" diameter PVC pipe installed on the bottom of the basin at the mid-point of the basin. This 2" PVC pipe is normally considered non-detectable for the ordinary GPR scan, as evidenced by both 900 MHz and 400 MHz data presented in Figure 6.18.

For this lab test, only the analysis procedures of algorithm 1, the moving background reduction, were applied. Due to the limited length of the test basin, it is not possible to obtain enough data to develop robust percentage change statistics via algorithm 2 to represent a correct probability distribution, thus this procedure is ignored in this particular analysis. However, results obtained at two different GPR operating frequencies are still combined here as a final step.

The analysis procedures are exactly the same as the ones used to process the field data described above. Thus, the results obtained in each calculation step are not shown for simplicity. Instead, only a final detection result is shown in Figure 6.19 with a threshold level of Tp = 99%.

The result is similar to that obtained with the field test data—red peaks represent the actual position of the installed pipe; blue peaks represent the final detection result from the 400 MHz data; and green peaks represent the final detection result from the 900 MHz data. According to this final result, the installed 2" PVC is successfully detected but with two false alarms. One possible reason for the false alarms is that anomalous lines could not be removed without algorithm 2. Another possibility is that there could be air voids in the test basin because of the lack of effective soil
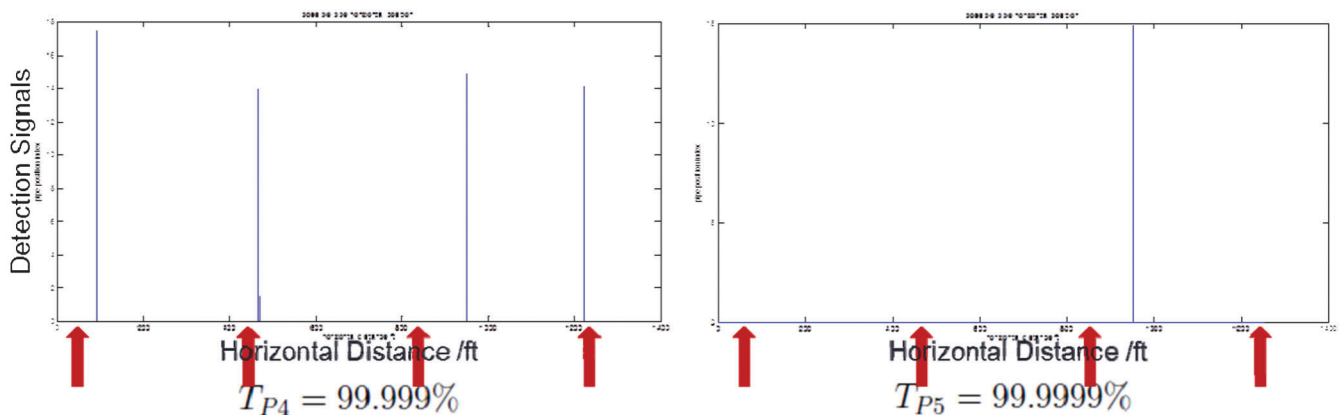

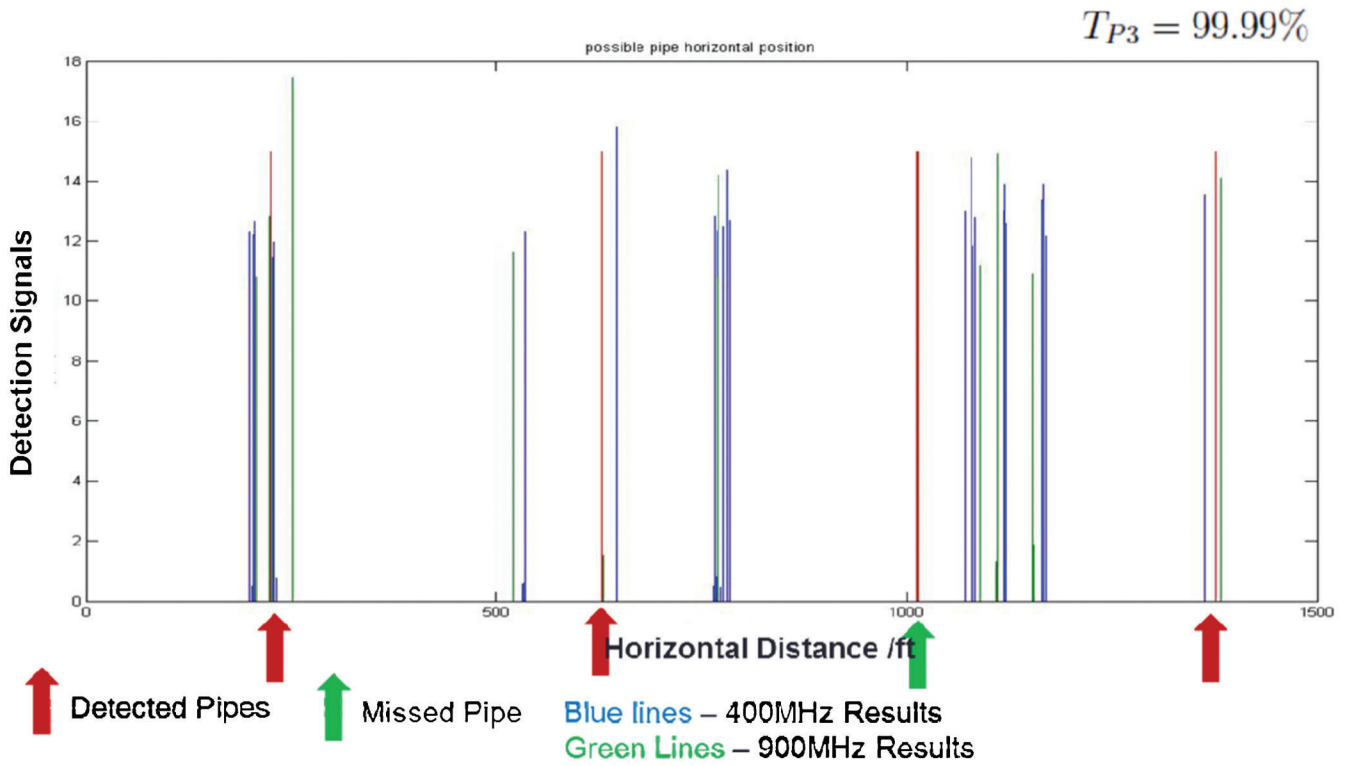**Figure 6.13**   900 MHz Final result at threshold level of $T_{P4} = 99.999\%$ and $T_{P5} = 99.9999\%$.

$$T_{P3} = 99.99\%$$

Figure 6.14   Final detection result of US-231 field test with a threshold level of $T_{P3} = 99.99\%$.
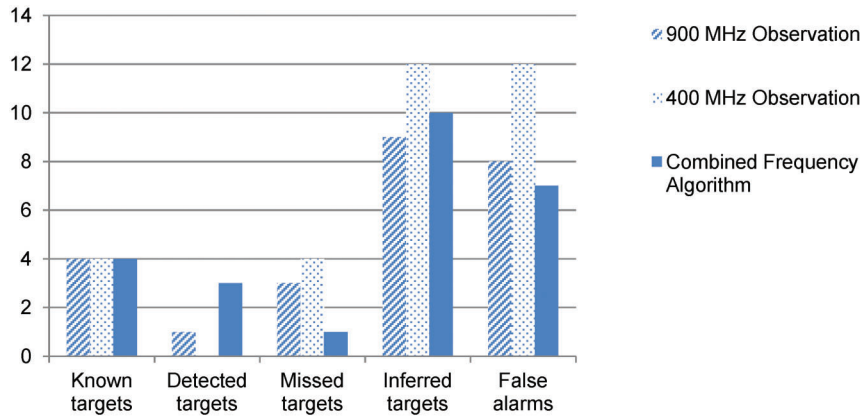

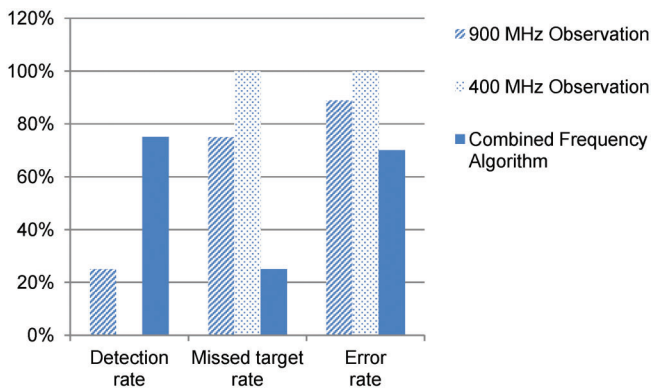**Figure 6.15**   US231Field data detection effectiveness.
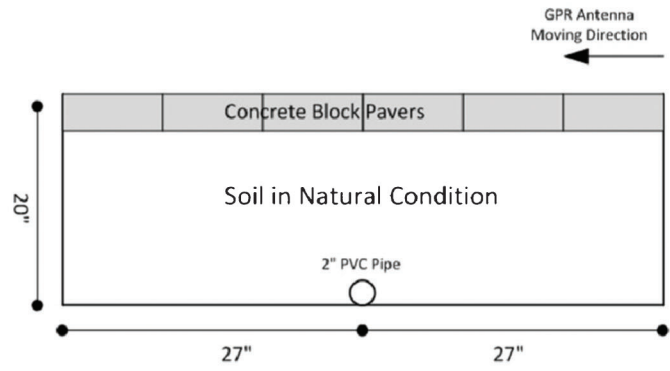

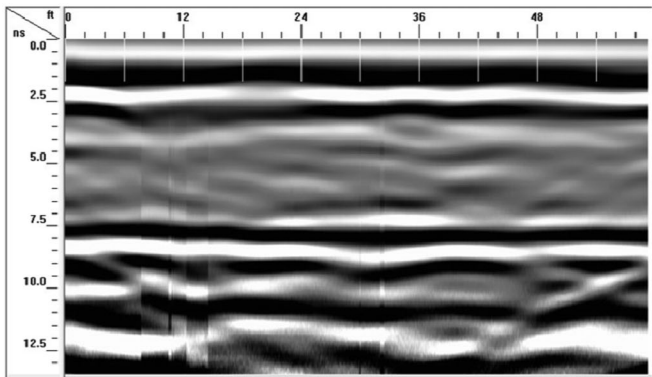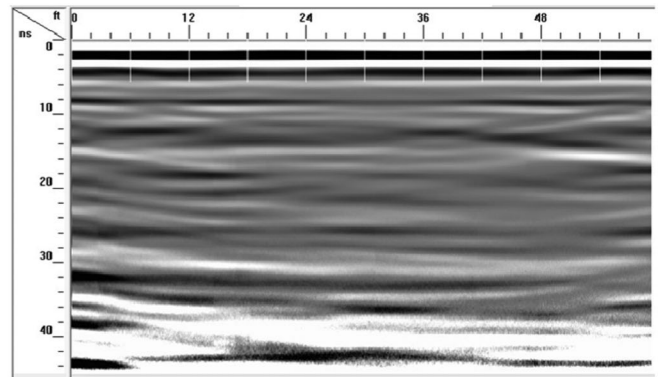**Figure 6.16**   US231Field data detection rate comparison.

Figure 6.17 Laboratory experiment set up and illustration.

900MHz Original Image

400MHz Original Image

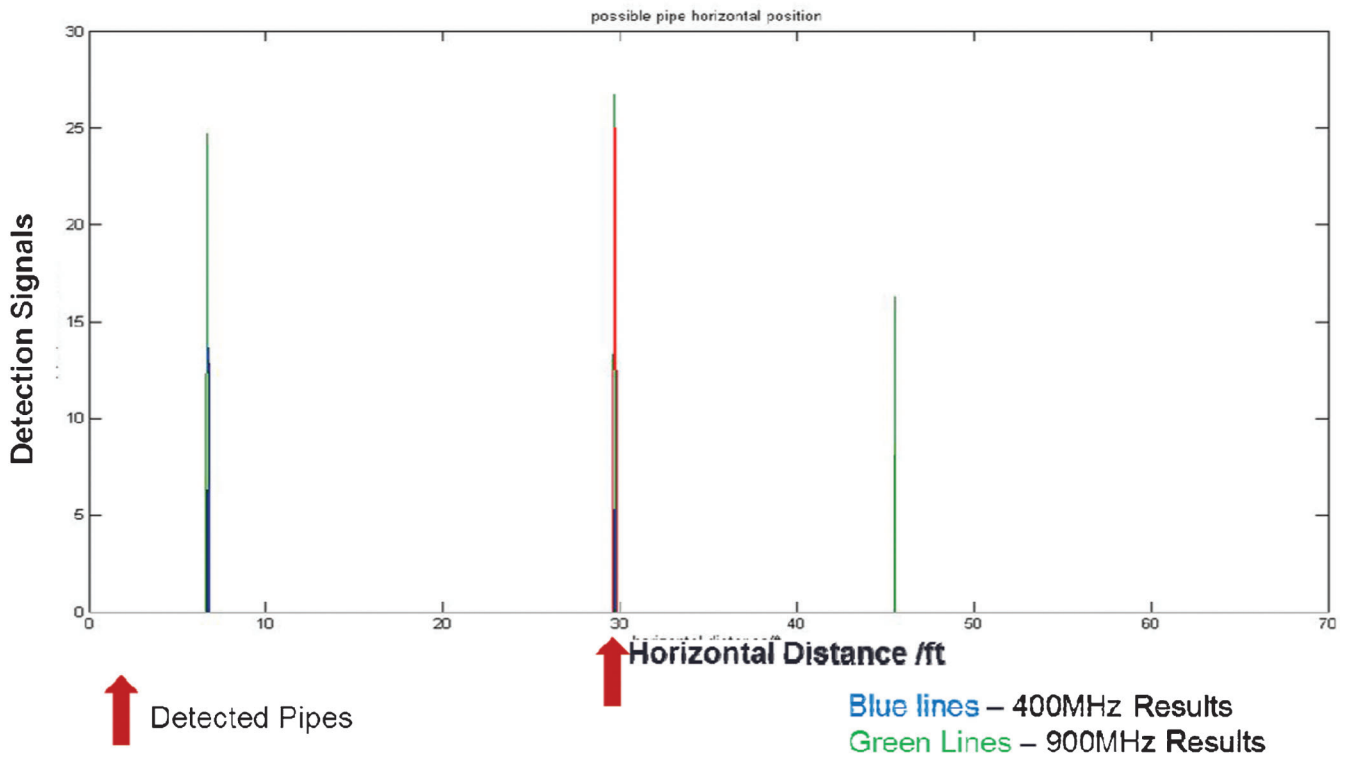**Figure 6.18** Original GPR image of laboratory experiment setup.

Figure 6.19 Final result of laboratory experiment.

compaction in the laboratory. Overall, the signal processing procedures pursued here appear to significantly enhance the ability to identify pipe locations beyond what could be achieved using standard visual inspection of the 2-D GPR data.

7. DIGITAL SIGNAL PROCESSING METHOD 2: PATTERN RECOGNITION

7.1 Introduction

Pattern recognition is another approach that can be employed to analyze data obtained via GPR scans. As is well known, the typical GPR signal returned by a buried drainage pipe takes the form of a hyperbola. With this in mind, the signal processing method pursued in this part of the work is focused on enhancing the collected hyperbola signals in order to identify potential targets.

In contrast to the improved background reduction method introduced in the previous sections, this analysis is still performed on the 2D data set rather than a 1D variant. The primary purpose of this method is to recognize the signature pattern—a hyperbolic shape—of potential drainage targets in order to facilitate detection. After processing data via Methods 1 (improved background reduction) and 2 (anomalous signal removal), several potential target areas are flagged. These areas can then be explored by employing a pattern recognition algorithm, hereafter referred to as Method 2 (pattern recognition), to search for hyperbolic shapes in the original GPR image. Verified by this pattern recognition technique, the results obtained by Method 1 could be more accurate and reliable.

To gain benefit from a pattern recognition method, unclear hyperbolic shapes in the original GPR image must be enhanced so that they can be recognized by an edge detection or shape recognition algorithm. Typically, there are three steps to this process: (1) the mean value of the entire potential checking area is removed in order to reduce unwanted background and noise; (2) the signal difference is improved by calculating the square of observed values; and (3) the original image is converted into a binary image by applying selected greyscale thresholds. The details of this technique will be introduced in the following sections.

7.2 Literature Review on Pattern Recognition in GPR Applications

Pattern recognition is a popular image processing approach to identify particular shapes in a given image. This method can be used to detect various curves and shapes appearing in an image, such as straight lines, circles, and triangles, or in the case of GPR, the hyperbolic return resulting from a buried pipe. Confirmation of a hyperbolic return signal is a high confidence indication of a successfully detected target.

Several researchers have done a lot of work in GPR image pattern analyses. Al-Nuaimy, et al. (67) introduced an automatic detection method for buried

objects using neural networks and pattern recognition; Delbo, et al. (68) introduced a fuzzy shell clustering approach to recognize the hyperbolic signatures in GPR images; Pasolli, et al. (69) introduced a pattern recognition approach to automatically analyze the GPR images. The core of these methods involves comparison of the hamming distance between candidate hyperbolic shapes and data points in an enhanced binary GPR image. Others have expanded on this basic approach. For example, Milisavljevi, et al (70) introduced a hyperbola detection technique using a randomized Hough transform applied to high potential region selections. Ehret (71) introduced an artificial neural networks (ANN)- and support vector machines (SVM) -based pattern recognition approach to analyze geophysical data.

In this work, emphasis is placed on preparing a data set for application of a pattern recognition algorithm. This involves two key stages of analysis: (1) select potential target areas using the method of improved background reduction discussed earlier; and (2) within the selected potential target areas, enable improved hyperbola recognition by improving the contrast and definition of the original image.

7.3 Data Analysis Procedures

As introduced above, the main method discussed herein is focused on enabling hyperbolic shape recognition in the original GPR images. Before applying the pattern enhancement method to the entire set of data, potential areas with targets are selected using the method of improved background reduction (Method 1). Because most of the data obtained from a roadway scan does not contain a drainage pipe, there is little value in searching the entire data set to identify hyperbolas. Method 1 will produce a plot indicating potential drainage pipe positions as a function of horizontal location in the data set. The detailed procedures of this method have been discussed in Section 6 of this report and will not be repeated here.

Based on every marked potential pipe location, a range of data to the left and to the right is selected as the analysis area for the pattern enhancement method (Method 2). This method involves the following steps.

Step 1: Pre-selection of vertical data. Just as outlined for Method 1, along the vertical depth of an A-scan, it is unlikely that data received at delay times greater than 30ns is of any value, as noise is typically stronger than the transmitted radar pulse in this range. Thus, to accelerate calculations, only the data received before 30ns is considered in the analysis (this cutoff can be modified as needed for specific field circumstances).

Step 2: Remove the average signal from the entire selected analysis area. In order to enhance the received hyperbola signals and also remove some of the unwanted background and noise, such as horizontal pavement layer reflections and random noise, a simple background

reduction technique is applied here. Normally, this procedure will not destroy the hyperbola signatures and may increase the contrast of the useful signals.

Step 3: Enhance the signal contrast by taking the square of the result obtained in Step 2. Normally, the hyperbolic shapes in the original data set are not clear enough to be identified easily. One possible reason could be the magnitude difference between the hyperbolic signal and background is too low. Thus the contrast in the image may not be large enough to facilitate separation and the result is an unclear hyperbolic shape. Squaring the signal values in the background reduced matrix improve the contrast significantly.

Step 4: Convert the image matrix obtained in step 3 to a binary image based on selected threshold. Even though step 3 could significantly increase the signal contrast in the GPR image, the signature shape of a hyperbola may not be easily identified. Thus, in order to perform automatic detection, the image obtained in step 3 is converted into a binary image based on user selected signal thresholds.

7.4 Field Data (I-65N) Analysis and Comparison

7.4.1 Introduction of field test on I-65N

A two-day field data collection effort was performed in May 2012 on the side of Interstate road I-65N. The purpose of this test was to locate both X-Drains and K-drains on the side of the interstate. X-drains are newly installed PVC pipes under the pavement layer, while K-drains are old existing metal pipes located more deeply under the pavement. Figure 7.1 provides a picture of the equipment setup before the test. As seen in this picture, there are 4 antennae involved in this test, two 400 MHz antennae and two 900 MHz antennae with different polarization directions.

Figure 7.1 GPR Equipment set up on the side of I-65N.

The data collected in this test represents a survey that is about 5 miles long, thus only a portion of the data analysis is presented here, that is the first 1000 ft starting from I-65N mile marker 146. Physical observations confirm that there is at least one X-drain present at the horizontal location of 558 ft and a K-drain present at the horizontal location of 910 ft.

7.4.2 Data Analysis

In order to assess the effectiveness of the previously described pattern enhancement technique, only 400 MHz data is analyzed here.

Results obtained by Method 1. As introduced in the previous sections, Method 1 was fist carried out on the data to obtain potential pipe location areas. The detailed analysis procedure was introduced in previous sections of this report and will not be repeated here. The results from Method 1 are summarized in in Figure 7.2 and Figure 7.3.

Based on the obtained results, the total number of potential targets could be 9 when applying an SNR threshold of 95%. When the threshold is set higher, the number of potential targets decreases because of the strict selection factors. Within the 9 potential targets, number 5 is the known X-drain located at about 558 ft, and number 9 is the known K-drain located at about 910 ft. The other 7 potential targets still could not be definitively declared detects or false alarms at this point in the analysis.

Hyperbola signature recognition in the potential regions. After obtaining the potential target regions, the hyperbola signature enhancement method was performed following the procedures introduced above. The hyperbola recognition results are shown in Figure 7.4 (a–i). There are 4 subplots in each result figure for each potential target zone. On the top left is the original received GPR image over the check range; on the top right is the simple background reduction enhanced GPR image; on the bottom left is the squared value image based on background removed GPR image; on the bottom right is the converted binary image used to recognize hyperbola signatures. (Note that the check range here is narrower than the 30 ft used in the field simply to facilitate presentation and make the hyperbolic returns more easily visible in the figures).

Based on the results described above, targets 4, 5 and 7 can be defined as detection zones. Even though no drain was pre-identified at locations 4 and 7, they are clearly worth close inspection as both employed signal processing algorithms indicate the presence of a buried conduit. The remaining targets would require further investigation. It is important to note that the absence of a hyperbolic return cannot be used as a means to define a false alarm, as results presented earlier for the background reduction algorithm confirm that the statistical approach can identify drains even when no hyperbolic return is evident. Thus the shape enhancement
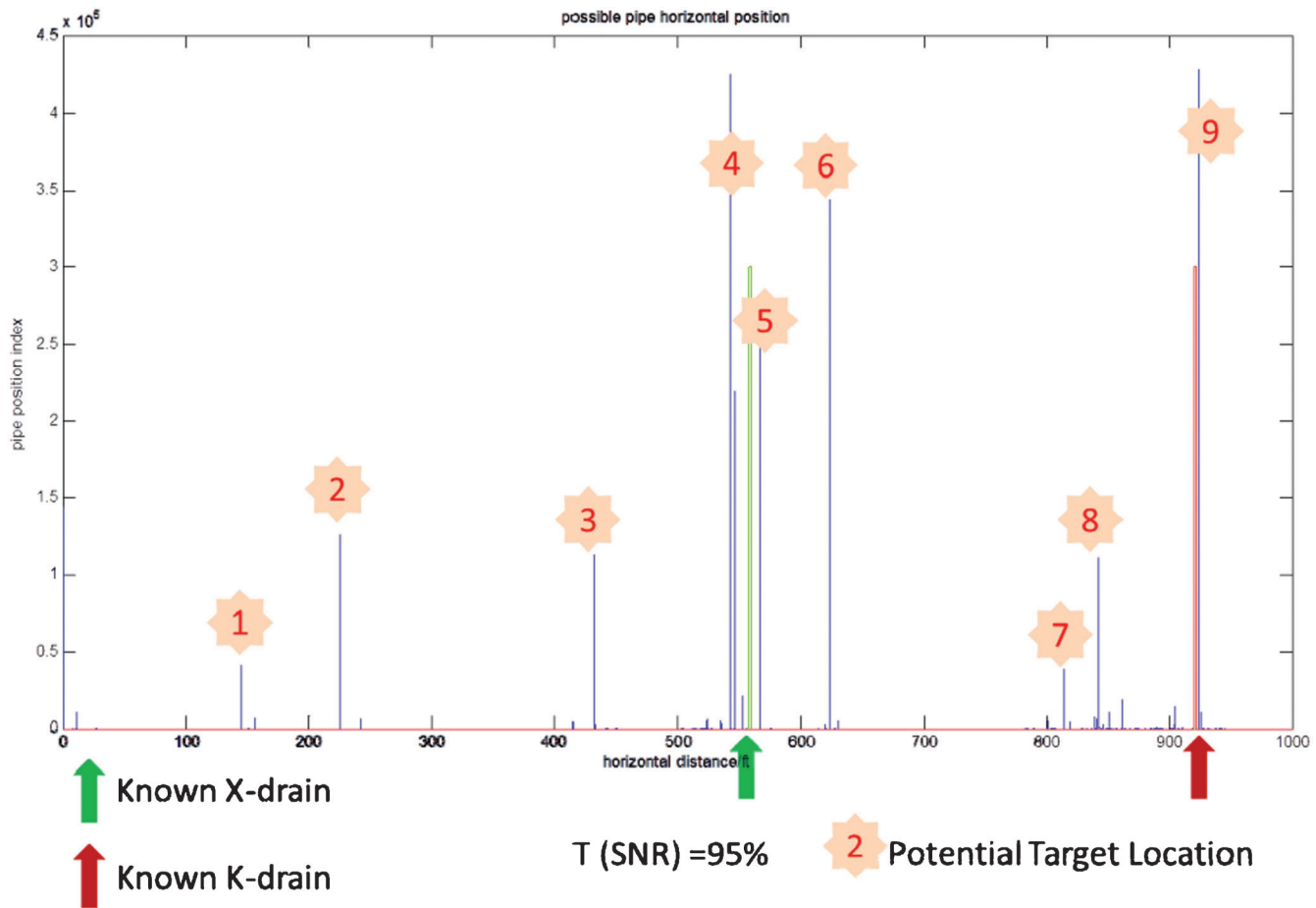
Figure 7.2 Potential target locations (9 in total) obtained by Method 1 with SNR threshold T=95%.

and related shape recognition activities serve mainly as a means to enhance certainty associated with detection zones.

K-Drain detection based on selected layer analysis using Method 1. The I-65N field test was unique in that the study area contained 3 known K-drains. K-drains are metal pipes or clay conduits associated with old pavement systems and are typically buried beneath modern, renovated pavement layers. When roads are reconstructed, the K-drains are often left in place. Over time, if not maintained, K-drains can retain soil, vegetation, and water, which in turn leads to serious pavement damage. Unfortunately, these drains are very difficult to locate as they are often associated with poorly documented construction operations from many years ago and can be hidden by vegetation as shown in Figure 7.5. With this in mind, effort herein was also made to locate K-drains in the I-65N data set.

The field data analyzed in this section was collected from I-65N, as described earlier. In total approximately 2 miles of data was analyzed, from I-65N mile marker 143 to 144, and from mile marker 146-147. As noted above, there were 3 known K-drains along this 2-mile roadway as well as a large transit pipe.

In order to locate K-drains using the analysis algorithms described earlier, a vertical region of the GPR image data is isolated that is likely to contain the K-drains. Based on the discussion above, K-drains were normally buried under new pavement system layers. Consequently, the only area in the original image that should be considered is the area deeper than all the pavement layers, including the X-drain layer, which is normally located in the base layer of pavement.

With this in mind, the signal processing method is then be applied to a vertical range of the GPR data from the 2-mile I-65N field exercise that extends from 1–2 meters below the ground surface. Following the same analysis procedures introduced above for Method 1, the final output of possible K-drain locations is shown in Figures 7.6 and 7.7.

The locations of the known K-drains in the Figures 7.5 and 7.6 are marked by red arrows and red lines. The green lines in the figures indicate locations of known X-drains. The blue lines represent possible target locations resulting from the data analysis. As shown, all 3 known K-drains were successfully detected by the employed algorithm. However, there are also a significant number of "potential" false alarms. These are described as "potential" false alarms because no
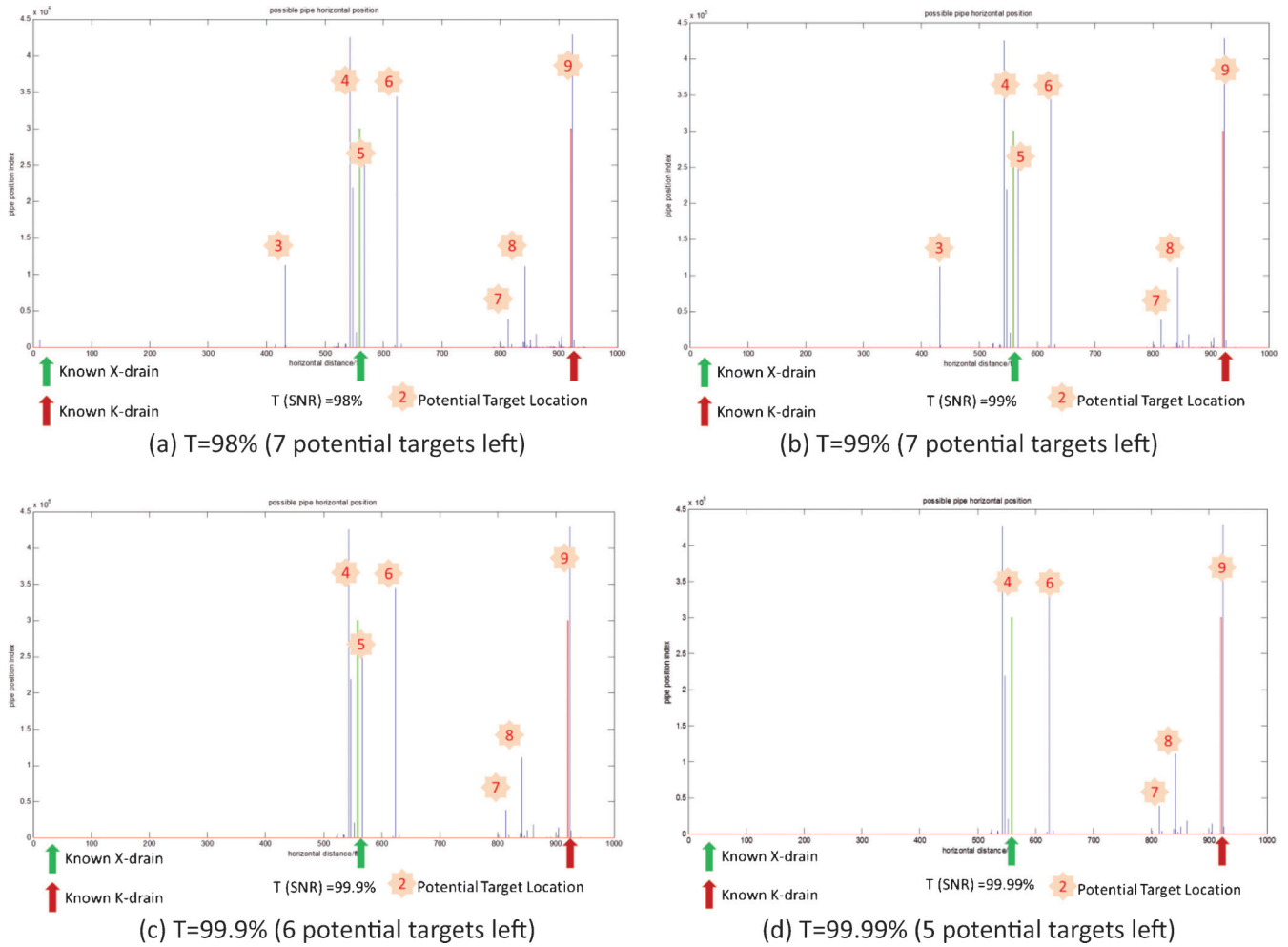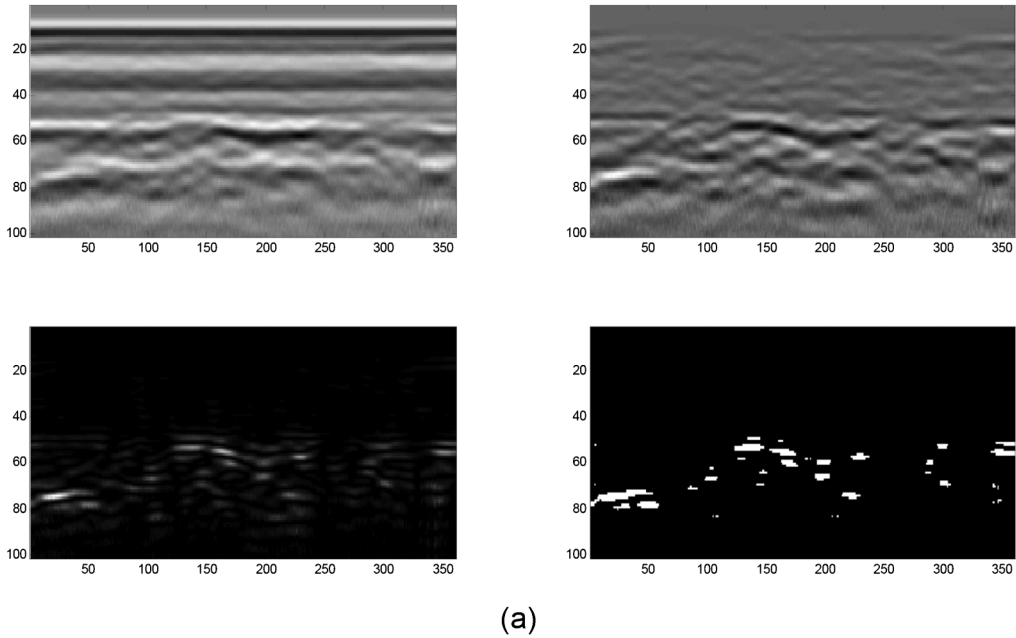
Figure 7.3   Potential target locations from by Method 1 as a function of SNR threshold.

Potential Target 1
Horizontal location: 145ft
Check range: 145±7.5ft (±180 scans)
Hyperbola detection: No hyperbola evident

(a)

Potential Target 2
Horizontal location: 230ft
Check range: 230±7.5ft (±180 scans)
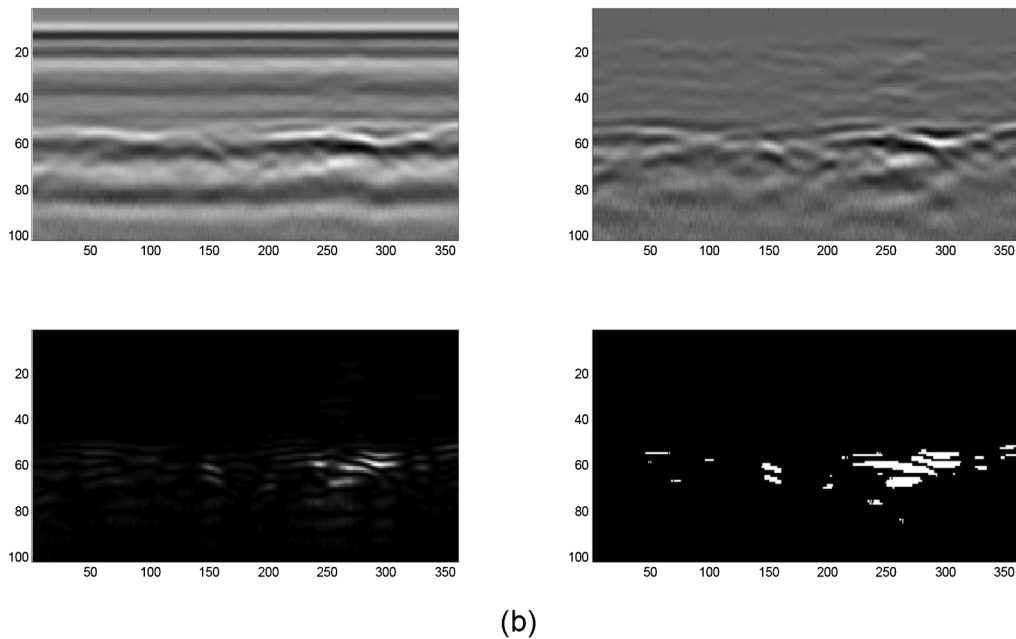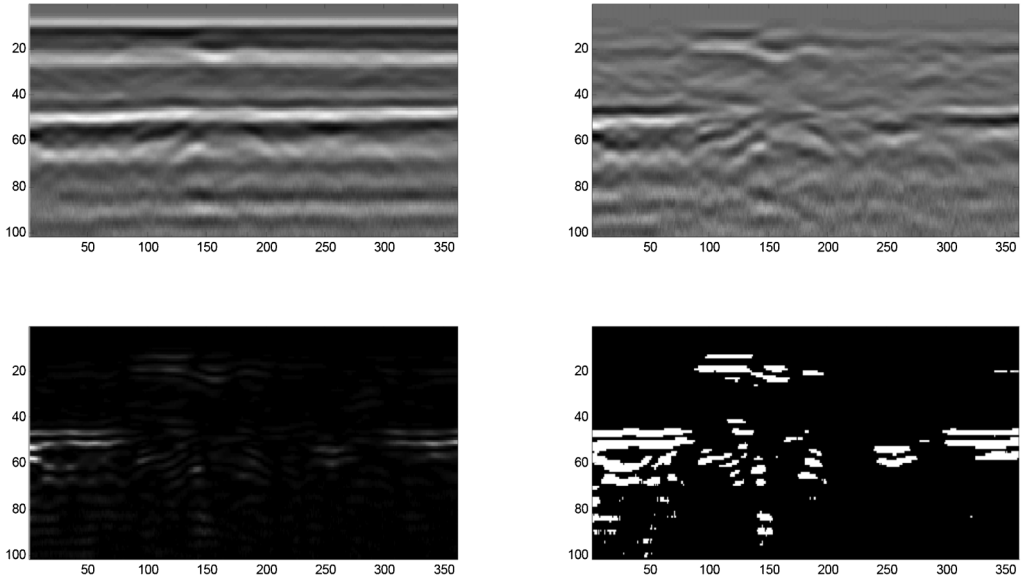Hyperbola detection: No hyperbola evident

(b)

Figure 7.4　Hyperbola recognition results, potential targets 1–9 (a–i).

Potential Target 3

Horizontal location: 410ft

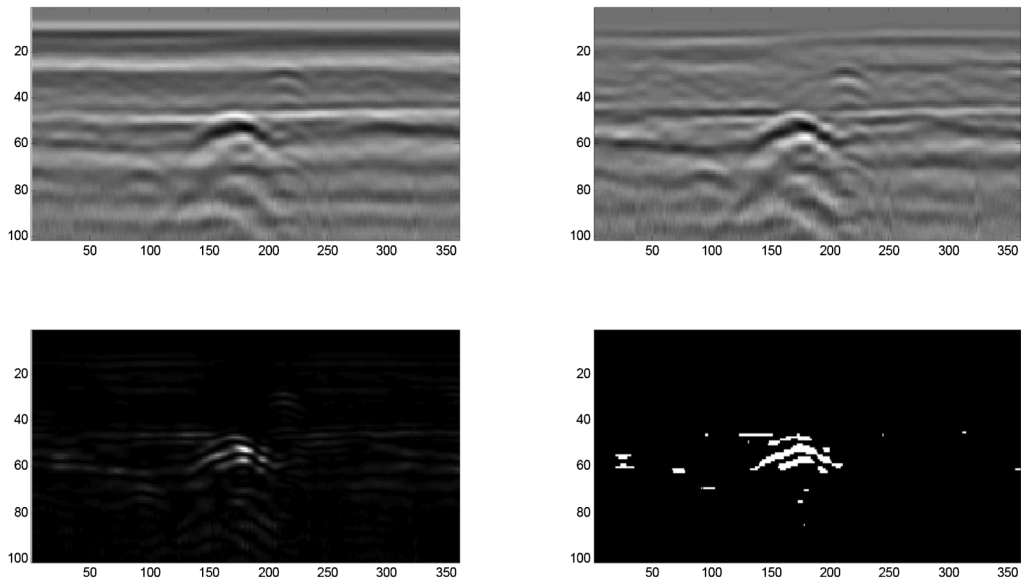Check range: 410±7.5ft (±180 scans)

Hyperbola detection: No hyperbola evident

(c)

Potential Target 4

Horizontal location: 522ft

Check range: 522±7.5ft (±180 scans)

Hyperbola detection: Hyperbola evident (very clear)
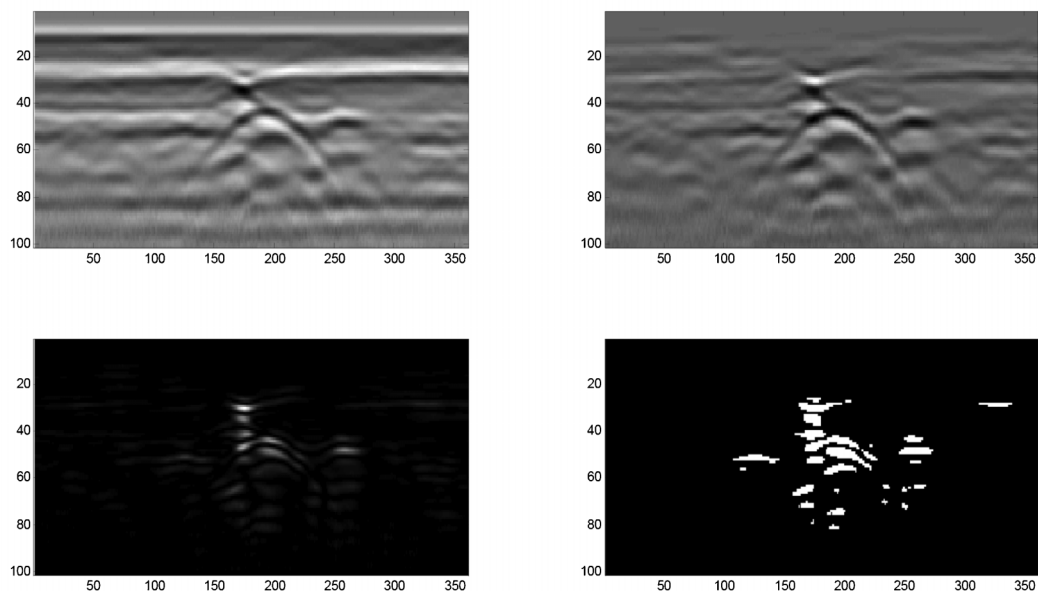

(d)

Figure 7.4   Continued.

Potential Target 5 (known X-drain)

Horizontal location: 557ft

Check range: 557±7.5ft (±180 scans)

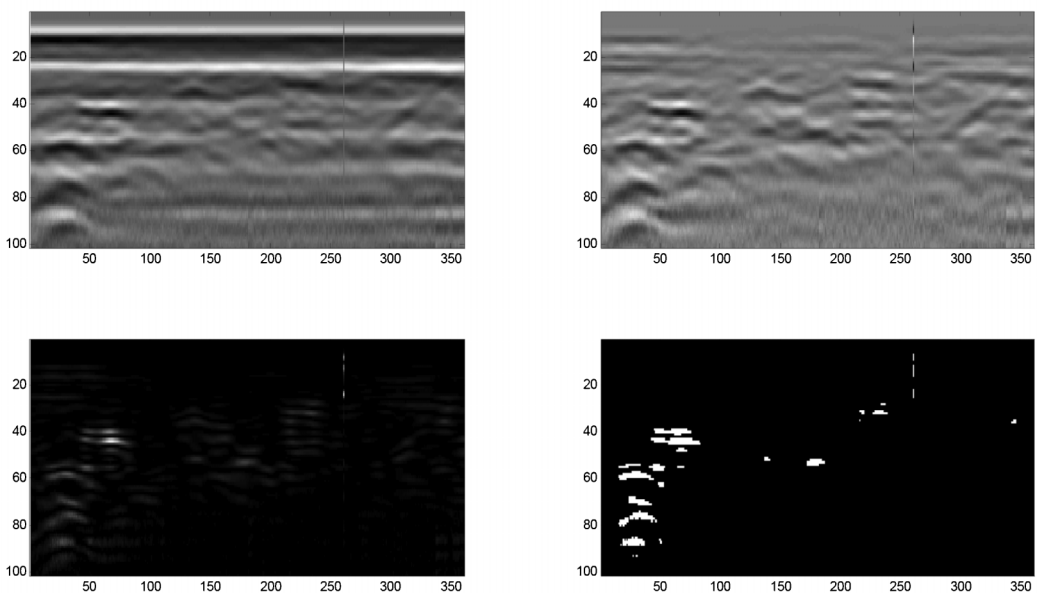Hyperbola detection: Hyperbola evident (very clear)

(e)

Potential Target 6

Horizontal location: 620ft

Check range: 620±7.5ft (±180 scans)

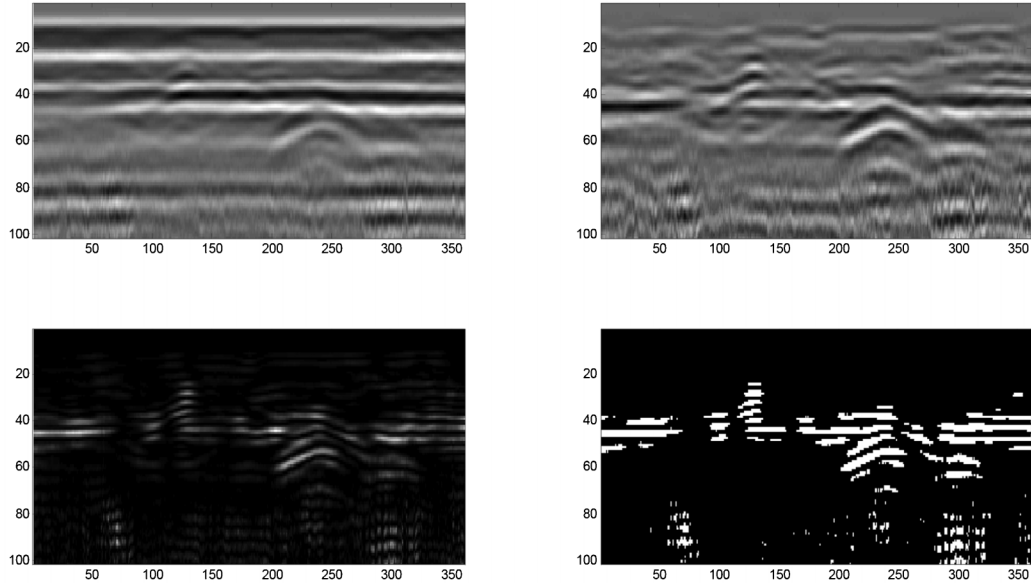Hyperbola detection: No hyperbola evident

(f)

Figure 7.4   Continued.

Potential Target 7
Horizontal location: 820ft
Check range: 820±7.5ft (±180 scans)
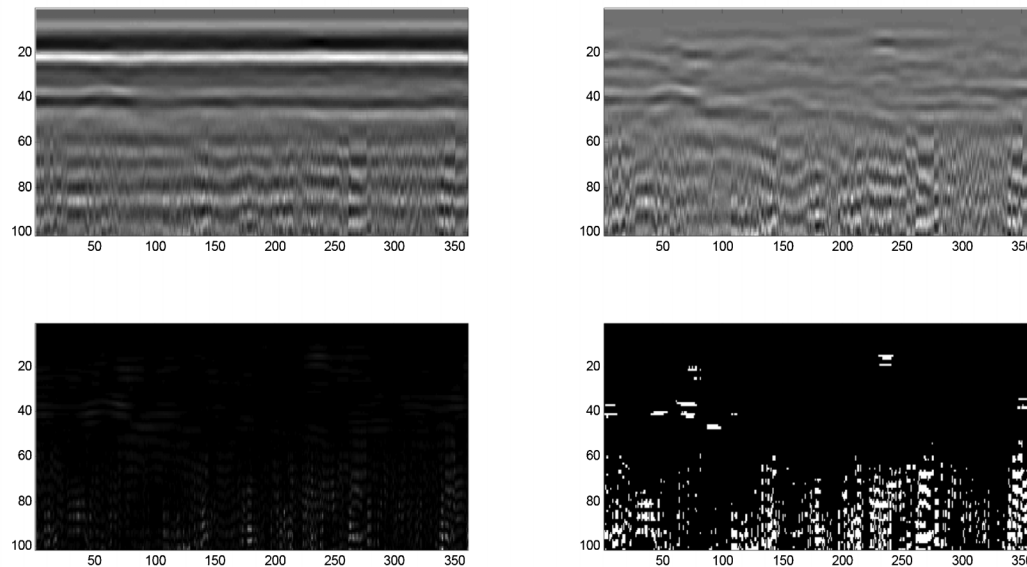Hyperbola detection: Hyperbola evident (clear)

(g)

Potential Target 8
Horizontal location: 860ft
Check range: 860±7.5ft (±180 scans)
Hyperbola detection: No hyperbola evident

(h)

Figure 7.4   Continued.
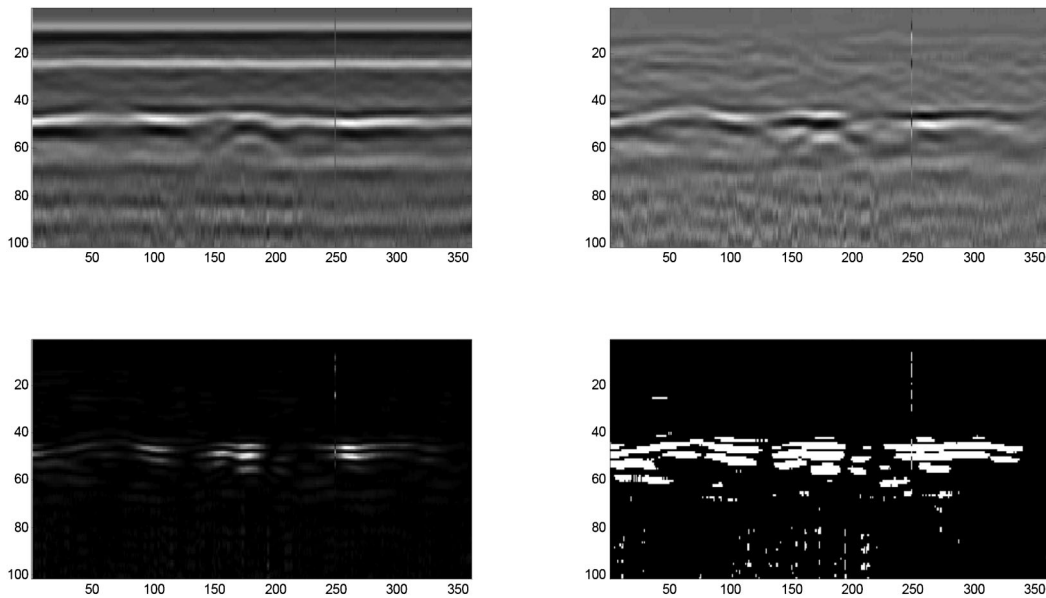
Potential Target 9 (known K-drain)

Horizontal location: 921ft

Check range: 921±7.5ft (±180 scans)

Hyperbola detection: No hyperbola evident (cannot be identified in the binary image but may be recognized the original GPR image and also the background reduction enhanced image)

(i)

Figure 7.4 Continued.

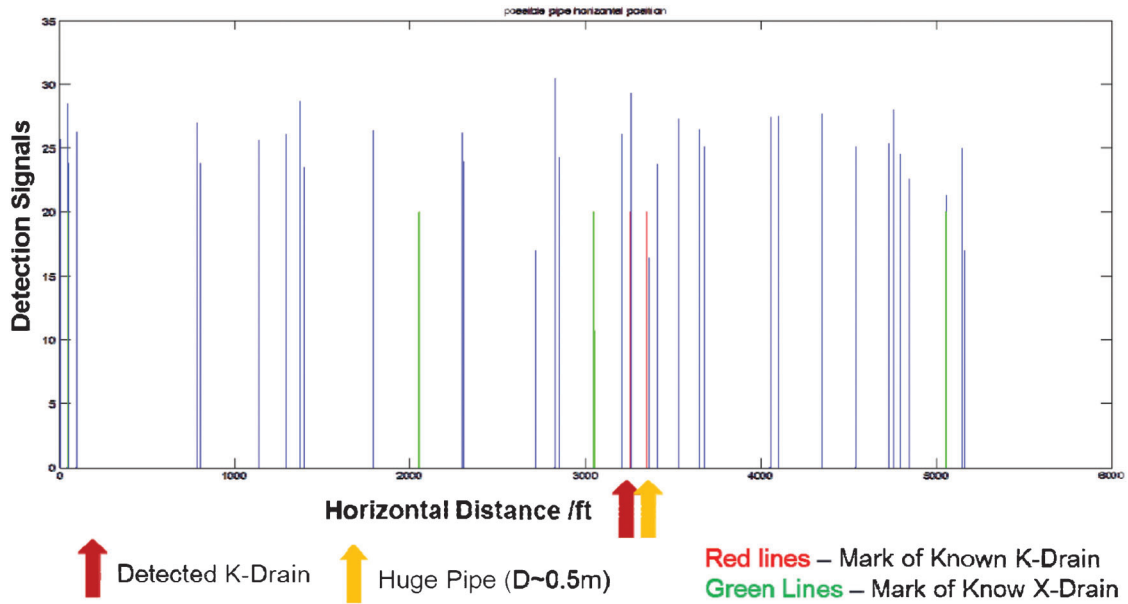**Figure 7.5** Buried K-drains on the side slope of I-65N.

Figure 7.6   Possible K-drain locations determined by Method 1 (I65N 143-144 mi).
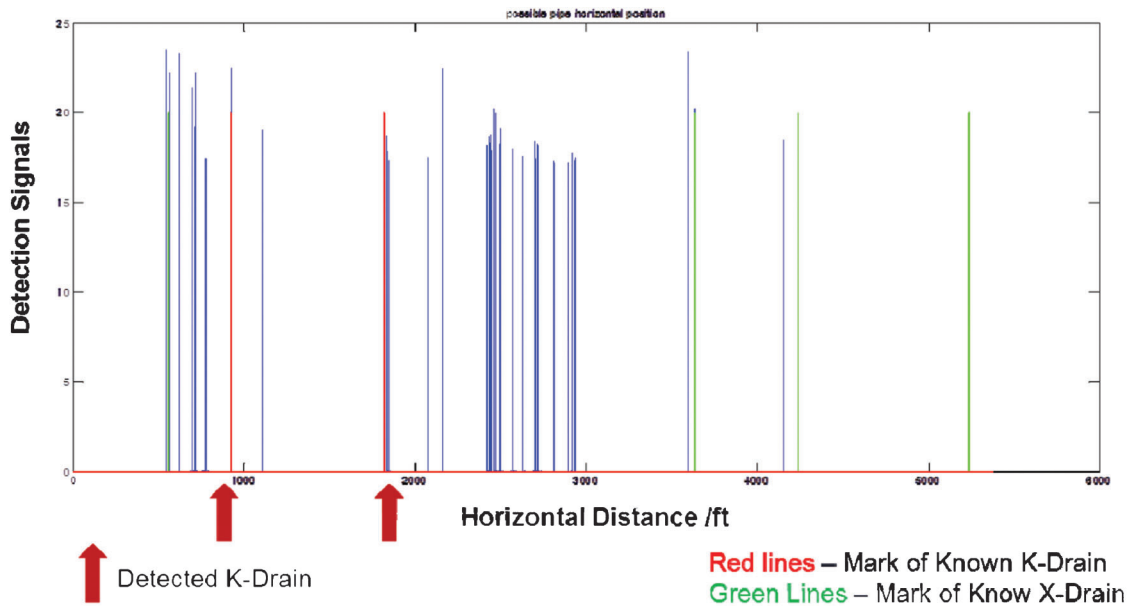

Figure 7.7   Possible K-drain locations determined by Method 1 (I65N 146-147 mi).

field work has been completed to check if there actually is a K-drain at the additional locations identified. Also, it is important to note that conduit spacing rules cannot be applied here as there is no evidence that older construction operations employed uniform spacing for the drains. Thus, some of the inferred targets may indeed be buried conduits, and others, of course, may truly be false alarms. Nonetheless, the fact that all known K-drains were detected is encouraging. Future work should likely be focused on gathering additional validation information, and on reducing false alarms in the K-drain analysis.

8. HARDWARE MODIFICATIONS: FIELD TRIALS OF GPR SYSTEM CONFIGURATIONS

8.1 Overview of Tested Antenna Configurations

In addition to signal processing, a number of possible antenna configurations were explored to assess their potential to improve GPR system sensitivity to sub-pavement drainage conduits. These system configurations were evaluated in the field on the newly constructed section of US-231, close to Purdue Airport. Two 6″ drainage pipes, spaced 8 inches apart as shown in Figure 8.1, were selected as the focal point of the tests, as changes in the quality of the detected signal were sought rather than simple detect vs. non-detect findings.

Over the course of two days in the field, three categories of antenna configurations were assessed, each of which will be introduced separately below.

Dual receivers (Rx). In order to maximize the benefit of the multi-channel GPR system, setups involving multiple antennae were explored. However, due to equipment limitations, only dual receiver configurations were possible in this study because the SIR-30 could not be configured to synchronously pulse two transmitters. With this in mind, emphasis was placed on exploring the benefits of collecting information from two receivers, each designed for different frequencies. Two such configurations were evaluated, each with the antennae aligned parallel to the direction of the roadway, and transverse to the anticipated pipe direction:

Dual receivers: 900 MHz and 400 MHz. In this experiment, one 900 MHz antenna was configured as the transmitter (Tx) and the first receiver (Rx), and

another 400 MHz antenna functioned only as a second receiver (Rx). Figures 8.2 and 8.3 illustrate this setup schematically and as it appeared in the field.

Dual receivers: 400 MHz and 270 MHz. Similar to the first setup, in this experiment, one 400 MHz antenna was operated as the transmitter (Tx) and the first receiver (Rx), and another 270 MHz antenna functioned only as the second receiver (Rx). Figures 8.4 and 8.5 illustrate this setup schematically and as it appeared in the field.

Dual-parallel Tx/Rx. The second category of antennae configurations tested in the field involved the use of two 270 MHz side-by-side Tx/Rx antennae operated in an orientation parallel to the road direction, and transverse to the anticipated pipe direction. This design enables comparison of two sets of data acquired at the same frequency to help eliminate anomalies and reinforce target signals. Figures 8.6 and 8.7 illustrate this setup schematically and as it appeared in the field.

Cross polarization. In addition to the setups introduced above, two types of cross polarization configurations were also tested by employing two 400 MHz antennae. Cross-polarized systems are known to help reduce background clutter and enhance antenna isolation in some applications, leading to improved signal-to-noise. An illustration and the related field setup is shown in Figures 8.8 and 8.9, respectively. This type of configuration is similar to the dual receiver setups described earlier but with one of the receivers turned 90°. In these experiments, only one transmitter was activated, as illustrated in the related figures.

8.2 Results of Field Tests

In this section, results obtained from the field tests introduced above are analyzed and compared.

8.2.1 Dual Frequency Receivers (900 MHz and 400 MHz)

The data analyzed in this section is based on scans of the same target pipe obtained along three different survey paths: a) data collection on the gravel slope; b) data collection on the edge of the pavement shoulder; c)

Figure 8.1 Drainage pipes observed on the new US-231 near Purdue Airport.
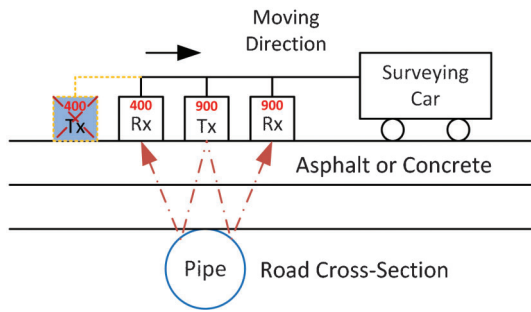
Figure 8.2 Illustration of dual frequency system (900 MHz and 400 MHz).

Figure 8.4 Illustration of dual frequency system (400 MHz and 270 MHz).

data collection in the middle of pavement shoulder. The difference of the obtained data is analyzed as follows.

Original data obtained by GPR system. The data discussed in Figures 8.10, 8.11, and 8.12 is the original data obtained from the GPR system. All the figures below provide two images. The top image in each figure is the signal obtained with 400 MHz receiver and the bottom image is the signal obtained with 900 MHz receiver.

The red arrow in Figures 8.10 through 8.12 provides the horizontal position of the target pipe. The red circle highlghts the reflected signals from the target pipe for each receiving channel. Note that the dual parabolic return seen at early reflection times stems from the points of connection between pavement sections of the roadway.

A review of Figures 8.10 through 8.12 reveals that the buried pipe can be readily identified in the both the 400 and 900 MHz data obtained on the gravel slope. It is also visible in the data obtained on the edge of the pavement shoulder, although the signal is considerably weaker in the 900 MHz dataset relative to the 400 MHz data. However, it is also apparent that the pipe cannot be identified in the data collected in the middle of the pavement shoulder.

Data alalyzed by the background reduction algorithm. Because visible hyperbolic returns were not observed in the data obtained in the middle of the pavement shoulder, the background reduction algorithm introduced in previous sections was applied in an attempt to enhance
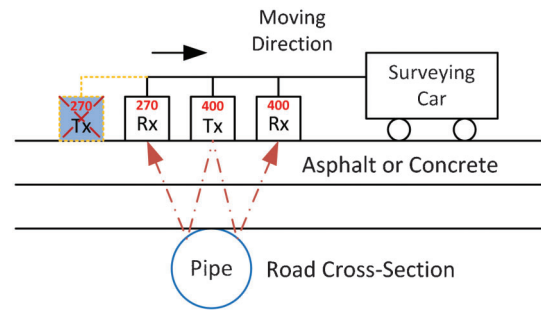
the results. The final result obtained by this analysis is shown in Figure 8.13, and it is clear that the target pipe is readily located as one of two possible targets identified by the algorithm. The red arrow points to the actual pipe position in the field as a reference.

8.2.2 Dual Frequency Receivers (400 MHz and 270 MHz)

Original data obtained by GPR system. Similar to the previous section, Figures 8.14, 8.15, and 8.16 represent images acquired on two different control unit channels. The top image in each figure is the result obtained with the 270 MHz receiver and the bottom image is the result obtained with the 400 MHz receiver. The red arrow in the figures again provides the horizontal position of the target pipe. The red circle, again, highlights the reflected target signals obtained by each receiving channel.

A review of the dual reciever data for the 270 and 400 MHz configurations indicates that the return signal from the buried pipes is readily visible only for the tests performed on the gravel slope. The other data sets are difficult to visually interpret.

Data alalyzed by the background reduction algorithm. The background reduction algorithm was again applied on the data collected in the middle of the pavement shoulder, in which the pipe signal could not be visually identified. As shown in Figure 8.17, the pipe location is clearly identified in the final 1-D result, although two additional false alarms are also indicated. Nonetheless this represents a significant improvement relative to the non-detect status obtained without the algorithm.

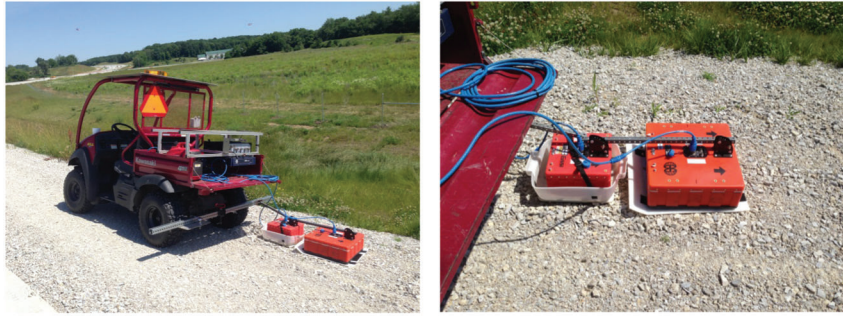**Figure 8.3** Field Setup of dual frequency system (900 MHz and 400 MHz).

Figure 8.5 Field setup of dual frequency system (400 MHz and 270 MHz).

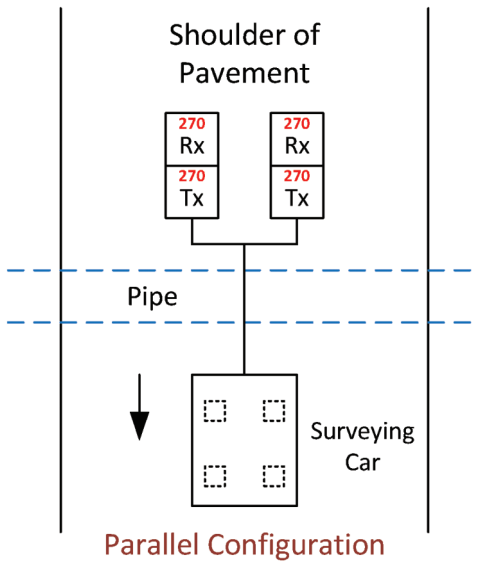**Figure 8.6** Illustration of dual-parallel configuration (270 MHz).

8.2.3 Dual-Parallel Tx/Rx (Two 270 MHz)

Original data obtained by GPR system. The following figures provided the original GPR images obtained by each of the 270 MHz antennae, on both the gravel slope adjacent to the pavement and the shoulder of the pavement. As shown in Figures 8.18 and 8.19, the pipe signals can be picked up clearly in the data obtained on the gravel slope, but cannot be identified in the data from the pavement shoulder.

Data alalyzed by the background reduction algorithm. Just as outlined earlier, the data from the middle of the pavement shoulder is again analyzed using the background reduction algorithm. Results of this analysis are presented in Figure 8.20.

8.2.4 Cross Polarization (Two 400 MHz Antennae)

In this section, the data obtained with the trailing cross-polarized receiver oriented perpendicular to the transmitter and direction of travel (left side of Figure 8.4) is analyzed (cross polarization configuration 1).

Original data obtained by GPR system. In the original data images, the top image is obtained from trailing cross-polarized 400MHz receiver oriented perpendicular to the transmitter and direction of travel and the bottom image is obtained from another 400MHz receiver in the traditional orientation parallel to the direction of travel. Figure 8.21 represents the original GPR image collected on the gravel slope. Figure 8.22 represents the original GPR image collected on the edge of paved shoulder and Figure 8.23 is the original GPR image collected in the middle of the pavement shoulder.

Data alalyzed by the background reduction algorithm. Again here, although the buried drainage pipe is clearly visible in the images obtained on the gravel and the edge of the pavement shoulder, the pipe cannot be discerned in the images obtained in the middle of the pavement shoulder. The background reduction algorithm was therefore applied. The result is presented in Figure 8.24. In addition, the background reduction algorithm was also applied to the
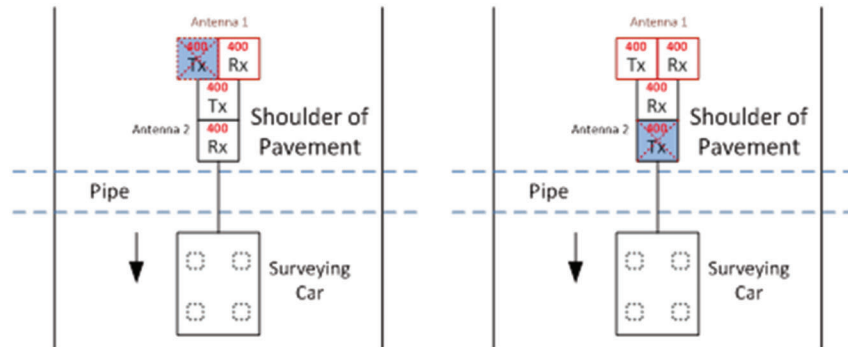

Figure 8.7 Field setup of dual-parallel configuration (270 MHz).

Figure 8.8 Illustration of cross polarization configurations (400 MHz).
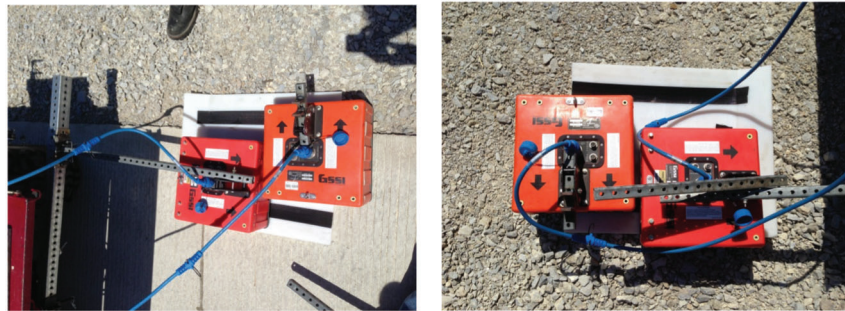

Figure 8.9 Field Setup of cross polarization configurations (400 MHz).

antenna oriented in the traditional direction. This result is presented in Figure 8.25. Although the pipe location is clearly identified with the cross polarized antenna, eight additional false alarms are also indicated.

8.3 Summary and Comparison of Field Trial Results

Based the analyses above, a comparison of the results is presented in Table 8.1 to illustrate the effectiveness of the different antenna configurations and analyses explored. Note that a clear or very clear image is one in which a hyperbolic return is very evident. A "discernable" image is one in which human interpretation yields a detection. Also, note that SNRdb values represent 10 x log base 10 of the ratio of the mean target signal squared divided by the mean background signal squared reported in decibels, as is customary in signal processing.
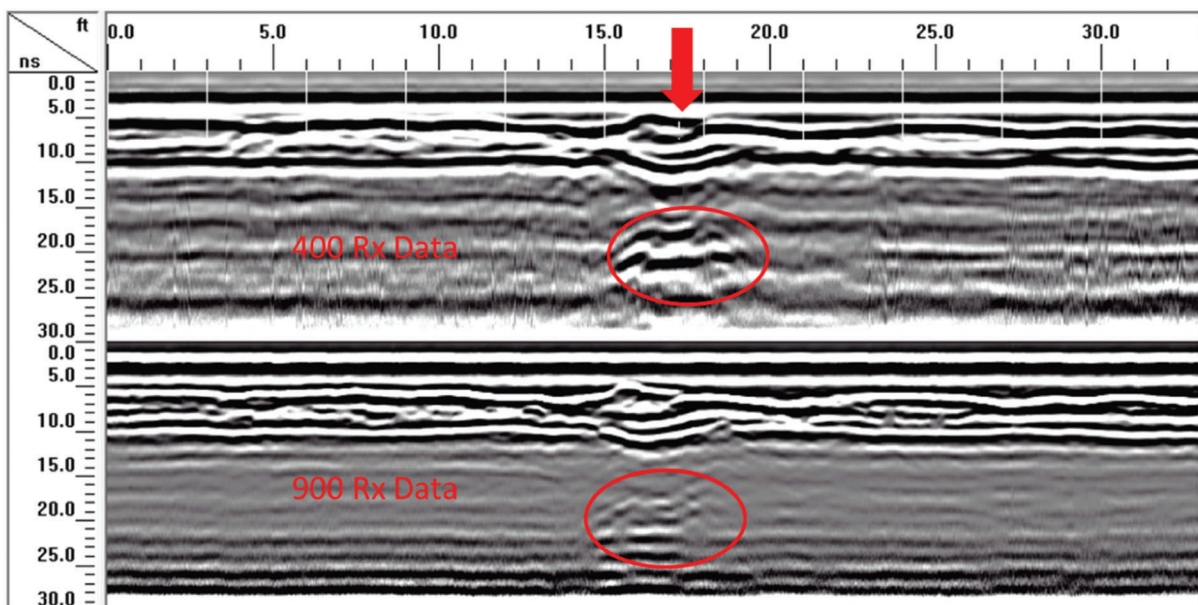

Figure 8.10 The original GPR image collected on the gravel slope (400 MHz and 900 MHz).
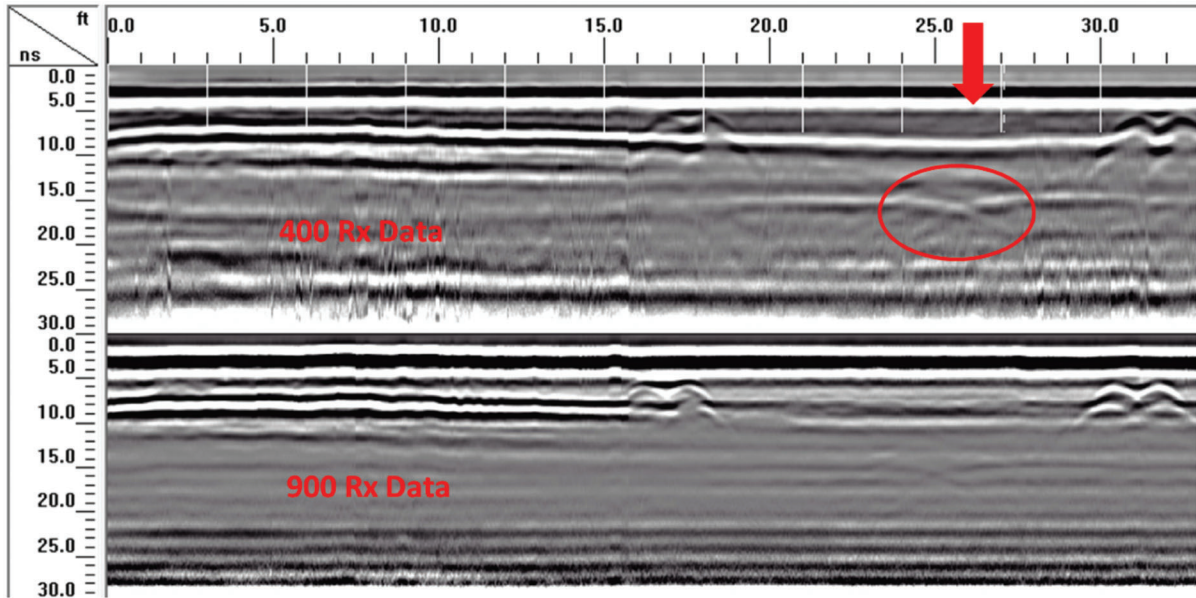
Figure 8.11 The original GPR image collected on the edge of pavement shoulder (400 MHz and 900 MHz).

Figure 8.12 The original GPR image collected in the middle of the pavement shoulder (400 MHz and 900 MHz).

Figure 8.13 Application of the background reduction method to the dual receiver data (400 MHz) obtained in the middle of the pavement shoulder.

Figure 8.14 Original GPR image collected on the gravel slope (270 MHz and 400 MHz).

Figure 8.15 Original GPR image collected on the edge of the pavement shoulder (270 MHz and 400 MHz).
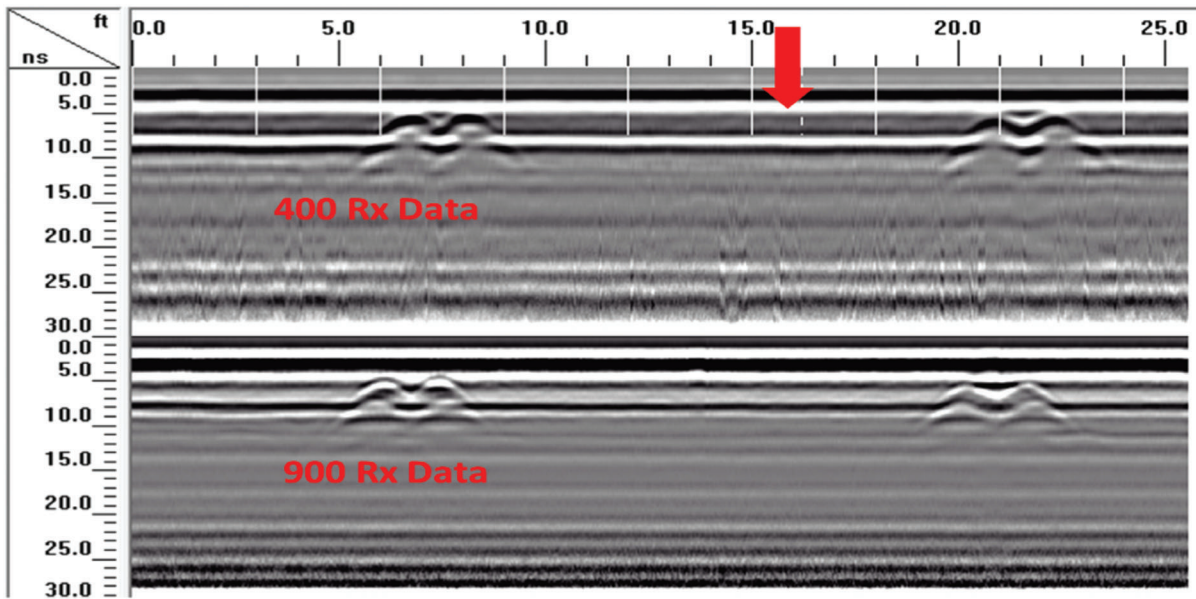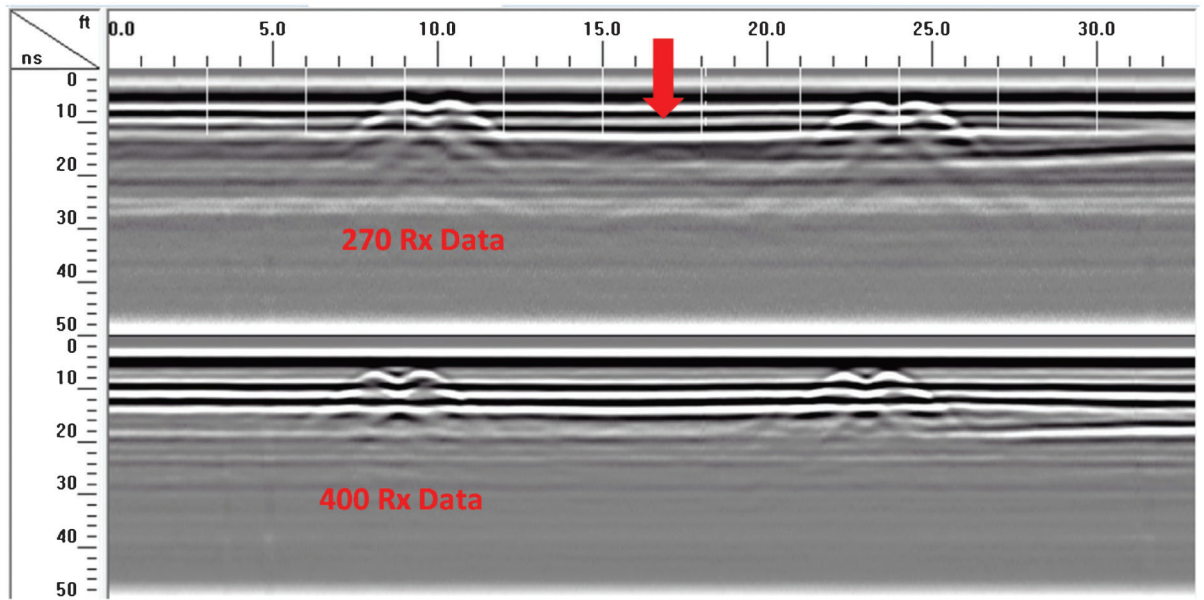

Figure 8.16 Original GPR image collected in the middle of the pavement shoulder (270 MHz and 400 MHz).
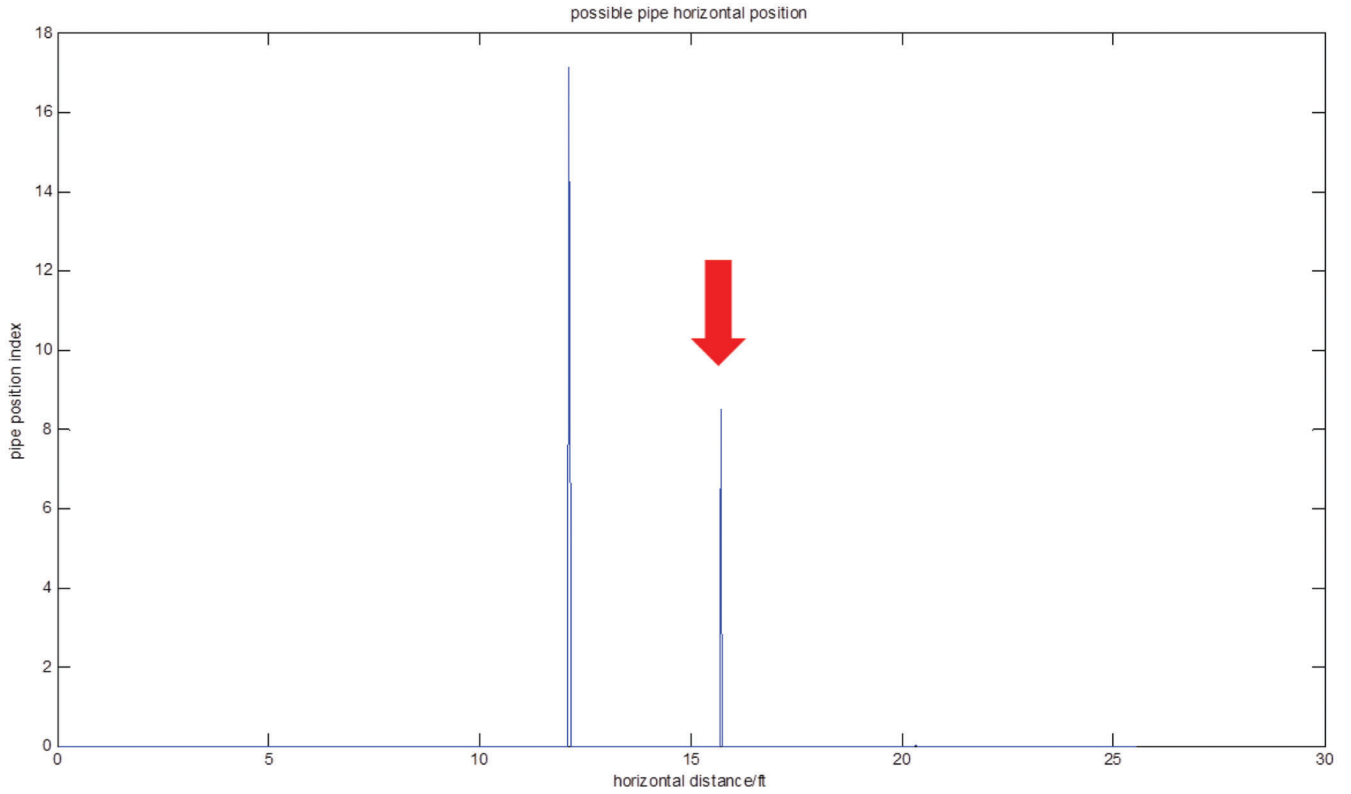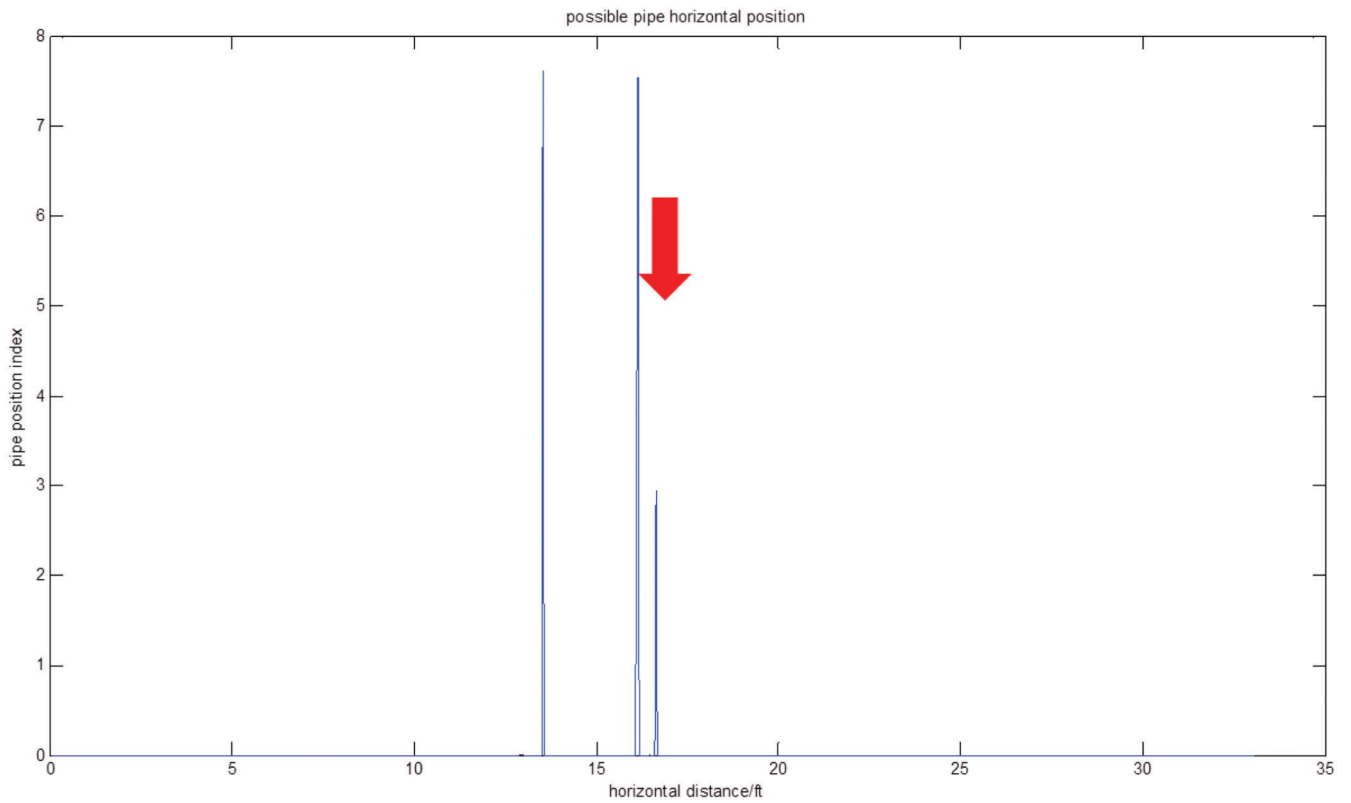
Figure 8.17 Application of the background reduction method to the dual receiver data (270 MHz) obtained in the middle of the pavement shoulder.
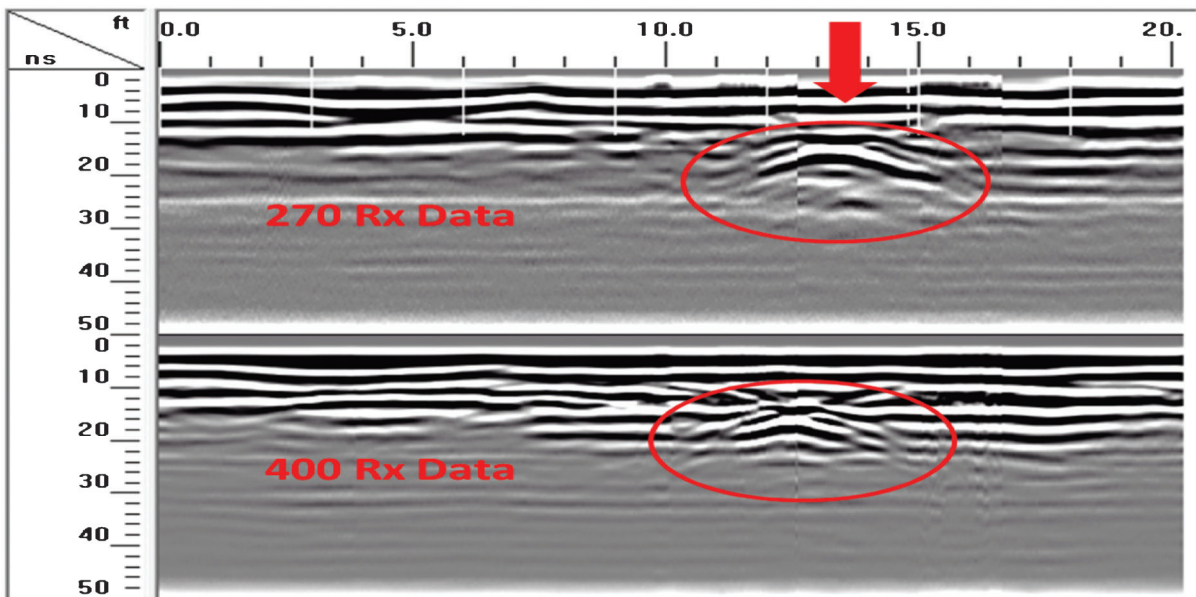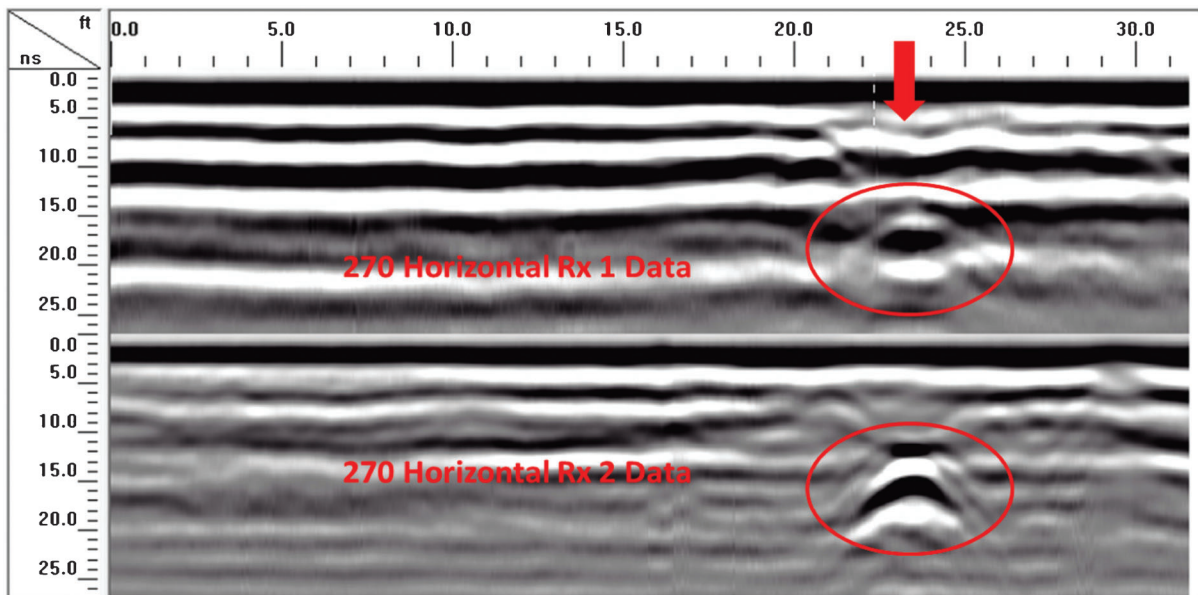

Figure 8.18 Original GPR image collected on the gravel slope (two parallel 270 MHz).
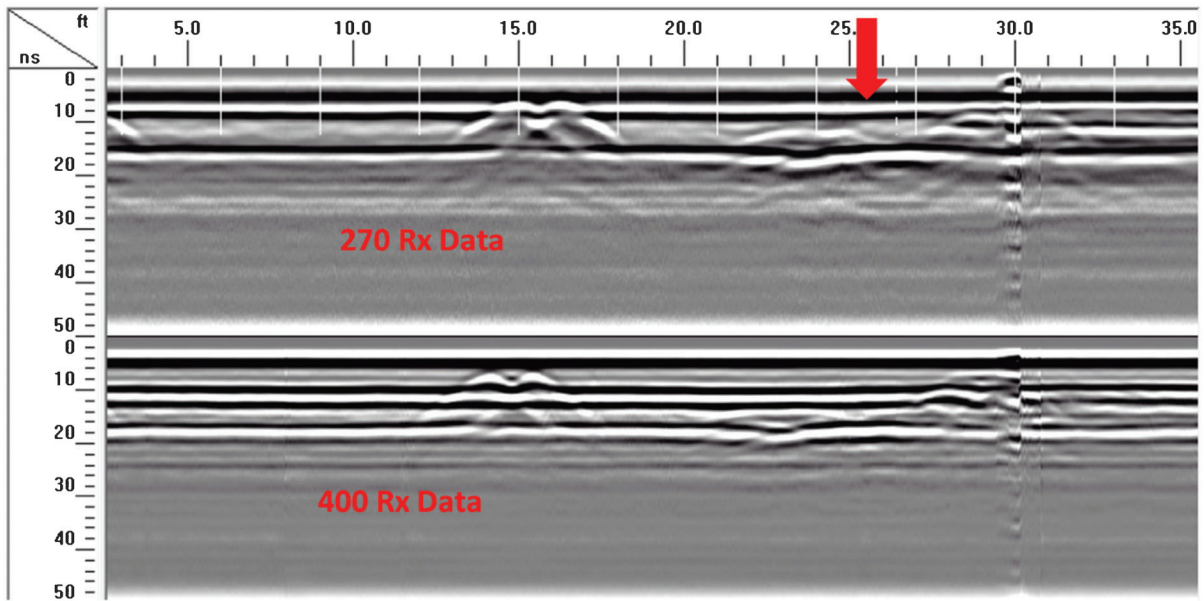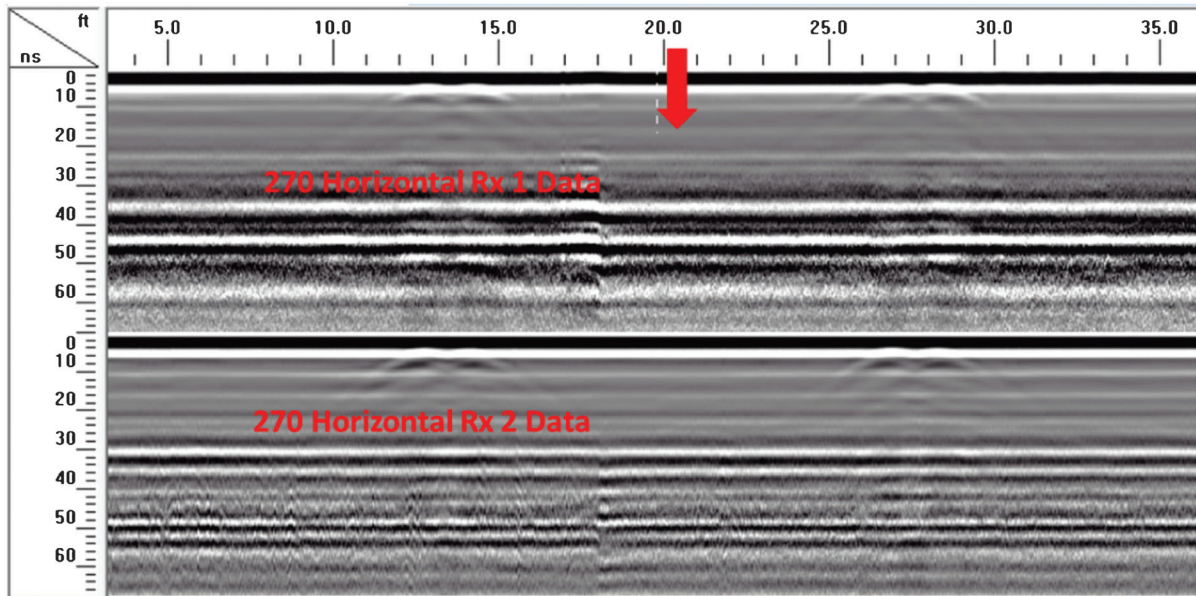
Figure 8.19 Original GPR image collected in the middle of the pavement shoulder (two parallel 270 MHz).
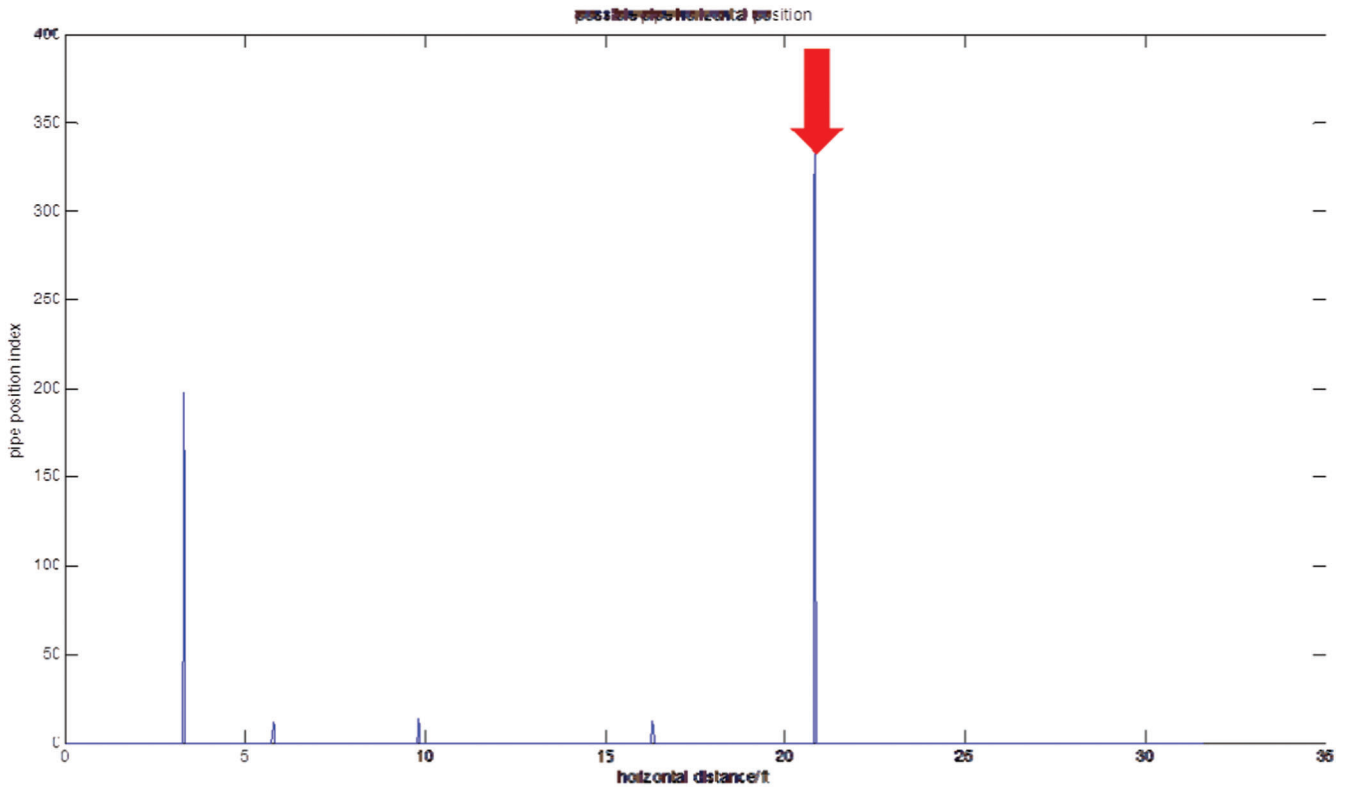
Figure 8.20 Result of background reduction method for dual-parallel Tx/Rx (two 270 MHz) setup (middle of pavement shoulder).
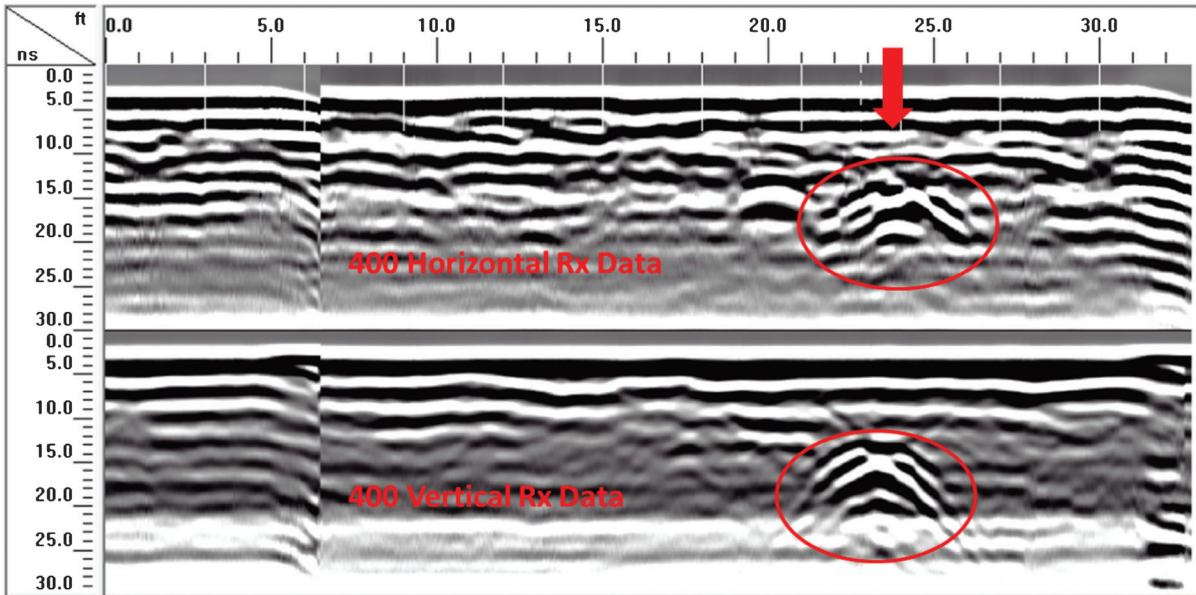
Figure 8.21 Original GPR image collected on the gravel slope (cross polarization configuration 1: 400 MHz).
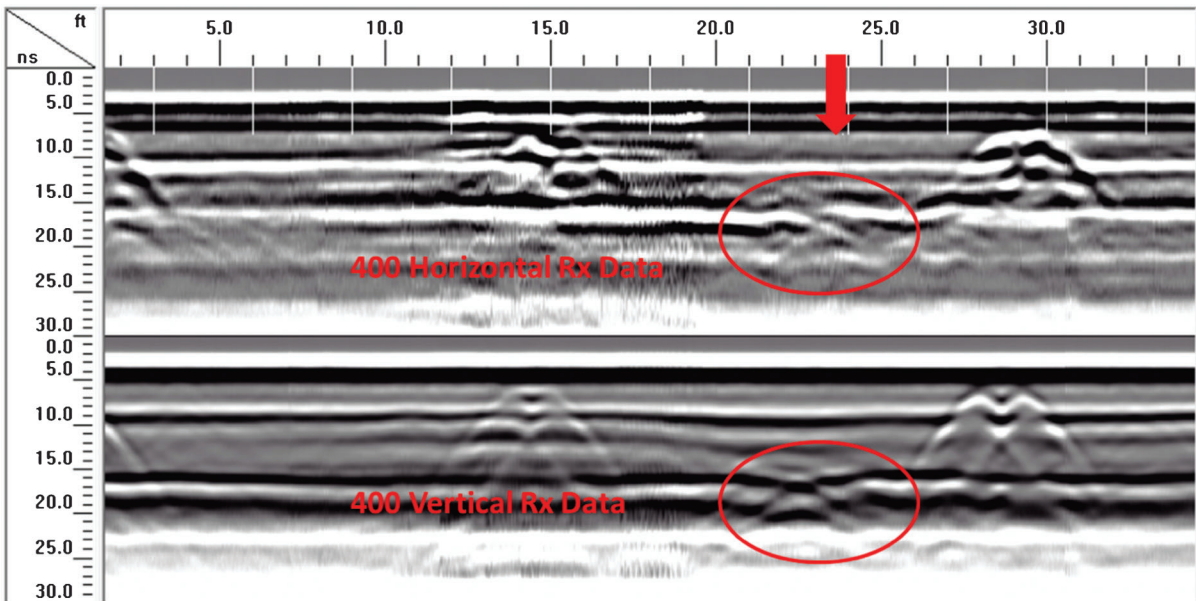
Figure 8.22 Original GPR image collected on the edge of the pavement shoulder (cross polarization configuration 1: 400 MHz).
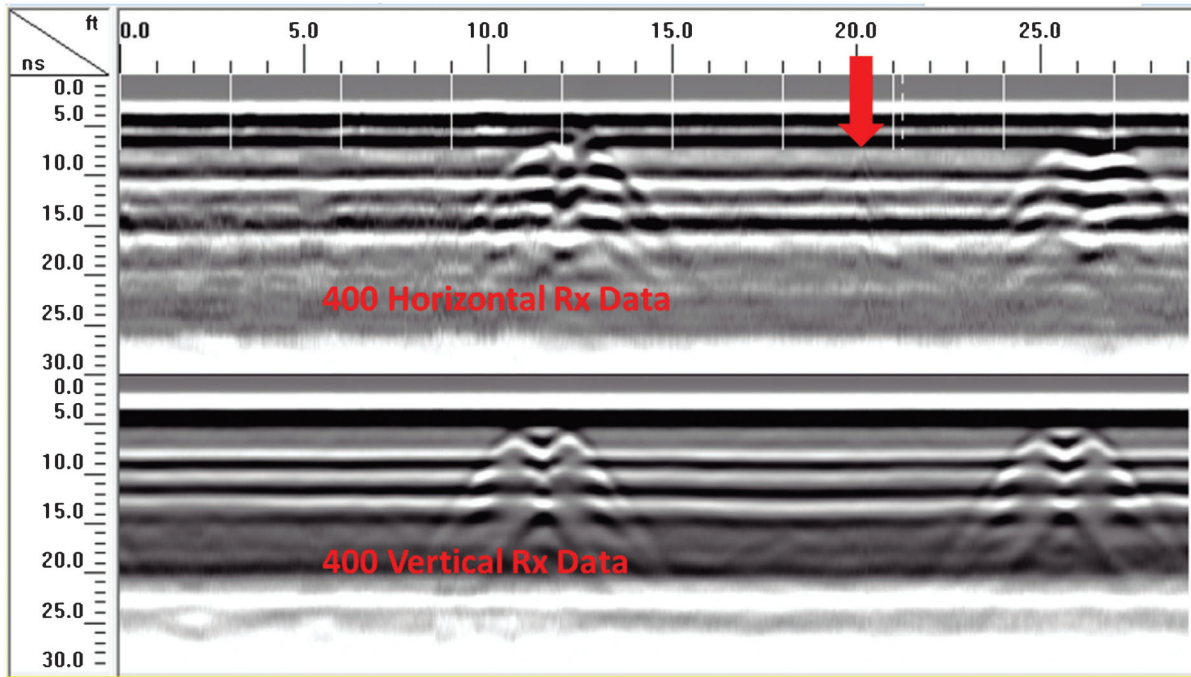
Figure 8.23 Original GPR image collected in the middle of the pavement shoulder (cross polarization configuration 1: 400 MHz).
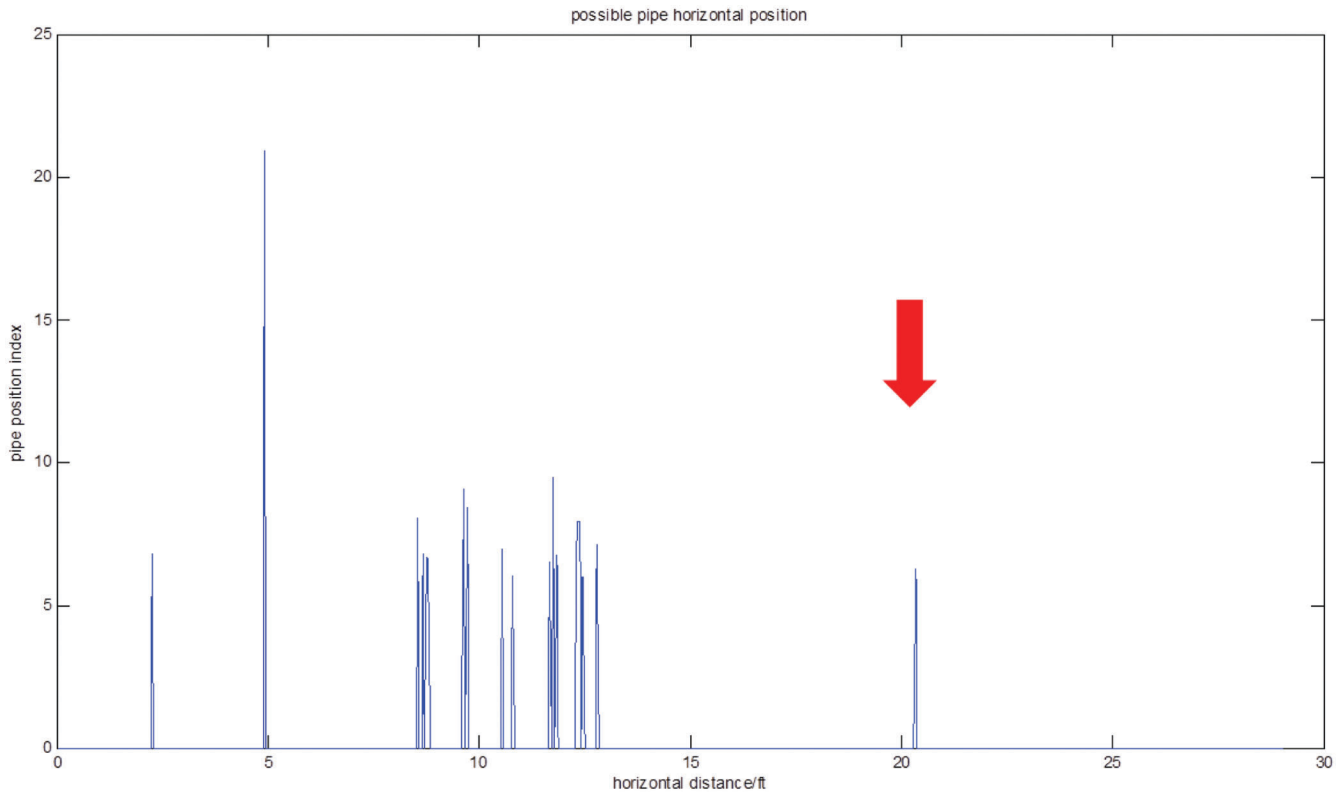
Figure 8.24 Result of background reduction method on data obtained with cross-polarized antenna (cross polarization configuration 1: 400 MHz).
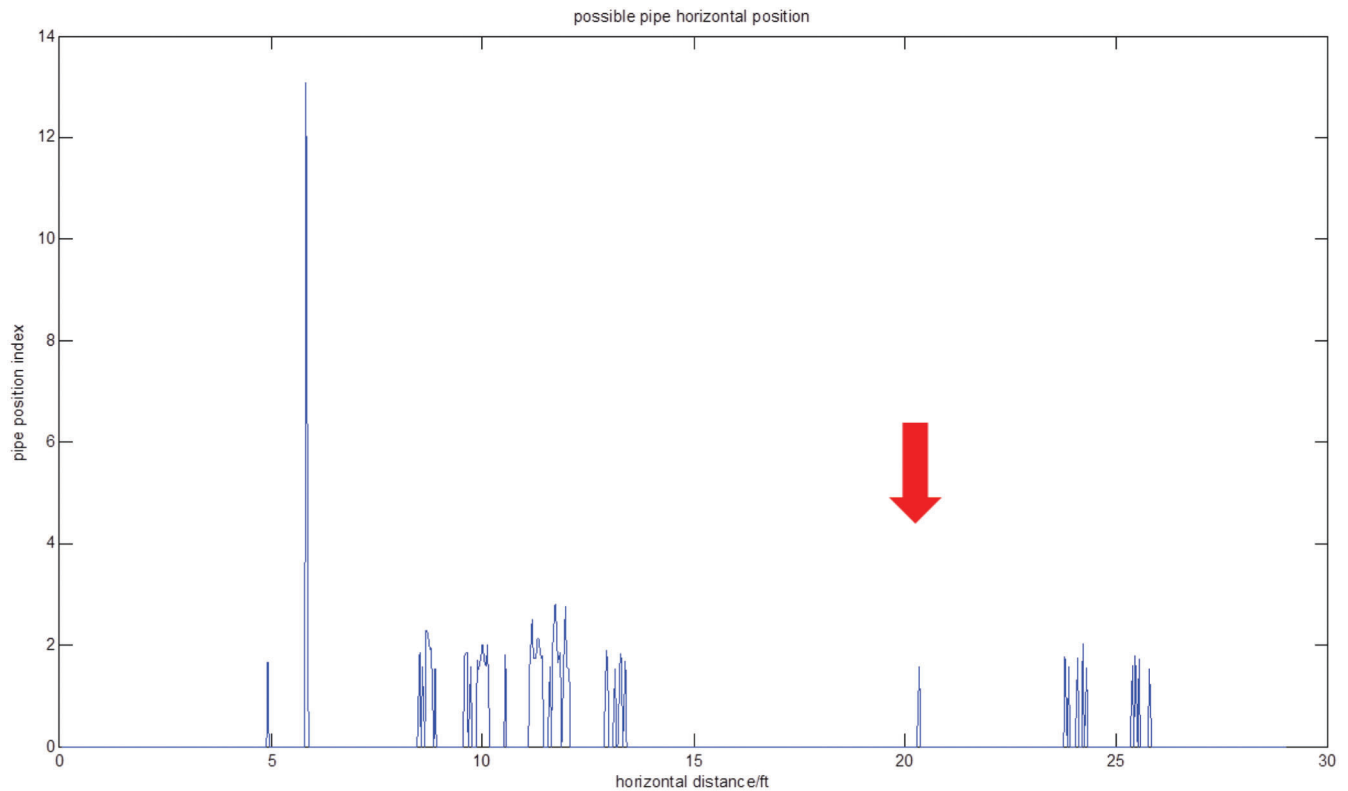
Figure 8.25 Result of background reduction method on data obtained with traditional antenna (cross polarization configuration 1: 400 MHz).

TABLE 8.1
Result Comparison of Different Approach

| Experiment Method Analysis Approach		900-400 Dual Rx	400-270 Dual Rx	Dual-Parallel Tx/Rx (Two 270 MHz)	Cross Polarization (Two 400 MHz)*
Original GPR Image	Gravel	400 Very Clear $(SNR_{dB} \sim 0.2)$; 900 Discernable $(SNR_{dB} \sim -0.06)$	270 Very Clear $(SNR_{dB} \sim 0.16)$; 400 Very Clear $(SNR_{dB} \sim 0.17)$	Very Clear [Ch2 data] $(SNR_{dB} \sim 4.2)$	Very Clear $(SNR_{dB} Rx(H) \sim 0.07)$ $(SNR_{dB} Rx(V) \sim 0.1)$
	Edge	400 Discernable; 900 Not Clear	Not Clear	×	Discernable
	Shoulder	Not Clear [400 MHz data] $(SNR_{dB} \sim -0.06)$	Not Clear [270 MHz data] $(SNR_{dB} \sim 0.04)$	Not Clear [Ch2 data] $(SNR_{dB} \sim 0.74)$	Not Clear $(SNR_{dB} Rx(H) \sim -0.18)$ $(SNR_{dB} Rx(V) \sim -1.78)$
Background Removal Algorighm	Gravel	Position identified clearly with 3 false alarms [400 MHz data] $(SNR_{dB} \sim 12.5)$	Position identified clearly with 2 false alarms [270 MHz data] $(SNR_{dB} \sim 13)$	Position identified clearly [Ch2 data] $(SNR_{dB} \sim 11)$	Position identified with a few false alarms $(SNR_{dB} Rx(H) \sim 9)$ $(SNR_{dB} Rx(V) \sim 9)$
	Edge	×	×	×	×
	Shoulder	Position identified with one false alarm [400 MHz data] $(SNR_{dB} \sim 13)$	Position identified with two false alarms [270 MHz data] $(SNR_{dB} \sim 7)$	Position identified with one false alarm [Ch2 data] $(SNR_{dB} \sim 9.5)$	Position identified with a few false alarms $(SNR_{dB} Rx(H) \sim 9.5)$ $(SNR_{dB} Rx(V) \sim 8.5)$

NOTE: H = cross-polarized receiver; V = standard receiver.

9. SUMMARY AND CONCLUSIONS

As noted earlier, the work carried out in this program involved a two-pronged approach to improve GPR-based sub-pavement drainage system evaluation while maximizing the value of INDOT's pre-existing investment in GPR hardware and remaining within project budget limitations. Two major avenues were explored to achieve improvements in GPR detection success: (1) software-based signal processing and (2) modifications of hardware test configurations.

Two complementary sets of signal processing approaches were developed in this work, referred to herein as Methods 1 and 2. Method 1 involves two signal processing algorithms that are designed to reduce background clutter and noise by taking advantage of the somewhat uniform nature of the strata underlying constructed pavements and to systematically remove anomalous signals. The output of this method is a 1-D plot of potential target locations as a function of distance on the survey line along the roadway. This method proved to be very effective at identifying buried pipes even when a hyperbolic signal return could not be observed in the 2-D data. Generally all X-drains are routinely identified (with only occasional exceptions), with 3 to 4 false alarms per successful detection. Similarly, all known K-drains in the studied field test regions were successfully identified even though none could be observed in the original GPR images, although each successful detection was accompanied by a significant number of potential false alarms. While these false alarms all require field investigation, the effort associated with these investigations is likely substantially less than the effort required to manage the consequences of undetected, and thus unmaintained, K-drains. The reliability of Method 1 was shown to improve when scans obtained with two antennae are compared, and when routine drain spacing is employed as a filter. These additional screens help to reduce false alarms to roughly 2 to 3 per successful detection for X-drains. Note that accurate false alarm statistics could not be developed for K-drains, because the total number of K-drains in the field test area is not known.

Method 2 focuses on enhancing 2-D image quality to facilitate recognition of hyperbolic signal returns indicative of a drain detection. When this method reveals a hyperbola, there is a clear "detect" outcome and thus the approach can clarify interpretation of potential targets identified via Method 1. It is important to note however, that lack of a hyperbolic return in the 2-D image is not conclusive in declaring a "false alarm" as the statistical algorithms of Method 1 routinely detected pipes when no hyperbolic return was visible. Thus, in practice, it is likely important to investigate all potential target zones identified by Method 1. Overall, Method 2 would likely be most valuable if incorporated in an automated data processing system to help rapidly identify clear "detects" and thus limit the focus of in-field investigative study to only truly uncertain target zones.

Field experiments were also carried out in this work to assess the potential for alternative antenna configurations to enhance the detection success. Five different antenna configurations were tested. These tests reveal several conclusions that can be generalized as follows:

1. Survey line selection has a significant influence on the quality of obtained GPR images. In all cases, images obtained on the gravel side slope of roads provided clearer, higher SNR, images of buried drains relative to images obtained in the middle of the shoulder of the roadway, and more frequently displayed the characteristic hyperbolic returns expected from a buried conduit. For example, as described in association with the test of the dual-parallel 270 MHz antennae, the signal to background ratio (SNR_{dB}) on the gravel slope was 11dB and on the shoulder decreased to 9.5dB. While in this particular case, both survey lines resulted in a detection, an enhanced SNR provides the opportunity to detect pipes that may be more deeply buried or in less favorable ground conditions and thus the survey line that routinely provides the greatest SNR should always be sought. It is believed that this result stems from the reduced surface cover over the drains on the gravel slope which permits more energy to reach the target zone. It is also worth noting that while operating on the gravel slope has some challenges in terms of maintaining the stability of the antennae, a survey line well off the roadway adds to the safety of the overall scanning operation. With this in mind, there is likely value in developing a robust outrigger setup that can facilitate antenna coupling with the ground on the gravel slopes beside roadways.
   Tests carried out at the pavement shoulder – gravel slope interface repeatedly yielded poor results. The interface between the pavement edge and the gravel is highly heterogeneous and limits coupling of energy into the subsurface. In addition, it is difficult to obtain a reliable background signal in this region. Survey lines at the pavement shoulder – gravel slope interface should therefore be avoided.

2. Test configurations involving two antennae facilitate more reliable detection strategies than single antennae configurations. As highlighted earlier, the potential to compare results from two antennae along a shared survey line helps to distinguish background clutter and anomalies from actual pipe detections and facilitates signal averaging that can be employed to reduce the net background interference in post-processing. The benefits of this logic likely increase to a limit as additional antennae are added to the test setup. Some researchers have demonstrated the value of employing large antenna arrays, however these types of systems (which can cost hundreds of thousands to millions of dollars to develop (see for example Project ORFEUS being pursued by the European Community)) were cost prohibitive to explore in this study.

3. In tests conducted with a transmitter and dual receivers operating at different frequencies (e.g., 900 Tx and 900/400 Rx; or 400 Tx and 400/270 Rx), higher input frequencies yielded higher SNR_{dB} results than lower input frequencies. However, at any given input frequency results obtained with the lower frequency receiver of the studied pair tended to provide higher SNR_{dB} returns, indicating some loss in energy of the returned signal combined with a beneficial reduction in sensitivity to noise.

4. Cross polarized configurations generally provided good results but did not yield a benefit that justified the added complexity of operating the cross polarized system. It is

important to note that only configurations involving a cross-polarized receiver oriented perpendicular to the transmitter and direction of travel and vice versa were pursued in this work. Other orientations of the entire cross-polarized setup (e.g., 45° relative to the direction of travel), may warrant future investigation.

Based on the tests and data analyses performed herein, the following recommendations are provided to guide future deployments of GPR for subsurface drainage detection under pavements:

1. Implement the background reduction and anomaly detection algorithms developed in this work (Method 1) in a user-friendly software application that can be employed to process GPR data.
2. Implement the shape enhancement algorithms developed in this work (Method 2) to facilitate evaluation of potential target zones via an automated shape recognition routine.
3. Enhance on-board computing power employed in the field vehicle used to pull the GPR antennae so that data can be processed in real time, thereby enabling target zone marking during the GPR scanning operation (vs. post–data processing).
4. Develop a robust GPR unit outrigger capable of negotiating the gravel slopes alongside roadways to maximize energy coupling into the subsurface and enhance detection sensitivity.
5. Deploy (at least) two antennae in any survey operation to improve background management and facilitate results comparison that can increase the probability of successful detection and false alarm rejection.
6. Utilize configurations involving one transmitter and dual-frequency high-low receiver pairs to optimize energy input into the subsurface and minimize received noise. (Note the simulations indicated that a dual-transmitter shared frequency system would be promising but equipment limitations prevented field study of this configuration).

Beyond these recommendations, this study also identified several issues that likely warrant future research, such as:

1. Increasing the offset between transmitters and receivers of the same frequency. Simulations carried out in this study showed improvements in detection sensitivity with an offset between the Tx and Rx antennae. Unfortunately, due to the design of the equipment utilized in this study, this configuration change could not be evaluated and may prove helpful in challenging detection circumstances.
2. Employing unique sensing techniques to overcome the challenges posed by water in the soil. As noted throughout this report, it is hypothesized that some sub-pavement drains may be positioned in clay layers that also tend to retain moisture, thus limiting propagation of electromagnetic radiation at typical GPR frequencies, which makes it challenging to detect their location. With this in mind, two avenues of future research may be helpful to enhance the pipe detection rate and reduce false alarms in these difficult conditions:

   a. It may be useful to combine the GPR unit with a commercial grade metal detector in an attempt to increase effectiveness in locating metal K-drains by inducing and subsequently monitoring for changes in magnetic field;

   b. It may also be helpful to exploit recent research on propagation of electromagnetic waves through water in the frequency range of 3-100 MHz to minimize the influence of water, which may be especially common in clay layers.

3. Significantly refining the hardware design of the GPR system to enable step frequency analysis and/or the use of dielectric focusing elements to enhance energy coupling with the ground.

REFERENCES

1. Jeong, H. S., C. A. Arboleda, D. M. Abraham, D. W. Halpin, and L. E. Bernold. *Imaging and Locating Buried Utilities*. Publication FHWA/IN/JTRP-2003/12. Joint Transportation Research Program, Indiana Department of Transportation and Purdue University, West Lafayette, Indiana, 2003. doi: 10.5703/1288284313237.
2. Allred, B. J., N. R. Fausey, L. Peters Jr., C. Chen, J. J. Daniels, and H. Youn. Detection of Buried Agricultural Drainage Pipe with Geophysical Methods. *Applied Engineering in Agriculture*, Vol. 20, No. 3, 2004, pp. 307–318. http://handle.nal.usda.gov/10113/9974.
3. Szuch, R. P., J. G. White, M. J. Vepraskas, and J. A. Doolittle. Application of Ground Penetrating Radar to Aid Restoration Planning for a Drained Carolina Bay. *Wetlands*, Vol. 26, No. 1, 2006, pp. 205–216. doi: 10.1672/0277-5212(2006)26[205:AOGPRT]2.0.CO;2.
4. Hunaidi, O., and P. Giamou. Ground-Penetrating Radar for Detection of Leaks in Buried Plastic Water Distribution Pipes. *Proceedings of 7th International Conference on Ground Penetrating Radar (GPR' 98)*, Lawrence, Kansas, May Vol. 27–28, 1998, pp. 783–786.
5. Rmeili, E., and T. Scullion. Detecting Stripping in Asphalt Concrete Layers Using Ground Penetrating Radar. In *Transportation Research Record: Journal of the Transportation Research Board*, No. 1568, Transportation Research Board of the National Academies, Washington, D.C., 1997, pp. 165–174. doi: 10.3141/1568-20.
6. Halabe, U., H.-L. Chen, V. Bhandarkar, and Z. Sami. Detection of Sub-Surface Anomalies in Concrete Bridge Decks using Ground Penetrating Radar. *ACI Materials Journal*, Vol. 94, No. 5, 1997, pp. 396–408.
7. Maierhofer, C. Nondestructive Evaluation of Concrete Infrastructure with Ground Penetrating Radar. *Journal of Materials in Civil Engineering*, Vol. 15, No. 3, 2003, p. 287. doi: 10.1061/(ASCE)0899-1561(2003)15:3(287).
8. Devaru, D., U. B. Halabe, B. Gopalakrishnan, and S. Agrawal. Ground Penetrating Radar (GPR) Based System for Nondestructive Detection of Interior Defects in Wooden Logs. *International Journal of Manufacturing Research*, Vol. 3, No. 4, 2008, pp. 425–451. doi: 10.1504/IJMR.2008.020903.
9. INDOT. *Road Design Manual*. Indiana Department of Transportation, 2010.
10. Harris, D. W. Pavement Thickness Evaluation Using Ground Penetrating Radar. Doctoral dissertation, Purdue University, West Lafayette, Indiana, 2006.
11. Hagen, M. G., and G. R. Cochran Comparison of Pavement Drainage Systems. In *Transportation Research Record: Journal of the Transportation Research Board*, No. 1519, Transportation Research Board of the National Academies, Washington, D.C., 1996, pp. 1–10. doi: 10.3141/1519-01.

12. Mallela, J., L.Titus-Glover, and M. Darter. Considerations for Providing Subsurface Drainage in Jointed Concrete Pavements. In *Transportation Research Record: Journal of the Transportation Research Board*, No. 1709, Transportation Research Board of the National Academies, Washington, D.C., 2000, pp. 1–10. doi: 10.3141/1709-01.

13. Ring, G. W. Drainage of Concrete Pavement Structures. *Proceedings of the International Conference on Concrete Pavement Design*, Purdue University, 1977, pp. 365–381.

14. Ahmed, Z., T. D. White, and P. L. Bourdeau. *Pavement Drainage and Pavement-Shoulder Joint Evaluation and Rehabilitation.* Publication FHWA/IN/JHRP-93/02-2. Joint Highway Research Project, Indiana Department of Transportation and Purdue University, West Lafayette, Indiana, 1993. doi: 10.5703/1288284314209.

15. AASHTO. *AASHTO Guide for Design of Pavement Structures.* American Association of State Highway and Transportation Officials, Washington, D.C., 1986.

16. Hassan, H. F., T. D. White, R. S. McDaniel, and D. H. Andrewski. Indiana Subdrainage Experience and Application. In *Transportation Research Record: Journal of the Transportation Research Board*, No. 1519, Transportation Research Board of the National Academies, Washington, D.C., 1996, pp. 41–50. doi: 10.3141/1519-06.

17. Stimson, G. *Introduction to Airborne Radar*, 2nd edition. SciTech Publishing, Inc., Raleigh, North Carolina, 1998.

18. Loulizi, A. Development of Ground Penetrating Radar Signal Modeling and Implantation for Transportation Infrastructure Assessment. Doctoral dissertation, Virginia Polytechnic Institute and State University, Blacksburg, Virginia, 2001.

19. Attoh-Okine, B. Engineering-Economic Assessment of Paved Road Thickness Using Ground Penetrating Radar (GPR). Doctoral dissertation, University of Kansas, Lawrence, Kansas, 1993.

20. Hubbard, S., J. Chen, K. Williams, J. Peterson, and Y. Rubin. Environmental and Agricultural Applications of GPR. In *Proceedings of the 3rd International Workshop on Advanced Ground Penetrating Radar*, 2005, pp. 45–49.

21. Kowalsky, M. B., S. Finsterle, J. Peterson, S. Hubbard, Y. Rubin, E. Majer, A. Ward, and G. Gee. Estimation of Field-scale Soil Hydraulic and Dielectric Parameters through Joint Inversion of GPR and Hydrological Data. W11425. *Water Resources Research*, Vol. 41, No. 11, 2005. doi: 10.1029/2005WR004237.

22. Linde, N., J. Chen, M. B. Kowalsky, and S. Hubbard. Hydrogeophysical Parameter Estimation Approaches for Field Scale Characterization. *Applied Hydrogeophysics*, Vol. 71, 2006, pp. 9–44. doi: 10.1007/978-1-4020-4912-5_2.

23. Beres, M. Jr., and F. P. Haeni. Application of Ground-Penetrating-Radar Methods in Hydrogeologie Studies. *Ground Water*, Vol. 29, No. 3, 1991, pp. 375–386. doi: 10.1111/j.1745-6584.1991.tb00528.x.

24. Inman, D. J., J. T. Ammons, R. E. Yoder, and R. S. Freeland. Soil Investigations Using Electromagnetic Induction and Ground-Penetrating Radar in Southwest Tennessee. *Soil Science Society of America Journal*, Vol. 66, No. 1, 2002, pp. 206–211. doi: 10.2136/sssaj2002.2060.

25. Yoder, R. E., R. S. Freeland, J. T. Ammons, and L. L. Leonard. Mapping Agricultural Fields with GPR and EMI to Identify Offsite Movement of Agrochemicals. *Journal of Applied Geophysics*, Vol. 47, No. 3, 2001, pp. 251–259. doi: 10.1016/S0926-9851(01)00069-6.

26. Oleschko, K., G. Korvin, A. Muñoz, J. Velazquez, M. E. Miranda, D. Carreon, et al. Mapping Soil Fractal Dimension in Agricultural Fields with GPR. *Nonlinear Processes in Geophysics*, Vol. 15, No. 5, 2008, pp. 711–725. doi: 10.5194/npg-15-711-2008.

27. Gish, T. J., C. S. T. Daughtry, C. L. Walthall, and K. J. S. Kung. Quantifying Impact of Hydrology on Corn Grain Yield Using Ground-Penetrating Radar. In *Proceedings of the Tenth International Conference on Ground Penetrating Radar (GPR), IEEE*, 2004, pp. 493–496.

28. Woeckel, S., M. Konstantinovic, J. Sachs, P. S. Lammers, and M. Kmec. Application of Ultra-Wideband M-Sequence-Radar to Detect Sugar Beets in Agricultural Soils. In *11th International Conference on Ground Penetrating Radar*, June 2006, pp. 19–22.

29. Allred, B., N. Fausey, J. Daniels, C. Chen, L. Peters, and H. Youn. Considerations for Using Ground Penetrating Radar to Locate Buried Agricultural Drainage Pipe. In *ASAE Annual International Meeting*, No. 032344, 2003.

30. Allred, B. J., J. J. Daniels, N. R. Fausey, C. Chen, L. Peters Jr., and H. Youn. Important Considerations for Locating Buried Agricultural Drainage Pipe Using Ground Penetrating Radar. *Applied Engineering in Agriculture*, Vol. 21, No. 1, 2005, pp. 71–87.

31. Pipan, M., L. Baradello, E. Forte, A. Prizzon, and I. Finetti. 2-D and 3-D Processing and Interpretation of Multi-Fold Ground Penetrating Radar Data: A Case History from an Archaeological Site. *Journal of Applied Geophysics*, Vol. 41, No. 2, 1999, pp. 271–292. doi: 10.1016/S0926-9851(98)00047-0.

32. Leckebusch, J. Two- and Three-Dimensional Ground-Penetrating Radar Surveys Across a Medieval Choir: A Case Study in Archaeology. *Archaeological Prospection*, Vol. 7, No. 3, 2000, pp. 189–200. doi: 10.1002/1099-0763(200009)7:3<189::AID-ARP134>3.0.CO;2-N.

33. Basile, V., M. T. Carrozzo, S. Negri, L. Nuzzo, T. Quarta, and A. V. Villani. A Ground-Penetrating Radar Survey for Archaeological Investigations in an Urban Area (Lecce, Italy). *Journal of Applied Geophysics*, Vol. 44, No. 1, 2000, pp. 15–32. doi: 10.1016/S0926-9851(99)00070-1.

34. Sternberg, B. K., and J. W. McGill. Archaeology Studies in Southern Arizona Using Ground Penetrating Radar. *Journal of Applied Geophysics*, Vol. 33, No. 1, 1995, pp. 209–225. doi: 10.1016/0926-9851(95)90042-X.

35. da Silva Cezar, G., P. L. Ferrucio da Rocha, A. Buarque, and A. da Costa. Two Brazilian Archaeological Sites Investigated by GPR: Serrano and Morro Grande. *Journal of Applied Geophysics*, Vol. 47, No. 3, 2001, pp. 227–240. doi: 10.1016/S0926-9851(01)00067-2.

36. Goodman, D. Ground-Penetrating Radar Simulation in Engineering and Archaeology. *Geophysics*, Vol. 59, No. 2, 1994, pp. 224–232. doi: 10.1190/1.1443584.

37. Gader, P. D., B. N. Nelson, H. Frigui, G. Vaillette, and J. M. Keller. Fuzzy Logic Detection of Landmines with Ground Penetrating Radar. *Signal Processing*, Vol. 80, No. 6, 2000, pp. 1069–1084. doi: 10.1016/S0165-1684(00)00020-7.

38. Yu, S. H., R. K. Mehra, and T. R. Witten. Automatic Mine Detection Based on Ground-Penetrating Radar. In *Proceedings of SPIE*, Vol. 3710, 1999, p. 961. doi: 10.1117/12.357116.

39. Bruschini, C., B. Gros, F. Guerne, P. Y. Pièce, and O. Carmona. Ground Penetrating Radar and Imaging Metal Detector for Antipersonnel Mine Detection. *Journal of Applied Geophysics*, Vol. 40, No. 1, 1998, pp. 59–71. doi: 10.1016/S0926-9851(97)00038-4.

40. Montoya, T. P., and G. S. Smith. Land Mine Detection Using a Ground-Penetrating Radar Based on Resistively

Loaded Vee Dipoles. *IEEE Transactions on Antennae and Propagation*, Vol. 47, No. 12, 1999, pp. 1795–1806.

41. Earp, S. L., E. S. Hughes, T. J. Elkins, and R. Vickers. Ultra-Wideband Ground Penetrating Radar for the Detection of Buried Metallic Mines. *Aerospace and Electronic Systems Magazine, IEEE*, Vol. 11, No. 9, 1996, pp. 30–39.

42. Sun, Y., and J. Li. Time-Frequency Analysis for Plastic Landmine Detection via Forward-Looking Ground Penetrating Radar. In *Radar, Sonar and Navigation, IEEE Proceedings*, Vol. 150, 2003, pp. 253–261. IET.

43. Song, J., Q. H. Liu, P. Torrione, and L. Collins. Two-Dimensional and Three Dimensional Nufft Migration Method for Landmine Detection Using Ground Penetrating Radar. *IEEE Transactions on Geoscience and Remote Sensing*, Vol. 44, No. 6, 2006, pp. 1462–1469.

44. Zoubir, A. M., I. J. Chant, C. L. Brown, B. Barkat, and C. Abeynayake. Signal Processing Techniques for Landmine Detection Using Impulse Ground Penetrating Radar. *Sensors Journal, IEEE*, Vol. 2, No. 1, 2002, pp. 41–51.

45. Gader, P. D., M. Mystkowski, and Y. Zhao. Landmine Detection with Ground Penetrating Radar Using Hidden Markov Models. *IEEE Transactions on Geoscience and Remote Sensing*, Vol. 39, No. 6, 2001, pp. 1231–1244.

46. Lee, J. S., C. Nguyen, and T. Scullion. A Novel, Compact, Low-Cost, Impulse Ground-Penetrating Radar for Non-destructive Evaluation of Pavements. *IEEE Transactions on Instrumentation and Measurement*, Vol. 53, No. 6, 2004, pp. 1502–1509.

47. Olhoeft, G. R., and S. S. Smith III. Automatic Processing and Modeling of GPR Data for Pavement Thickness and Properties. *Proceedings of SPIE*, Vol. 4084, 2000, p. 188.

48. Saarenketo, T., and T. Scullion. Road Evaluation with Ground Penetrating Radar. *Journal of Applied Geophysics*, Vol. 43, No. 2, 2000, pp. 119–138. doi: 10.1016/S0926-9851(99)00052-X.

49. Saarenketo, T. *Measuring Electromagnetic Properties of Asphalt for Pavement Quality Control and Defect Mapping*. Roadscanners, Ravaniemi, Finland, 2009.

50. Spagnolini, U., and V. Rampa. Multitarget Detection/Tracking for Monostatic Ground Penetrating Radar: Application to Pavement Profiling. *IEEE Transactions on Geoscience and Remote Sensing*, Vol. 37, No. 1, 1999, pp. 383–394.

51. Johnson, R. H., and E. P. Poeter. Interpreting DNAPL Saturations in a Laboratory-Scale Injection Using One- and Two-Dimensional Modeling of GPR Data. *Ground Water Monitoring & Remediation*, Vol. 25, No. 1, 2005, pp. 159–169.

52. Siriwardane, H. J., S. Pyakurel, R. Kiriakidis, U. B. Halabe, and R. Ingram. Laboratory Determination of Phreatic Surface During Seepage Through Soils Using Ground Penetrating Radar. *Review of Quantitative Nondestructive Evaluation* (D. O. Thompson and D. E. Chimenti, eds.) Vol. 26, 2007, pp. 1389–1394. doi: 10.1063/1.2718128.

53. Yigit, E., S. Demirci, C. Ozdemir, and A. Kavak. A Synthetic Aperture Radar-Based Focusing Algorithm for B-Scan Ground Penetrating Radar Imagery. *Microwave and Optical Technology Letters*, Vol. 49, No. 10, 2007, pp. 2534–2540. doi: 10.1002/mop.22724.

54. Abujarad, F., G. Nadim, and A. Omar. Clutter Reduction and Detection of Landmine Objects in Ground Penetration Radar Data Using Singular Value Decomposition (SVD). *Proceedings of the 3rd International Workshop on Advanced Ground Penetrating Radar, IWAGPR*, IEEE, 2005, pp. 37–42. doi: 10.1109/AGPR.2005.1487840.

55. Abujarad, F., A. Jostingmeier, and A. Omar. Clutter Removal for Landmine using Different Signal Processing Techniques. *Tenth International Conference on Ground Penetrating Radar*, 2004, pp. 697–700.

56. Caldecott, R., J. D. Young, J. P. Hall, and A. J. Terzuoli. *An Underground Obstacle Detection and Mapping System*. Electric Power Research Institute (Report EPPRI EL), 1985.

57. Brunzell, H. *Detection of Shallowly Buried Objects Using Impulse Radar. IEEE Transactions on Geoscience and Remote Sensing*, Vol. 37. No. 2, pp. 875–886, March 1999.

58. Carevic, D. A Kalman *Filter-Based Approach to Target Detection and Target-Background Separation in Ground Penetrating Radar Data*. Report DSTO-TR-0853. DSTO Electronics and Surveillance Research Laboratory. Salisbury, South Australia, Australia, 1999.

59. Khan, U. S., and W. Al-Nuaimy. Background Removal from GPR Data Using Eigenvalues. *13th International Conference on Ground Penetrating Radar (GPR)*. IEEE, 2010, pp. 1–5. doi: 10.1109/ICGPR.2010.5550079.

60. Hakan, B. Clutter Reduction and Object Detection in Surface Penetrating Radar. *Radar 97 (Conf. Publ. No. 449)*, 1997, pp. 688–691. doi: 10.1049/cp:19971763.

61. Dogaru, T., and L. Carin. Time-Domain Sensing of Targets Buried Under a Rough Air-Ground Interface. *IEEE Transactions on Antennae and Propagation*, Vol. 46, No. 3, 1998, pp. 360–372.

62. Hakan, B. Detection of Shallowly Buried Objects Using Impulse Radar *IEEE Transactions on Geoscience and Remote Sensing*, Vol. 37, No. 2, 1999, pp. 875–886.

63. Sezgin, M. Simultaneous Buried Object Detection and Imaging Technique Utilizing Fuzzy Weighted Background Calculation and Target Energy Moments on Ground Penetrating Radar Data. *Journal on Advances in Signal Processing*, Vol. 2011, No. 55, 2011. doi: 10.1186/1687-6180-2011-55.

64. Sezgin, M. A Novel Detection Warning Signal Creation Method for Hand-Held GPR Applications. *13th International Conference on Ground Penetrating Radar (GPR)*, IEEE, 2010, pp. 1–6. doi: 10.1109/ICGPR.2010.5550163.

65. Nuzzo, L., and T. Quarta. Improvement in GPR Coherent Noise Attenuation Using τ-p and Wavelet Transforms. *Geophysics*, Vol. 69, No. 3, 2004, pp. 789–802.

66. Carevic, D. Clutter Reduction and Detection of Minelike Objects in Ground Penetrating Radar Data Using Wavelets. *Subsurface Sensing Technologies and Applications*, Vol. 1, No. 1, 2000, pp. 101–118.

67. Al-Nuaimy, W., Y. Huang, M. Nakhkash, M. T. C. Fang, V. T. Nguyen, and A. Eriksen. Automatic Detection of Buried Utilities and Solid Objects with GPR Using Neural Networks and Pattern Recognition. *Journal of Applied Geophysics*, Vol. 43, 2000, pp. 157–165.

68. Delbo, S., P. Gamba, and D. Roccato. A Fuzzy Shell Clustering Approach to Recognize Hyperbolic Signatures in Subsurface Radar Images. *IEEE Transactions on Geoscience and Remote Sensing*, Vol. 38, No. 3, 2000, pp. 1447–1451.

69. Pasolli, E., F. Melgani, and M. Donelli. Automatic Analysis of GPR Images: A Pattern-Recognition Approach. *IEEE Transactions on Geoscience and Remote Sensing*, Vol. 47, No. 7, 2009, pp. 2206–2217.

70. Milisavljevi, N., I. Bloch, S. van den Broek, and M. Acheroy. Improving Mine Recognition Through Processing

and Dempster–Shafer Fusion of Ground-Penetrating Radar Data. *Pattern Recognition*, Vol. 36, 2003, pp. 1233–1250. doi: 10.1016/S0031-3203(02)00251-0.

71. Ehret, B. Pattern Recognition of Geophysical Data. *Geoderma*, Vol. 160, No. 1, 2010, pp. 111–125. doi: 10.1016/j.geoderma.2009.09.008.

About the Joint Transportation Research Program (JTRP)

On March 11, 1937, the Indiana Legislature passed an act which authorized the Indiana State Highway Commission to cooperate with and assist Purdue University in developing the best methods of improving and maintaining the highways of the state and the respective counties thereof. That collaborative effort was called the Joint Highway Research Project (JHRP). In 1997 the collaborative venture was renamed as the Joint Transportation Research Program (JTRP) to reflect the state and national efforts to integrate the management and operation of various transportation modes.

The first studies of JHRP were concerned with Test Road No. 1—evaluation of the weathering characteristics of stabilized materials. After World War II, the JHRP program grew substantially and was regularly producing technical reports. Over 1,500 technical reports are now available, published as part of the JHRP and subsequently JTRP collaborative venture between Purdue University and what is now the Indiana Department of Transportation.

Free online access to all reports is provided through a unique collaboration between JTRP and Purdue Libraries. These are available at: http://docs.lib.purdue.edu/jtrp

Further information about JTRP and its current research program is available at: http://www.purdue.edu/jtrp

About This Report

An open access version of this publication is available online. This can be most easily located using the Digital Object Identifier (doi) listed below. Pre-2011 publications that include color illustrations are available online in color but are printed only in grayscale.

The recommended citation for this publication is: